⑫

AD-A256 618

‖‖‖‖‖‖‖‖‖‖‖‖‖‖‖‖

The Pennsylvania State University
APPLIED RESEARCH LABORATORY
P.O. Box 30
State College, PA 16804

MODEL FOR THE FORMATION AND EVOLUTION
OF SAND RIDGES ON THE CONTINENTAL SHELF

by

J. M. Restrepo
J. L. Bona

Technical Report No. TR 92-06
October 1992

DTIC
OCT 23 1992
D

Approved for public release; distribution unlimited

92-28204

‖‖‖‖‖‖‖‖‖‖‖‖‖‖‖‖

REPORT DOCUMENTATION PAGE

1. AGENCY USE ONLY (Leave blank)	2. REPORT DATE October 1992	3. REPORT TYPE AND DATES COVERED

4. TITLE AND SUBTITLE

Model for the Formation and Evolution of Sand Ridges on the Continental Shelf

5. FUNDING NUMBERS

6. AUTHOR(S)

J. M. Restrepo, J. L. Bona

7. PERFORMING ORGANIZATION NAME(S) AND ADDRESS(ES)

The Applied Research Laboratory
P.O. Box 30
State College, PA 16804

8. PERFORMING ORGANIZATION REPORT NUMBER

TR-92-06

9. SPONSORING / MONITORING AGENCY NAME(S) AND ADDRESS(ES)

Space and Naval Warfare Systems Command
Department of the Navy
Washington, DC 20363-5000

10. SPONSORING / MONITORING AGENCY REPORT NUMBER

N00039-88-C-0051

11. SUPPLEMENTARY NOTES

12a. DISTRIBUTION / AVAILABILITY STATEMENT

Approved for Public Release. Distribution Unlimited.

12b. DISTRIBUTION CODE

13. ABSTRACT (Maximum 200 words)

A model for the formation and evolution of three-dimensional sedimentary structures such as longshore sand ridges, on the continental shelf in water deeper than that of the shoaling region, is proposed. The model is based on the interaction between surficial or internal weakly nonlinear shallow water waves having weak span-wise spatial dependence and the bottom topography.

While these ridges are not the results of a single formative agent, it is argued that the mechanism proposed in this study does contribute significantly to their generation and evolution. Testing the hypothesis, however, is as difficult as formulating it. Comparisons of this model with oceanographic data must wait for sufficient data to become available. In conjunction with developing the sand ridge model, this study proposes a new mathematical equation, properties of which are explored here in some detail. This equation potentially applies to other physical processes and raises questions which are themselves good avenues for further research.

The numerical implementation of the model combines fixed point methods with finite difference techniques, resulting in a scheme which is found to be superior to conventional finite difference technique in economy of computational resources and speed. Details of the scheme's inner workings and performance are included.

14. SUBJECT TERMS	15. NUMBER OF PAGES
Sand ridges, continental shelf, sedimentary structure, model, non-linear, shallow water waves, finite difference	169
	16. PRICE CODE

17. SECURITY CLASSIFICATION OF REPORT	18. SECURITY CLASSIFICATION OF THIS PAGE	19. SECURITY CLASSIFICATION OF ABSTRACT	20. LIMITATION OF ABSTRACT
UNCLASSIFIED	UNCLASSIFIED	UNCLASSIFIED	

DTIC QUALITY INSPECTED 1

Abstract

A model for the formation and evolution of three-dimensional sedimentary structures such as longshore sand ridges, on the continental shelf in water deeper than that of the shoaling region, is proposed. The model is based on the interaction between surficial or internal weakly nonlinear shallow water waves having weak span-wise spatial dependence and the bottom topography.

While these ridges are not the result of a single formative agent, it is argued that the mechanism proposed in this study does contribute significantly to their generation and evolution. Testing the hypothesis, however, is as difficult as formulating it. Comparisons of this model with oceanographic data must wait for sufficient data to become available. In conjunction with developing the sand ridge model, this study proposes a new mathematical equation, properties of which are explored here in some detail. This equation potentially applies to other physical processes and raises questions which are themselves good avenues for further research.

The numerical implementation of the model combines fixed point methods with finite difference techniques, resulting in a scheme which is found to be superior to conventional finite difference techniques in economy of computational resources and speed. Details of the scheme's inner workings and its performance are included.

Contents

List of Figures

List of Tables

Chapter 1

Introduction

1.1 Statement of the Problem

The dynamics of sand ridges, which are a common feature of the Continental Shelf, are poorly understood. Sand ridges are underwater bar-like features composed of loose granular sediment. Hundreds of meters long and up to a few meters high sand ridges are usually found in groups, arranged in more or less parallel rows separated from each other by hundreds of meters. They may be loosely classified as either tidal ridges or longshore sand ridges. Tidal ridges are oriented parallel to the prevailing direction of the local ocean currents, whereas longshore sand ridges are oriented normal to the direction in which the overlying water waves propagate. In this study I propose a possible mechanism for the formation and evolution of longshore sand ridges.

The model presented here follows from work initiated by Boczar-Karakiewicz and Bona, which dates to 1986. In [1] they conjecture that longshore sand ridges are the result of energetic interactions between shallow water waves and the underlying bottom topography, and propose a simple model, which in [2] was shown to be in qualitative agreement with oceanic data. While the present study owes much to the previous work, it improves upon it considerably and in several ways. In addition to extending the two-dimensional model to three dimensions, this work contributes to an understanding of

the general behavior and mathematical structure of both the two- and three-dimensional model. The model is free of adjustable parameters and, at this stage, intentionally crude. Our motivation was to present the simplest possible formulation in order to effectively study and test the hypothesis unhindered by physically negligible effects. We do not claim that sand ridge formation is the result of a single event or agent, nor do we claim that this model rules out all other explanations for the phenomenon. Rather, we describe a likely mechanism for the formation and evolution of these structures, a mechanism we believe must play a significant role.

A great deal of work on the problems of sedimentation has been done; however, particularly since the middle of this century, most of the work has been directed towards understanding smaller-scale aspects of sediment motion, rather than the formation and evolution of sedimentary structures. For a comprehensive review of the present level of our understanding of sedimentation, the reader is referred to Sleath [3]. While considerable progress has been made, our current understanding of sediment dynamics and, especially, of sedimentary structure formation is far from complete. The emphasis in this dissertation will be on the fluid mechanical aspects of sedimentation. We believe that a great deal of progress in understanding sediment movement in a fluid environment can be achieved by determining first what sort of patterns the fluid is able to generate.

The plan of the dissertation is as follows. In this introduction, we discuss the relevance of the study, describe the morphology of oceanic sedimentary structures, comment on observational and laboratory work, and review the various sedimentation and sand-bar models. In Chapter 2, we consider the main hydrodynamical issues for the cases of both surface and internal waves. Chapter 3 deals with the boundary-layer problem and with the development of a mass transport equation driven by the nonlinear wave motion.

Chapter 4 presents analytical results pertinent to the new equations resulting from the hydrodynamic problem discussed in Chapter 2. Chapter 5 presents the numerical solution of the full system, along with an analysis and evaluation of the numerical scheme. Numerical examples are presented and qualitatively discussed in Chapter 6 Chapter 7 lists conclusions and open questions worthy of future pursuit. Two appendices provide details on the higher order theory.

1.2 Relevance of This Study

For many, celebrating the beauty and mystery of nature is sufficient reason for studying the patterns and structures by which nature organizes and evolves. Nevertheless, there are also very practical reasons for research into sedimentary structures, some of which are listed below:

- The study and control of coastal erosion is of major economic, political, and ecological importance to communities that neighbor oceans and major lakes.

- Most features of the ocean bottom evolve in geological time scales; sedimentary structures, however, change comparatively quickly. A model of sedimentary structure evolution and movement will help us understand how these quickly evolving features will modify the bottom topography over time scales relevant for such things as navigation.

- Understanding the movement of these structures may help biologists discern how nutrients and organic materials migrate along the ocean bottom, information essential to understanding the dynamics of the marine habitat.

- Similarly, such knowledge may shed light on the movement and eventual fate of man-made pollutants and debris.

- Alternatively, the sedimentary structures themselves may have economic and social importance. The best surfing beaches have naturally occurring sandbars strategically located to concentrate the action of water waves in some areas and destroy it in others. Predictability of these so-called "hot spots" is essential to the welfare of the surfing community.

- Sand ridges are part of hydrocarbon reservoirs in ancient strata. Predicting their properties and evolution would be useful in petroleum exploration.

- The storm-wave devastation of coastal communities and offshore structures could, in principle, be significantly ameliorated by the construction of lightweight sandbar-like structures, which could be "tuned" to the most damaging waves, thus damping them considerably. This technique would replace the present heavy and very expensive barrier walls, which may impinge harmfully on the natural balance in the environment.

- The above-mentioned resonant effect may also be used to produce the opposite effect: the bar-like structures could act as a lens, concentrating the power of the most energetic waves into a small region and thus increasing the efficiency of water-wave driven electric generators.

- The approach taken to understand the formation and evolution of sand ridges may be applicable in some degree to other structures in nature that are the result of fundamentally nonlinear interactions, such as cloud patterns and sand dunes.

1.3 Morphology of Oceanic Sedimentary Structures

Not that long ago it was thought that sand ripples, like those found in the beach zone, and their larger cousins the sand ridges. were morphologically similar. We now recognize a

variety of different sedimentary structures, defining the categories by shape or generating mechanism. Examples are sand ripples, ridge-runnel systems, tidal ridges, longshore sand ridges. The formation and maintenance of these sedimentary structures is not well understood.

In the near-beach zone, including the breaker zone, occur small sand ripples, on the order of a few centimeters high, which come in a multitude of shapes and forms. Larger structures, such as crescentic bars, occur as well. In this region the fluid flow is quite complex, since there are both incident and reflected waves, tidal flow effects, and turbulence from wave breaking.

The ridge-runnel system, so common in the near-beach zones in the American Northeast and in the Great Lakes [4], is comprised of a large bump 3 to 15 meters away from the beach, about 0.3 meters high and up to perhaps 7 to 10 meters in length, which is preceeded by a runnel. The runnel may or may not be scoured with small ripples. The system is thought to be formed by storms eroding the beach and the dune fields and/or by tidal currents [4]. Davis et al. [4] provide observational evidence for their claim that storms seem to play a minor role in the evolution of these structures once they have formed.

Tidal ridges, which were noticed by Off [5], are rhythmic features oriented parallel to the direction of tidal currents. They are 8 to 30 meters high, 7 to 60 kilometers long, and separated by 1 to 10 kilometers. Allen [6] found that their height is roughly proportional to the square root of their spacing, and that they are composed of sand, silt, and mud. He reported that they occur where tidal currents reach at least 1 to 5 knots and where there is an ample supply of sediment. Tidal ridges are also very prominent in the neighborhood of river deltas. Tidal ridges may have a fairly flat dome, suggesting to some researchers that erosion effects play a very minor role.

Sandbars are distributed in complicated patterns on the continental shelf, and it is sometimes difficult to discern which is a tidal ridge and which is a longshore sand ridge. the object of attention in this study. For example, Figure 1.1, taken from a paper by Swift [7], shows the relative orientation of different types of ridges. Note that some bars fan out around river deltas, while some are oriented parallel or almost normal to the coast.
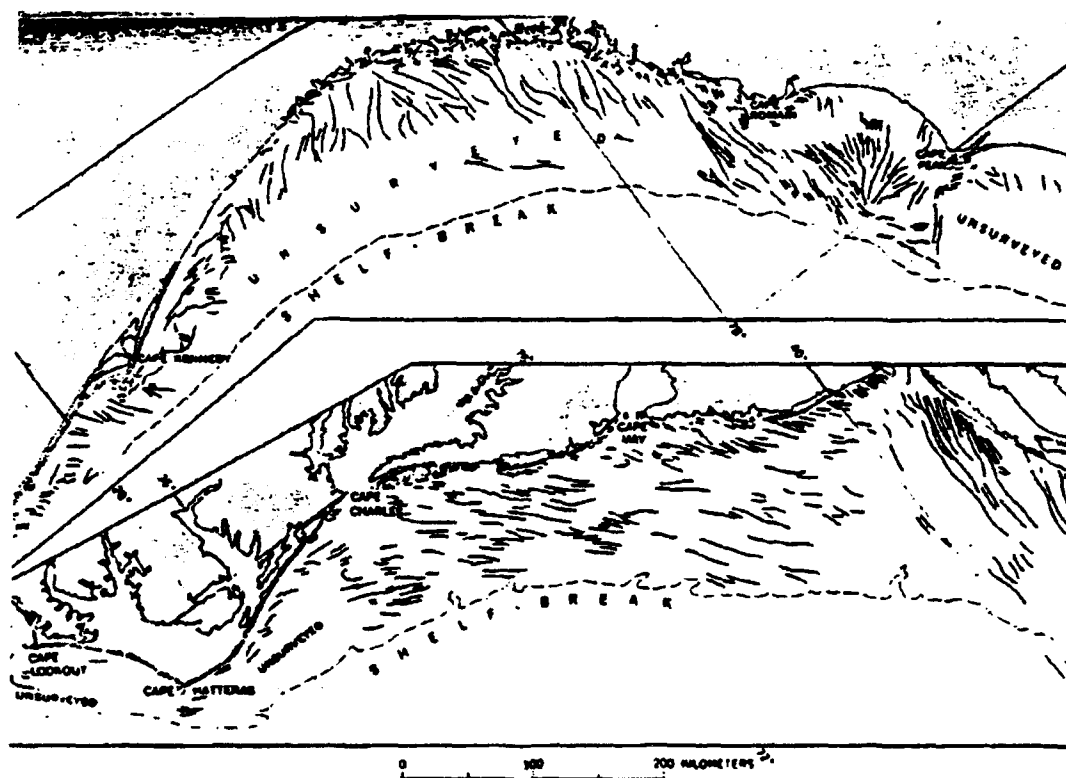
Figure 1.1: Submerged ridge field from Long Island to Florida, from Swift [7].

Longshore sand ridges are common features of the continental shelf in water deeper than the surf zone, from the near-shore region to the farthest reaches of the shelf. The better-known ridge fields are those found in the shallowest end of this range, primarily because they are readily seen, as is illustrated in Figure 1.2, which shows the bar system off central Harrison County, Mississippi. Other near-shore systems are found along the

coasts of the Carolinas, Florida, the northern coast of Alaska, in the Black Sea, the Baltic Sea, and even in large lakes such as Lake Michigan. Longshore sand ridges can be found in the farthest reaches of the shelf hugging every continent around the world as well.

From observations there seems to be a mean gradient, in the neighborhood of 0.02 to 0.05, which favors the formation of longshore sand ridges [8]. The ridges are composed mostly of fine sand and silt, sometimes of mud. The mean sediment particle size ranges between 0.1 and 0.5 millimeters. As shown in Figure 1.3, the ridges are typically a few
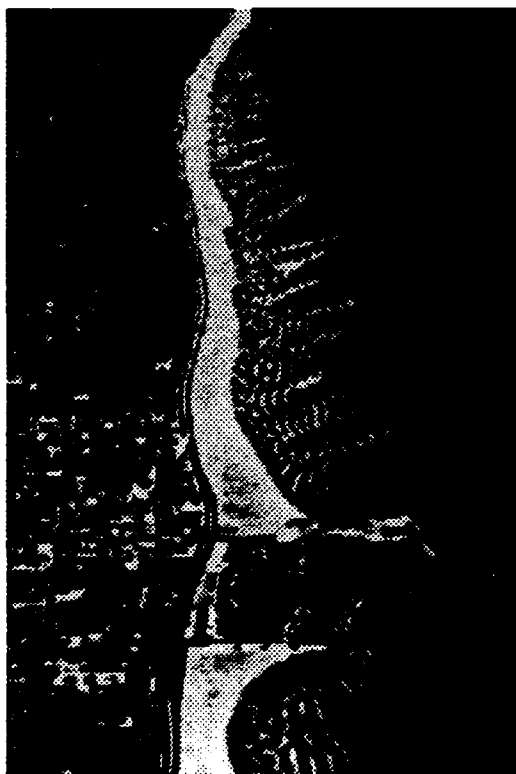
Figure 1.2: Sand ridges in shallow water, Harrison County, Mississippi.

meters high and are spaced hundreds of meters from each other. Groups of up to 12 ridges have been seen, mostly parallel to each other. Their migration rates vary from place to place; for instance, the ridges on Sable Island Bank have been estimated to move at rates ranging from 0.5 meters per year, in water 60 meters deep, to 5 meters

per year, in 30-meter depths [9]. The ridge fields are routinely found in regions where the water depth is small compared to the wavelength of surface waves with frequencies in the infra-gravity range [10].
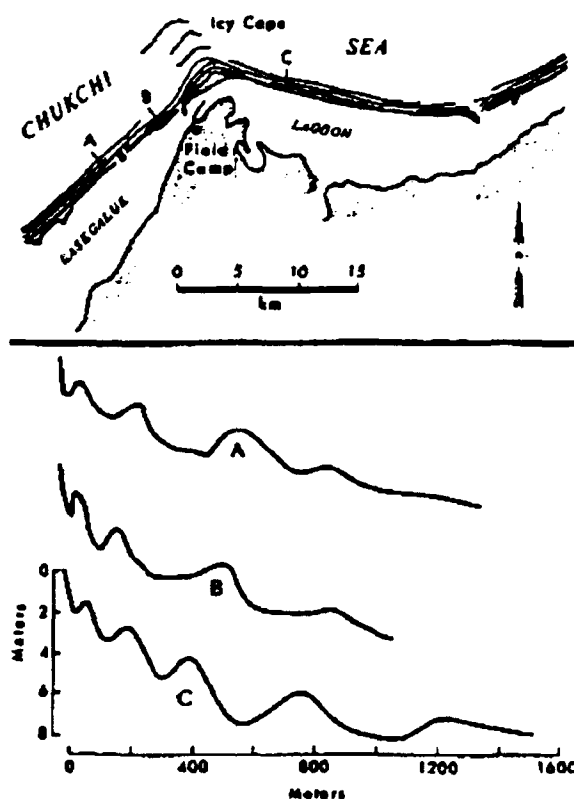
Figure 1.3: Cross Section. Sand ridges off the coast of Northern Alaska. Almost half of the 1350 Km. long coast share such morphology. From Short [10].

1.4 Comments on Field and Laboratory Observations

In addition to the inherent difficulties of conducting laboratory experiments involving liquid/sediment media (such as leveling the sediment bed after each trial, extracting gas bubbles and contaminants, etc.), laboratory experiments that purport to model oceanic phenomena are difficult to interpret since, in most cases, oceanic phenomena do not

scale well to laboratory conditions. Field observations are also quite challenging. The environment can be quite hostile, time scales are long, and spatial scales are large.

It was not until the mid-1940s that exploration into the deeper parts of the continental shelf was even considered. In the '60s and '70s a great deal of field observations were made on sand structures of all sorts. Nevertheless, ridge fields have just begun to be investigated in a systematic way. Our expertise with signal processing, telemetry, and acoustical and radio wave remote sensing have only recently been upgraded to the point where large scale or long term experiments are now possible [11]. Although acoustical wave remote sensing has been shown to be the best way to probe the ocean environment, we lack the concerted effort that would be required to produce large-scale acoustic array measurements that would enable time-dependent data gathering of the bottom topography and fluid motion. It is no surprise, then, that very few complete data sets of ridge fields exist in the open literature at present. In addition, what is meant by a "complete" data set has been changing over the years. In our study, a complete data set would include bathimetric records, as well as surface or internal wave directional spectra taken over the course of years.

What do experiments suggest about sedimentary transport in an oceanic environment? In the case of laboratory experiments with sand ripples, theory seems to qualitatively agree with experiments for a rather limited regime of flow and time spans. Some of the most carefully conducted sand-ripple experiments are those of Boczar-Karakiewicz, Benjamin, and Pritchard [12]. However, Pritchard [13] has stated that, based on his as-yet unpublished results, with an erodible bed in a standing wave tank, a wave field can show very long periods of homogeneous activity with little discernible movement of the bottom. Then, at an unpredictable moment, if all is right, the waves can grow to the point of breaking. A great deal of turbulence is seen in the boundary layer, the bed

suffers a very quick rearrangement, and the wave field returns to little activity. Pritchard did not measure all of the fluid parameters in the water column or in the suspended sediment. In his opinion, insofar as sand ripples in the near-shore zone are concerned, wave breaking is an extremely important source of sediment structure formation.

Is wave breaking essential to the generation of sand ridges? Ripples can be formed in a laboratory tank by a non-breaking wave field. Sand ridges, as was mentioned earlier, appear in regions where no breaking waves occur. Most models for the near- or far-shore zones, like the one which will be presented here, do not apply to the breaker zone. While breaking is an excellent source of turbulence, we do not know how it controls the dynamics of sediment and of the underlying sand structures. Nevertheless, wave breaking away from the breaker region has been seen to have the following effects: Lau and Travis [8] found that sandbars beyond the breaker zone do not disappear, but simply change location after a severe storm. Short, in his field observations in Northern Alaska [10], found that severe storms seem to rework the bars, but that some sandbars photographed in 1949 and 1955 were still identifiable after approximately 30 years. Preliminary data from the so-called "Super Duck" [11] experiments (purported to be the most conclusive measurement enterprise) show this bar "reworking"; we are waiting for the release of these data.

There are two main differences in the near and far ends of the continental shelf insofar as the fluid environment is concerned. First, in the near-shore we can identify strong incident and reflected components to the wave field. Second, as the (nonlinear) waves shoal some of the energy in the lower frequencies will shift to higher frequencies. Not only is there significant asymmetry in the velocity field, there can be quite pronounced asymmetry in the acceleration field. Bijker et al. [14] made laboratory measurements of acceleration and velocity fields for water waves with fairly high Stokes numbers, in the

order of 12-57. They found the net transport to be in the direction of the wave, particularly if the wave was very nonlinear. Smaller particles seemed to be transported mostly by the Stokes flow, whereas larger particles responded mostly to the "acceleration" field. Hallermeier [15] analysed a large experimental data set and found an empirical rule for the prediction of ripple characteristics based on the acceleration field, which suggests that this field may be an important sand-transport mechanism in the near-beach zone. Elgar et al. [16] made measurements in the shoaling region, in water depths in the range of 1-6 meters, over a topography with mean slope of 5 %, which confirmed the existence of the velocity and acceleration field asymmetry. They found that the acceleration asymmetry becomes increasingly significant with decreasing water depth. The above investigations suggest that the acceleration field becomes ever more important as the distance to the beach decreases; our model would not apply in this area, since the transport equation we use does not include acceleration effects.

1.5   Sedimentation Transport Models

As mentioned previously, much of the work on sedimentation has been designed to understand how the sediment moves, rather than how it generates patterns. Most researchers working on sedimentation transport assume an outer fluid flow at the edge of a boundary layer, and attempt to model sediment motion on the bed and in the layer. Sleath presents a good review of the subject; we will summarize, therefore, only in a cursory manner the different sedimentation models.

A model developed by Bagnold [17,18] assumed that wave-induced oscillatory water motion causes sediment to move back and forth with a net expenditure of energy. Although no net transport results in such an oscillatory flow, the energy dissipation acts to

keep the sediment in suspension. Once in suspension, any steady current superimposed on this oscillatory flow will then cause a net transport of the suspended sediment in the direction of the instantaneous total bottom stress. Originally a bed load model, Bagnold's model is also applied to suspended load transport for low Froude number flows. A threshold of motion parameter, called the Shield's parameter, is incorporated into the model to reflect the fact that a critical amount of energy must be imparted on the bed before transport can occur. Smith [19] and Fredsœ [20] applied this model to the ocean environment. They assumed a constant eddy viscosity and obtained criteria for the onset of instability and ripple formation. Richards [21] used instead a turbulent scale that increases linearly in height from the bed, thus obtaining two modes of instability, which yield small- and large-scale ripples respectively. Bagnold's model has also been used with some success in the near-shore zone, in a version which includes the effect of wind on sediment transport rate [22]. However, Bailard and Inman [18] found that the model did not perform adequately when the waves are not normally incident to the beach.

Another sedimentation model by Raudkivi [23], and by Williams and Kemp [24], attributes the formation of ripples to a chance piling of sediment. This deformation then causes the flow to separate, with subsequent building up of the ripple downstream. They attribute the initial small deformation to the random action of highly turbulent velocities, or "bursts", close to the bed.

Lastly we mention the model in Longuett-Higgins' seminal paper [25]. He shows how a second order drift velocity, which was first noted by Stokes [26], develops in the boundary layer from an outer oscillatory flow or in the bulk of the fluid through the action of nonlinear waves. This drift velocity is capable of transporting sediment, particularly suspended sediment. A number of people have studied this mechanism; of note are Johns [27], who developed explicit expressions appropriate for the ocean environment

and studied the character of the drift velocity and its stability, and Blondeaux [28] and Vittori and Blondeaux [29], who looked at the stability and formation for Froude numbers at which flow separation does not occur. They determined adequate height, spacing, and onset thresholds, as compared to laboratory experiments. The second of these papers introduced more structure and made a case for the inclusion of nonlinear effects.

In our study we adopt this last model. The mean slopes in those regions of principal interest here are very low, hence down-slope gravitational transport, which is important in the coastal environment, plays a negligible role in this model. The ratio of bar height to separation is very much below the critical value of 0.1. As noted by Sleath [3], values above 0.1 usually lead to boundary layer separation behind the crests of the bars, and vortex formation takes place. When this occurs vortex ripples will spread over the entire bed.

1.6   Sedimentary Bar Models

Among the researchers who have coupled a sedimentation transport model to an oceanic wave field to look at the process of bar formation in the oceanic environment are Holman and Bowen [30]. They use the linear three-dimensional water wave equations to compute drift velocity, which in turn they substitute in Bagnold's transport model for suspended load. In particular, they examine the edge wave case in an effort to compute the formation of crescentic bars in the shoaling region. Bowen [31] has also examined the performance of his model in predicting the spacing of longshore ridges and reports good qualitative agreement with field observations.

As mentioned earlier in connection with Pritchard's work [12], laboratory and field observations indicate that standing wave patterns display a Bragg resonance process with an underlying wavy bottom. In the steady-state, the ripples develop a spacing

that is roughly half the local average length of the water waves. This theory [12,32-34] is applicable in the near-shore environment, since it relies on the scouring effect of a standing wave pattern. This first order theory is the one most widely studied, since it is most easily implemented in the laboratory: at one or another time, researchers implicated this mechanism in the generation of all sandbars.

The ridge and runnel system has been modeled using a variant of Bagnold's transport formula by Dean [22] and deVriend [35]. The extent of their success, however, is hard to discern from their publications. Since the undertow and the local bed slope are significant and since the effect of the wind in generating stresses on the surface of the ocean must be taken into account, modeling the formation of runnels is difficult. Russell and Osorio [36], Bijker et al. [37] found that on a sloping beach, the mass transport velocity near the bed was onshore before breaking and offshore after. This effect, independent of wave reflection from the beach, may explain why these bar systems are usually found close to the plunge line of breakers.

Huthnance [38] develops a theory for the formation of tidal ridges, based on an instability which is triggered by a small protuberance on the shelf. The ensuing boundary layer develops a bar that is fed by bedload. The resulting steady-state bar is finite in extent and parallel to the always present currents. Equilibrium is reached when the supply of sand is exhausted. Huthnance notes that the tops of these ridges are flat rather than rounded, which he claims dismisses erosion as being the source for the generation of these structures. Erosion should not be dismissed, however, since these bars appear close to river deltas and, possibly, as features of older beaches. Huthnance's study does not address the periodic nature of these bars and does not suggest a relation between their height and spacing.

Theories for the formation of the longshore sand ridges, which are the subject of this

study, will be briefly reviewed in the following section.

1.7 Proposed Model

1.7.1 Historical Development

Among the first to suggest that infragravity standing waves may be responsible for sand ridge formation was Suhaida [39]. He did so at a time when few people saw anything fundamentally different about near-shore sandbars, where a strong standing wave field is present, and bars or ridges far from the beach, where little or no standing wave pattern is to be found. Short [10] made field measurements of sand ridges in Alaska. He found a loose correlation between the ridge spacing and the average peak infragravity component wavelenth.

Lau and Travis [8] derived a drift velocity from a Stokes water wave field for a bed with constant slope. They were able to estimate the spacing and the number of ridges from the periodicity of the drift velocity. They made use of the SRIT (slightly resonant interacting triads) approximation developed by Lau and Barcilon [40] and Mei and Ünlüata [32] for weakly nonlinear shallow water waves to solve approximately for the wave motion. They made some comparisons with field data to examine the adequacy of their theory in predicting the observed bar separation distances.

Boczar-Karakiewicz brought this problem to the attention of Bona while the latter was visiting Poland in the early 1980s. Eventually, their collaboration resulted in the Boczar-Karakiewicz, Bona, Cohen paper [1], in which they use the ideas of Lau and Barcilon to obtain the resulting drift velocity in a boundary layer and use this drift velocity as a source of sediment motion in a transport equation. Exploiting the discrepancy of the time scales between fluid and sediment dynamics, they were able to formulate the first truly evolutionary sand ridge models. Their model is appropriate for the shallower

end of the continental shelf, since it was derived for an isotropic water environment. Later, the model was extended to the internal wave case and was tested against actual field data [2]. Encouraged by the results of the field data comparisons, it was thought that the natural extension of this ongoing research project should be to increase the model's applicability to three dimensions. The result is the present study. Bona and this author are currently pursuing some of the more theoretical issues in the project, while Boczar-Karakiewicz is testing the models against field data and is investigating possible practical improvements to the model, such as the use of more realistic transport equations and the addition of more phenomenology, so that the model might prove useful to the engineering community.

1.7.2 Brief Description of the Model

Referring to Figure 1.4, we envision infra-gravity waves coming into the purview of the model at the line $x = 0$, which is set, on the deep side, by the point at which the long waves "feel" the bottom topography. The shoreward direction, x, increases as the wave travels shoreward. The span-wise direction, given by y, is approximately parallel to the line of constant phase of the incoming waves. The waves propagate shoreward, possibly at an angle with respect to the prevailing direction of maximum gradient of the bottom topography. In the deeper reaches of the shelf, the waves would be supported by the picnocline, while in the isotropic water column, the waves would be on the ocean surface. The extent of the model is limited in the longshore direction by the disintegration of the interface supporting the internal waves, by the approach to the breaking zone, by any singularity in the depth, and by significant energy transfer from low to high frequencies. The span-wise direction is limited by the same sort of issues. Taking advantage of the disparate time scales for bottom and fluid evolution, the assumed gently sloping bottom will be considered to appear as a fixed but non-uniform surface to the waves

as they progress and eventually dissipate on the shore. This assumption enables us to decouple the problem: starting with some initial bottom configuration. we solve the hydrodynamics that evolve in time t and find the drift velocity in the boundary layer; the resultant drift velocity is then used in a transport equation to update the bottom topography, which is evolving in time scale T. which is considerably longer than t.
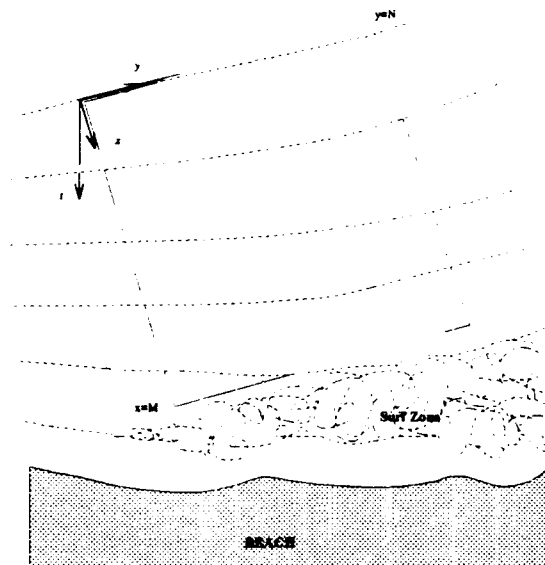
Figure 1.4: Aereal view of the problem.

1.7.3 General Comments

A few comments must be made as far as the general mechanism for longshore ripple and sand ridge formation is concerned. If a standing wave pattern exists in the surface waves, linear or nonlinear, the scouring effect of the waves generates ripples obeying a Bragg scattering mechanism. This is a first-order phenomenon. Its ability to influence the shape of the bottom topography relies on the existence of both a reflected and an incident wave. As we move further seaward. the reflected component may become weaker and weaker. Yet. we find large-scale bars. In this region it is suggested that the Bragg

mechanism gives way to the second-order, strictly nonlinear theory that we present in this study. Thus, we envision that both mechanisms operate along the continental shelf, but in the near-shore the first order theory is prevalent, while in the deeper reaches the second-order theory prevails.

The second order theory does not have to be strictly unidirectional. However, for very mild slopes and large distances from the shore, the reflected component is presumably very weak. Hence, if the bottom is not restricted in this way, as compared with spatial changes in the surface waves, the reflected component provides a great deal more structure. For the surface wave case the reflected component is still significant close to the shoaling region (which is the extreme end of the purview of this model); the waves are assumed, in the unidirectional case, to dissipate sufficiently so that the reflected component is negligible. For internal waves, the issue of dissipation is relatively more straightforward: As the density stratification collapses in the shallower reaches of the shelf, the water column is no longer able to support an internal wave. Incidentally, Boczar-Karakiewicz et al. [2] have found that the area in which stratification collapses agrees with the limit to which sand ridge fields appear.

The frequency range in this model is limited by assumptions of shallow water wave theory, i.e., long wavelengths compared to the local water column depth. For surface waves, the periods range from 0.5 minute to 0.5 hour, and energies in the order of $10^2 - 10^5 J/m^2$. For internal waves, the range is on the order of minutes to an hour in the period, and energies as high as $10^6 J/m^2$. The frequency range is infra-gravitational for both the surface and internal waves.

Internal waves in the above-mentioned frequency range are caused by such things as the action of tidal forces on the stratified fluid flow in places in which a sudden height change in the bottom topography occurs, such as that at the edge of the continental

shelf. For surface waves, on the other hand, the generating mechanism is less obvious: a distant storm, long-fetch wind effects, or tidal forces. No provision is made in the model for external forcing, such as by the wind. This restriction basically limits the frequency range of the surface case to very long waves. However, some of the longer waves are only observed in the farther reaches of the shelf, in areas where the assumptions of an isotropic water column are hardly realistic. In these areas, internal waves take over.

The equation which models the surface waves in this study is a highly truncated modal expansion of the Boussinesq system. In principle, however, there is no reason why the actual Boussinesq system itself could not be used. Elgar and his collaborators [41] have examined the issue of the recurrence of solutions to the modally truncated Boussinesq Equation numerically in the Stokes parameter regime of $O(1)$. They found that the two-mode case, which will be used in this study, displays recurrence-like solutions over a great many wavelengths of distance. As the number of modes is increased, they find that the recurrence is confined to fewer and fewer cycles the more modes are used. In addition they find that initially very narrow spectra undergo more recurrence-like cycles, before the spectra flatten, than do initially broad-banded spectra. Their conclusion is that recurrence-like solutions are an artifice of a severely truncated modal expansion of the Boussinesq Equation.

As is mentioned in their paper, other researchers have studied the issue of recurrence of solutions in such equations as the Nonlinear Schrödinger Equation (NLSE) and the Zakharov Equation (ZE), which share the common feature with the Boussinesq Equation that they all undergo $O(1)$ energetic transfers between their modes over large times/distances. Caponi and his collaborators [42] found numerically that in the ZE, depending on the initial conditions, the solutions were either "periodic, recurring, transitional, or chaotic." In connection with the NLSE, Weideman et al. [43] found that

solutions may be recurrent or chaotic, depending on the particular structure of the discretization used in its numerical solution and on the number of degrees of freedom. If the discretization preserves Hamiltonian structure, the orbits are homoclinic. Otherwise, if Hamiltonian structure is not preserved, for a few degrees of freedom the discrete NLSE behaves entirely differently than in the continuous case. As the number of degrees of freedom is increased, the solutions to the discrete and continuous NLSE converge, as does the Hamiltonian structure.

In conclusion, then, if Elgar and his co-workers' findings prove correct (we are presently addressing this issue in a separate study), we may be modeling the water waves in this study incorrectly. However, the observations of Elgar et al. do not weaken in any way our conjecture that weakly nonlinear shallow water waves are responsible for the formation and evolution of sand ridges. After all, there is more than ample observational evidence that these nonlinear waves travel over very vast spans of ocean. i.e.. that their spectra recurs a great many times before they lose their coherent shape, over regions where sar¹ ridges are a prominent feature of the ocean floor. Certainly, their findings do not square well with the recurrence-like solutions that internal waves are known to possess over very large spatial scales. Their research, if verifiable, leads us to conclude either that there is something inherently wrong with the modal expansions of the Boussinesq Equation as models for these types of waves or, more interestingly, that their findings, along with those of Caponi's and Weideman's groups, are pointing out that something as yet not understood but rather fundamental, is awaiting discovery in connection with discretizations of nonlinear evolution equations of the type discussed. There is still another possibility: It could be that the loss of coherence after a few recurrent cycles. in certain situations. is responsible for the interesting fine structure observed in actual sand ridge fields.

Chapter 2

The Hydrodynamics of the Water-Wave Problem

2.1 Preliminaries

Owing to the striking similarity of the typical bar spacing to the length scale at which energetic interactions among the most significant modes of shallow water waves takes place, we believe that longshore sand ridges are formed by flows in the boundary layer which are generated by these weakly-nonlinear long water waves. We refer to these waves as "shallow water waves" because their wavelength is considerably greater than the local depth of the water column on which they propagate. An appropriate description for these waves is given by the Boussinesq System [44].

In this section, starting from mass and momentum conservation, the equations for long weakly-nonlinear water waves are derived, detailing along the way the assumptions and approximations relevant to the oceanic environment.

2.1.1 Conservation of Mass and Momentum

Consider a function $\rho(r,t)$ defined in a time dependent set $\Omega_t \subset \mathcal{R}^3$, representing the density of the fluid in such a way that the total mass of the fluid body $m(\Omega_0)$ is equal to

$$\int_{\Omega_t} \rho(r,t)d^3r, \qquad (2.1)$$

and is constant. If this invariance holds it follows, presuming that both the density ρ and the velocity $\mathbf{u}$ are $\in C^1(\Omega_t)$, that

$$D_t \int_{\Omega_t} \rho(\mathbf{r},t)d^3r = \int_{\Omega_t} (D_t\rho + \rho\nabla \cdot \mathbf{u})d^3r, \qquad (2.2)$$

where the time derivative is the convective derivative, and we are making use of the divergence theorem and Leibniz' integration rule. If this invariance applies in every subdomain of the fluid body, then

$$D_t\rho + \rho\nabla \cdot \mathbf{u} = \partial_t\rho + \nabla \cdot (\rho\mathbf{u}). \qquad (2.3)$$

When it is assumed that the density of the fluid element does not change (although it may different for different fluid elements), the above simplifies to

$$\nabla \cdot \mathbf{u}, \qquad (2.4)$$

and we say that the fluid is "incompressible". Note that incompressibility is not a property of the fluid, but rather of the motion. It amounts to assuming that the volume is preserved, i.e. its flow is in conditions of constant volume. Equation (2.4) applies to the case considered in this study.

Momentum is conserved as well. Conservation of linear momentum asserts that

$$D_t \int_{\Omega_t} \rho\mathbf{u}d^3r = \int_{\Omega_t} \rho\mathbf{f}d^3r + \int_{\partial\Omega_t} \aleph \cdot \mathbf{n}d^2r, \qquad (2.5)$$

where $\mathbf{n}$ is the outward normal on $\partial\Omega_t$. $\mathbf{f}$ encompasses all bodily forces, such as gravity, coriolis, etc., and the contribution of contact forces enters the balance through the stress tensor $\aleph$. Expressed in another way, momentum conservation asserts that

$$D_t \int_{\Omega_t} \rho\mathbf{u}d^3r = \int_{\Omega_t} \rho\mathbf{f}d^3r + \int_{\Omega_t} \nabla\cdot\aleph d^3r. \qquad (2.6)$$

It is convenient to express $\aleph_{ij}$, with i and j running from 1 to 3 in this instance, as the sum of an isotropic part $-p\delta_{ij}$, having the same form as the stress tensor in a fluid at rest, and a remaining "deviatoric" part d_{ij} contributing to the tangential stresses. The tensor d_{ij} has the distinctive property of being due entirely to the existence of the motion of the fluid. Furthermore, the deviatoric tensor may be recast in terms of physically amenable terms. Assume that d_{ij} is linearly proportional to velocity gradients, so that the stress tensor is now $\aleph_{ij} = -p\delta_{ij} + 2\mu(\epsilon_{ij} - \epsilon_{ii}\delta_{ij}/3)$, p representing the pressure (which in a fluid in motion is not related to the variables of state in equilibrium thermodynamics), and the deviatoric stress tensor separated into pure straining motion and expansion, which are respectively the second and third terms of the above expression.

In almost all oceanic circumstances the fluid may be regarded as a constant density, Newtonian, and isotropic fluid. Thus, $\epsilon_{ij} = \epsilon_{ji}$, and momentum conservation leads to the Navier-Stokes equations

$$\rho\frac{Du_i}{Dt} = \rho f_i - \frac{\partial p}{\partial x_i} + \frac{\partial}{\partial x_j}\{2\mu(\epsilon_{ij} - \epsilon_{ii}\delta_{ij}/3)\} \qquad (2.7)$$

where

$$e_{ij} = \frac{1}{2}(\frac{\partial u_i}{\partial x_j} + \frac{\partial u_j}{\partial x_i}) \qquad (2.8)$$

is the rate-of-strain tensor, and μ is the viscosity of the fluid, which is a constant of proportionality between the rate of shear and the tangential force per unit area when plane layers of fluid slide over each other. The viscosity is a strictly positive quantity, reflecting the common observation that the force between layers of fluid in relative sliding motion is always a frictional force resisting the relative motion. The typical value of μ for water at 10^0C is roughly $1.3\cdot10^{-2}g/cm/sec$, and it decreases at about 3% per degree centigrade rise in temperature in the neighborhood of normal temperatures. When appreciable temperature differences exist in the flow field, μ must be considered spatially dependent.

However, in the oceanic setting under consideration, such temperature differences are not present and the viscosity is safely assumed constant. Adopting such a condition, and incorporating the incompressible condition, conservation of linear momentum in the bulk of the ocean is expressed as

$$\rho \frac{D\mathbf{u}}{Dt} = \rho \mathbf{f} - \nabla p + \mu \nabla^2 \mathbf{u}. \tag{2.9}$$

Viscous terms can be very important in narrow regions of flow, or in very small scale motions, where the significant velocity changes are confined to small distances, such as is the case in the so-called boundary layers at the air-water interface and in the fluid system immediately above the bottom topography. Consideration is first given, however, to the effect of viscosity away from both boundary layers in order to arrive at the appropriate equations of conservation in the bulk of the oceanic fluid.

Given that it is the fluid is isotropic and of constant density ρ, take λ, the wavelength of the water waves, to be typical of the length of appreciable spatial variation in the motion or magnitude of the velocity $\mathbf{u}$. Thus, the ratio $\mathcal{R} = \rho\lambda|\mathbf{u}|/\mu$, which is an appropriate Reynolds number for this situation, gives an estimate of the relative magnitudes of the inertial forces as a ratio to the viscous forces involved. For long wavelength waves, $|\mathbf{u}|$ may be replaced by the more accessible velocity measure $\omega\lambda$, where ω is the frequency of these waves. In this case the Reynolds number $\mathcal{R} \equiv \rho\omega\lambda^2/\mu$ emphasizes the fact that acceleration in the fluid is proportional to frequency. The size of $\mathcal{R}$ is quite large in the body of the oceanic fluid, reflecting the fact that the motion is almost entirely governed by inertial forces. Therefore, for fluid motion which is dominated by inertial forces, momentum conservation may be approximated by

$$\rho \frac{D\mathbf{u}}{Dt} = \rho \mathbf{f} - \nabla p \tag{2.10}$$

to reflect such balance in the bulk of the fluid. Boundary layers form on the air-water interface, and the water-bottom interface. The boundary layer at the water-bottom interface produces significant losses even in the ideal situation considered here. We shall reserve the discussion of the bottom boundary layer for a later chapter, however. The attenuation due to dissipative losses in the air-water interface can be estimated by the following argument: Since the tangential stresses at the surface are zero, and the normal stress proportional to the surface tension, the losses due to viscous effects, typified by the magnitude of $\nu \equiv \mu/\rho$, are small compared to the inertial forces, that is, the Reynolds number $\mathcal{R} = \omega \kappa^{-2}/\nu$ is large and hence, the vortical flow may be neglected. For typical long oceanic waves, $\mathcal{R} \sim 10^6 - 10^8$. Thus, the wave decay is found to be proportional to $exp(-2\nu\kappa^2 t)$ from the conditions imposed on the tangential and normal stresses at the surface, where κ is the wavenumber of the waves. For the typical case, the "e-folding" distance is in the order of years. This simple result is, of course, only true for a perfectly clean and wind-free interface, which generally is not the situation in the real ocean environment. When the surface is contaminated, the free surface boundary condition is more appropriately modelled by an elastic, or dynamic no-slip condition, and in that instance the dissipation is not trivial. Additionally, even if the surface was clean, the energetic interactions between strong wind and the waves usually overwhelm the internal frictional forces just discussed.

The contributions of coriolis, surface tension, wind, and gravitational forces are now briefly examined. With the exception of surface tension forces, the forces just mentioned enter the momentum balance as terms on the right-hand side of Equation (2.10). The role of surface tension is not borne out of conventional momentum balances in the bulk of the fluid, but rather, as an ad-hoc condition to be satisfied at the air-water interface.

The apparent body forces on a fluid element with coordinates at rest relative to a rotating earth with approximately constant angular velocity Ω are

$$- 2\Omega \times \mathbf{u} - \Omega \times (\Omega \times \mathbf{u}). \tag{2.11}$$

where the second term is known as the centripetal force and the first term as the coriolis force. A measure of the relative size of the inertial forces to the coriolis force for long water waves is given by $U/L\Omega$, which is known as the Rossby number. Here U is representative of the velocity, L is a characteristic length, and $\Omega \approx 7.3 \cdot 10^{-5} sec^{-1}$. When the Rossby number is greater than unity, the coriolis force is negligible as compared to inertial forces. For long waves the Rossby number may be estimated by the ratio ω/Ω, and this ratio is close to unity for planetary waves. Thus, coriolis forces would not play a significant role in this study, since the wave periods for the waves under consideration range between fractions of a minute and an hour -the infra-gravitational spectrum. The centripetal force may be absorbed into the pressure term in the Euler equation, i.e. Equation (2.10), or safely neglected since the magnitude of the inertial forces to it is $O(\omega/\Omega^2)$.

Continuity of stresses at the air-water interface dictate that the pressure on the two sides of the surface can differ only as a result of surface tension since ideally the surface has zero mass. The force's origin lies in the fact that for any sufficiently small reversible isothermal change in the system, the total work done is proportional to the gains in the total Helmholtz free energy [45]. The molecular origin of surface tension evidently lies in the intermolecular cohesive forces. The magnitude of this surface tension is proportional to the local interface curvature. Following Batchelor [45], for long waves the pressure at the interface is regarded as constant. The condition for equilibrium, with z the height above the zero level reference pressure is

$$\rho g z - \gamma \left(\frac{1}{R_1} + \frac{1}{R_2} \right) = \text{constant}, \tag{2.12}$$

where R_1 and R_2 are the radii of curvature on the air side. The constant γ is the surface tension constant, which for pure water at $15^\nu C$ is about $74dyn/cm$. The relevant parameter which reflects the relative size of this force is $\sqrt{\gamma/\rho g}$. For pure water, the value is about $0.27cm$, which is the length scale on which effects of surface tension are likely to be comparable to the effects of gravity. Since infra-gravitational waves have length scales many times larger than $0.27cm$, surface tension effects may be neglected.

The wind is a major source of energy in the surface-wave case. The water wave spectrum considered in this study spans waves with periods as long as tens of minutes and as short as fractions of a minute, depending on the water depth. The longest ones are generated by earth movements, distant storms and other powerful meteorological phenomena, but it is quite clear that the most important forcing source, for waves in the high end of the frequency range of the model, or equivalently, in the shallower end of the shelf, is the wind.

Modelling the interaction of the wind with the ocean surface is, at present, far from satisfactory. Nevertheless, two complementary mechanisms for the generation and main-tenance of waves by the wind have been proposed. Phillip's resonance model [46] pro-poses that if the pressure fluctuations of the wind are in phase with the surface waves, a resonant interaction is expected with ensuing wave growth. It is said to govern the initial stages of wave generation, and it ignores the interaction between the surface-wave and the actual air flow, i.e. it considers the direct action of turbulent fluctuations in aerodynamic pressure. A complementary theory is the shear-flow theory worked out by Miles [47], which governs the "instability" phase. In this theory there is a transfer of momentum from the wind to the water waves through Reynold stresses at the boundary layer with ensuing wave growth.

In this study it shall be assumed that the wave field was created outside of the

model's region of applicability. This is admittedly a gross simplification in the surface-wave version of the model, but again, at this exploratory stage of the model, consideration of the effect of the wind takes us far from more immediate issues.

2.2 Surface Wave Problem

By "hydrodynamic problem" we shall mean the problem in the domain that excludes the boundary layer that hugs the bottom. As we shall explain later, we shall exploit the tremendous discrepancy between the time scales of the fluid motion, represented by t, and the time scales of the bottom evolution given by T. The latter time scale is to be considered a parameter in what follows. As illustrated in Figure 2.1, one may define the domain for the hydrodynamic problem as $\Omega = \mathbf{R}^2 \times [-H(T) + \delta, \eta(t)] \approx \mathbf{R}^2 \times [-H(T), \eta(t)]$, since $\delta \ll |H|$. The fluid is subjected solely to gravitational forcing. The velocity field is given by $(\mathbf{u}, w)$, where the first entry is the transverse velocity and w is the vertical velocity. Position is represented by the vector $(\mathbf{r}, z)$. The free surface is given by $z = \eta(\mathbf{r}, t)$ and the bottom by $z = -H(\mathbf{r}, T)$. We adopt the convention throughout this study, that the operator $\nabla_3 \equiv \nabla + \hat{k}\partial_z$.

It is postulated that the fluid is initially irrotational. That is,

$$\nabla_3 \times (\mathbf{u}, w) = 0. \tag{2.13}$$

The curl of Equation (2.10) yields what is commonly referred to as the Helmholtz equation:

$$\frac{\partial}{\partial t}\nabla_3 \times (\mathbf{u}, w) + \nabla_3 \times (\nabla_3 \times (\mathbf{u}, w) \times (\mathbf{u}, w)) = 0, \tag{2.14}$$

making use of the fact that the force field is conservative. Appealing to Equation (2.13), and using the vector identity $\nabla_3 \times \nabla_3 \times (\mathbf{u}, w) = -(\mathbf{u}, w) \times \nabla_3 \times (\mathbf{u}, w)$, it is seen that

$$\frac{D}{Dt}(\nabla_3 \times (\mathbf{u}, w)) = \nabla_3 \times (\mathbf{u}, w)\cdot\nabla_3(\mathbf{u}, w). \tag{2.15}$$
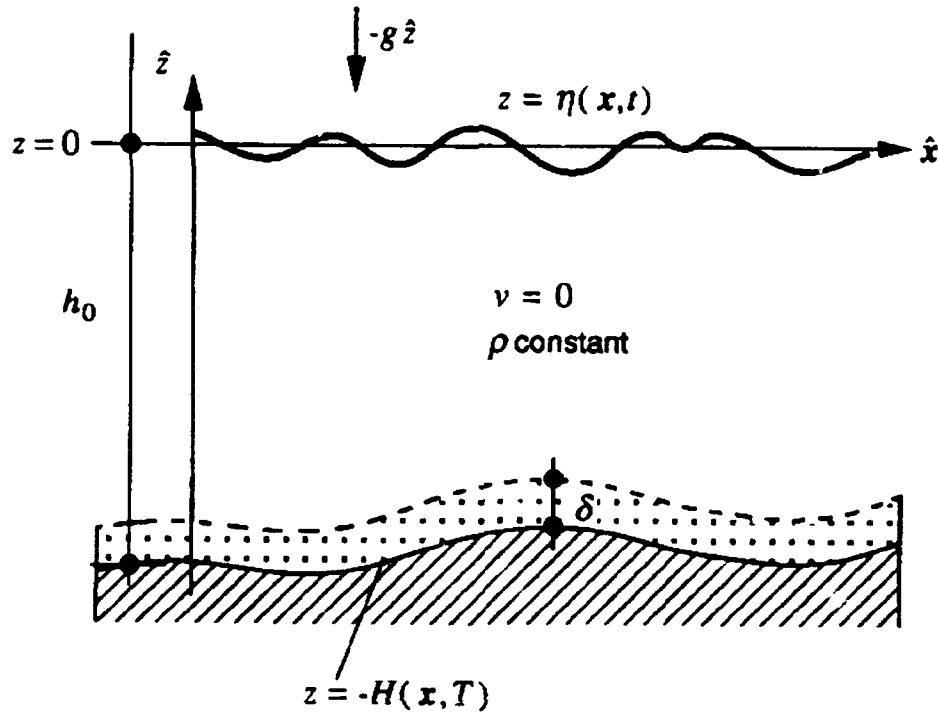
Figure 2.1: Side view, surface wave problem.

Since $\nabla_3 \times (\mathbf{u}, w) = 0$ is a possible solution of this equation, it follows that if the flow is initially irrotational, it shall remain as such for all time.

Since the fluid motion is irrotational, the velocity may be expressed as the gradient of a scalar potential φ:

$$(\mathbf{u}, w) = \nabla_3 \varphi. \tag{2.16}$$

From conservation of mass, Equation (2.4), the equation of motion within the fluid is

$$\Delta_3 \varphi = 0, \text{ in } \Omega. \tag{2.17}$$

At the air-water interface, conservation of momentum requires the pressure to be continuous. The assumed constant value of the pressure immediately above the water is set to zero. Hence, the pressure at the interface when the surface is quiescent shall be

zero. This dynamical boundary condition then specifically states that

$$\phi_t = -\frac{1}{2}|\nabla_3\phi|^2 - g\eta, \text{ at } z = \eta. \tag{2.18}$$

The bottom, which is assumed impermeable, has a normal velocity that agrees with that of the fluid. Thus,

$$\phi_z = -\nabla H \cdot \nabla \phi, \text{ at } z = -H. \tag{2.19}$$

Lastly, the kinematic condition on the air-water interface, that fluid particles on the surface shall remain there for all time, may be expressed as

$$\phi_z = \eta_t + \nabla\phi \cdot \nabla\eta, \text{ at } z = \eta. \tag{2.20}$$

Equations (2.17)-(2.20) with the additional requirement that $|\nabla\phi| \to 0$ as $|\mathbf{r}| \to \infty$ comprise the hydrodynamic problem.

Wave-like solutions of the above boundary value problem can easily be derived if the waves are infinitessimal in amplitude. Solutions of the form $\exp\{i(\mathbf{K}\cdot\mathbf{r} - \omega(\mathbf{K})t)\}$ exist for the linearized version of the system, provided that the relation between the frequency ω and the wavenumber $\mathbf{K}$ is the "dispersion relation"

$$\omega^2 = g\kappa\tanh(\kappa H), \tag{2.21}$$

where $\kappa \equiv |\mathbf{K}|$, and it is understood that the dispersion is spacially dependent since $H = H(\mathbf{r}, T)$. Both κ and ω must be real if we are strictly interested in plane wave solutions.

2.2.1 Hamiltonian Formulation of the Hydrodynamic Problem

To obtain a Hamiltonian formulation of the hydrodynamic problem proposed above, it is noted that the motion of the entire fluid body will be determined once the free surface motion is known. Specifically, if the function η which describes the free surface, and the velocity potential at the free surface,

$$\Phi \equiv \phi(\mathbf{r}, z = \eta, t), \tag{2.22}$$

are known, then, for each t, η determines the domain Ω_T and Φ determines the corresponding ϕ, which is the unique solution to the hydrodynamic problem comprised of Equation (2.17) through Equation (2.20) and Equation (2.22), with the additional assumption that $|\nabla_3 \phi| \to 0$, as $|\mathbf{r}| \to \infty$. In what follows, we rely heavily on ideas developed by Zakharov [48], Miles [49], Bowman[1] [50] and especially Benjamin[2] [51,52].

Consider the Hamiltonian $E = E(\eta, \Phi)$. The choice of label E reflects the fact that the Hamiltonian for this problem is conserved and is numerically equal to the sum of the potential energy V, and the the kinetic energy K. As shown by Benjamin and Olver [52], the requirement that E be stationary with respect to independent variations of $\delta\Phi$ and $\delta\eta$ yields the following Hamiltonian system:

$$
\begin{aligned}
\eta_t &= \frac{\delta E}{\delta \Phi} \\
\Phi_t &= -\frac{\delta E}{\delta \eta},
\end{aligned}
\tag{2.23}
$$

where the derivatives are Gâteaux derivatives.[3]

---

[1]S. Bowman has unfortunately left science and is now an actuarian in England. He leaves behind some good work, some of it unpublished.

[2]Not to be out done by particle theorists, Benjamin has been –successfully so far– working on unifying fluid dynamics under a consistent mathematical framework. A possible name for his framework could be Super Hamiltonian Unified Theory.

[3]The first variation of the functional F in the direction $\mathbf{r}$ is defined here by $\frac{d}{d\varepsilon} F(\mathbf{r} + \varepsilon \dot{\mathbf{r}})_{\varepsilon=0} \sim \dot{\mathbf{r}} \mathcal{E} F$, where $\mathcal{E}$ is the Eulerian derivative.

To briefly demonstrate the equivalence of the Hamiltonian system and the hydrodynamic problem consider the following: The energy in the system is

$$E = T + V = \int_{\mathbf{R}^2} d^2r \int_{-H}^{\eta} \frac{1}{2} |\nabla_3 \phi|^2 dz + \int_{\mathbf{R}^2} d^2r \frac{1}{2} g \eta^2 \qquad (2.24)$$

exactly. Extremizing E, keeping Φ constant and considering variations $\delta\eta$,

$$\delta E = \int_{\mathbf{R}^2} d^2r \delta\eta \{ \frac{1}{2} |\nabla_3 \phi|^2_{z=\eta} + g\eta \}, \qquad (2.25)$$

which leads to Equation (2.18). Next, keeping η constant and considering variations $\delta\Phi$, using Equation (2.17), and applying Green's theorem,

$$\delta E = \int_{-\infty}^{\infty} d\Sigma_s \delta\Phi(\Sigma_s) \hat{n}_{\Sigma_s} \cdot \nabla\phi|_{\Sigma_s} + \int_{-\infty}^{\infty} d\Sigma_B \delta\Phi(\Sigma_B) \hat{n}_{\Sigma_B} \cdot \nabla\phi|_{\Sigma_B}, \qquad (2.26)$$

where $\hat{n}$ is the outward normal to the boundaries. Since $d\Sigma_s = \sqrt{1 + (\nabla\eta)^2} d^2r$, and $d\Sigma_B = \sqrt{1 + (\nabla H)^2} d^2r$, the boundary contributions to Equation (2.26) are

$$\int_{\mathbf{R}^2} d^2r \delta\Phi \{ \phi_z - \nabla\eta \cdot \nabla\phi \}|_{z=\eta}, \qquad (2.27)$$

which leads to Equation (2.20), and

$$\int_{\mathbf{R}^2} d^2r \delta\Phi \{ \phi_z + \nabla H \cdot \nabla\phi \}|_{z=-H}, \qquad (2.28)$$

which implies Equation (2.19).

2.2.2 Development of the Boussinesq System

The Hamiltonian System, Equation (2.23), shall be specialized for the case of weakly nonlinear shallow water waves. Define the parameters $\alpha \ll 1$, and $\beta \ll 1$, their precise meaning, in terms of physically relevant parameters, shall be made clear subsequently.

Assume that $O(\alpha) \sim O(\beta^2)$, and take $H = O(1)$, $\nabla H = O(\alpha)$, $\eta = O(\alpha)$, $\Phi = O(\alpha)$. Further, consider the differentiations $\partial_z, \partial_t, \nabla = O(\beta)$.

An approximation to ϕ, which satisfies the boundary value problem is

$$\phi(\mathbf{r}, z, t) = \quad \Phi(\mathbf{r}, t) \quad - \quad \tfrac{1}{2}z^2\nabla^2\Phi(\mathbf{r}, t) \quad - \quad z\nabla\cdot(H\nabla\Phi(\mathbf{r}, t))$$

$$O(\alpha) \qquad\qquad O(\alpha\beta^2) \qquad\qquad O(\alpha\beta^2)$$

which can be easily derived using Rayleigh's trick[4] [53]. The gradient of the above expression

$$\mathbf{U}(\mathbf{r}, z, t) = \mathbf{u}(\mathbf{r}, t) - \{z\nabla[\nabla\cdot(H\mathbf{u}(\mathbf{r}, t))] + \frac{1}{2}z^2\nabla(\nabla\cdot\mathbf{u}(\mathbf{r}, t))\} \tag{2.29}$$

gives the velocity anywhere in the inviscid domain of the fluid.

The potential energy is exactly

$$V = \int_{\mathbf{R}^2} d^2r \frac{1}{2}g\eta^2. \tag{2.30}$$

The kinetic energy will be calculated using the approximation developed above for the velocity potential developed above, Equation (2.29):

$$K = \int_{\mathbf{R}^2} d^2r\{\frac{1}{2}(H + \eta)(\nabla\Phi)^2 + \frac{H}{2}(\nabla H\cdot\nabla\Phi)^2 - \frac{H^3}{6}(\nabla^2\Phi)^2\}, \tag{2.31}$$

which is an expression of $O(\alpha^3\beta^2)$, and $O(\alpha^2\beta^4)$.

Thus, in terms of the velocity at the surface $\mathbf{u} \equiv \nabla\Phi$, and the displacement, the energy is

$$E = V + K_0 + \alpha K_1 + \cdots, \tag{2.32}$$

---

[4]The trick was first used in connection with the solution of the electrostatic field in an axisymmetric strip, unbounded in x, say, and bounded by smooth but spatially varying edges in y. The harmonic functions φ and ψ representing the potential and the stream function are expanded as $\varphi = cos(y\partial_x)f$, and $\psi = sin(y\partial_x)f$, where f is determined termwise in the expansion in terms of the boundary conditions. Thanks are due to Prof. T. B. Benjamin for showing me this trick, and for introducing me to all matters Hamiltonian.

where

$$K_0 = \int\limits_{\mathbf{R}^2} d^2r \frac{1}{2} H \mathbf{u}^2 \tag{2.33}$$

$$K_1 = \int\limits_{\mathbf{R}^2} d^2r \{\frac{1}{2}\eta\mathbf{u}^2 + \frac{H}{2}(\nabla H \cdot \mathbf{u})^2 - \frac{H^3}{6}(\nabla\cdot\mathbf{u})^2\}, \tag{2.34}$$

and V is as before. Substituting E in Equation (2.23), to lowest order, yields the wave equation

$$\eta_t + \nabla\cdot(H\mathbf{u}) = 0 \tag{2.35}$$

$$\mathbf{u}_t + g\nabla\eta = 0. \tag{2.36}$$

To the next order,

$$\eta_t + \nabla\cdot[(H+\eta)\mathbf{u}] + \nabla\cdot[\mathbf{u}\nabla(H^2)\cdot\nabla H + \frac{1}{3}\nabla(H^3\nabla\cdot\mathbf{u})] = 0 \tag{2.37}$$

$$\mathbf{u}_t + (\mathbf{u}\cdot\nabla)\mathbf{u} + g\nabla\eta = 0, \tag{2.38}$$

a version of a Boussinesq System [44]. The Boussinesq System (BSS) is a shallow water– long-wavelength– weakly nonlinear approximation to the Euler Equation which admits bi-directional waves as solutions. The version given by Equation (2.37) and Equation (2.38), however, has a couple of troublesome characteristics from the standpoint of modelling a physical situation. Namely, the system is linearly unstable, and secondly, it is rather poor in conveying accurately the full dispersion relation.

The first problem may be seen as follows: without loss of generality, consider the one-dimensional version of BBS, dropping all nonlinear terms, setting $g = 1$, and considering, for simplicity, the case of a uniformly flat bottom. Additionally, let $\hat{u}(\kappa, t)$ be the Fourier transform in space of $u(x, t)$. Cross differentiating and combining Equation (2.37) and

Equation (2.38), the resulting equation is

$$u_{tt} - u_{xx} - \frac{1}{3}u_{xxxx} = 0,$$ (2.39)

or equivalently,

$$\hat{u}_{tt}(\kappa) = (-\kappa^2 + \frac{1}{3}\kappa^4)\hat{u}(\kappa),$$ (2.40)

for which a solution is

$$\hat{u}(\kappa, t) = \hat{u}(\kappa, 0)\{A\exp(\sqrt{\frac{1}{3}\kappa^4 - \kappa^2}t) + B\exp(-\sqrt{\frac{1}{3}\kappa^4 - \kappa^2}t)\}.$$ (2.41)

It is then immediately obvious that the solution can grow $\propto \exp(\sqrt{\frac{1}{3}}\kappa^2 t)$. The second problem is that the dispersion relation satisfied by Equation (2.39),

$$\omega^2 - \kappa^2(1 - \frac{1}{3}\kappa^2) = 0$$ (2.42)

is an adequate approximation to the Equation (2.21) strictly for very low frequencies as shall be demonstrated graphically in a subsequent section.

2.2.3 Regularization and Scaling

An ad-hoc procedure which "regularizes" BBS shall enable us to proceed in our development. As an alternative model to the Korteweg-deVries equation (KdV), Peregrine [54] developed an equation which has eventually been referred to as the "Regularized Long Wave Equation". While Peregrine was the first to propose it as an alternative to the KdV, it was Benjamin, Bona, Mahony [55] who later, but independently, proposed a regularized version of KdV, with the express intention of overcoming some of its shortcomings in modelling water waves, and who studied the resulting model's properties. The trick is to use the lowest order continuity and momentum balances in the higher order dispersive terms in order to obtain an equation which is more amenable to physical and computational studies. This procedure is justified on the grounds that the error in

making the substitution into the dispersive term, which is a higher order term, shall be no worse than the error already present in the original system. We shall employ a similar technique here, exploiting the specific form of the bottom topography, being careful not to destroy the bi-directional nature of the wave solutions.

Using Equation (2.36), and the fact that $\nabla H = O(\varepsilon)$, approximate

$$\nabla \cdot [\mathbf{u} \nabla (H^2) \cdot \nabla H + \frac{1}{3} \nabla (H^3 \nabla \cdot \mathbf{u})] = -\frac{1}{3} \nabla \cdot [\nabla (H^2 \eta_t)] + O(\alpha, \varepsilon). \qquad (2.43)$$

Thus, the regularized system (RB) adopted in this study, as an approximate model for the water waves, is

$$\eta_t + \nabla \cdot [(H + \eta)\mathbf{u}] - \frac{1}{3} \nabla \cdot [\nabla (H^2 \eta_t)] = 0 \qquad (2.44)$$

$$\mathbf{u}_t + (\mathbf{u} \cdot \nabla)\mathbf{u} + g \nabla \eta = 0. \qquad (2.45)$$

Several comments are in order. First of all, the dispersion relation of RB is

$$\omega^2 - \frac{\kappa^2}{1 + \frac{1}{3}\kappa^2} = 0. \qquad (2.46)$$

For plane wave propagation, both ω and κ must be real. A comparison of Equation (2.42) and Equation (2.46) shows that the upper limit for ω real is $|\kappa| = \sqrt{3}$ for the BSB system, while there's no limit on RB. Incidentally, another alternative Boussinesq System, the version used by Lau and Barcilon [40] results in a dispersion relation

$$\omega^2 - \kappa^2 + \frac{1}{3}\kappa^3 \omega = 0. \qquad (2.47)$$

This dispersion not only has a cutoff, but is also not symmetric about $\kappa = 0$, which implies incorrectly that wave propagation in the forward and backward directions are different. Figure(2.2) illustrates how the dispersion relations, Equation (2.42) and Equation (2.46),

compare to the full gravity wave dispersion relation. Equation (2.21). Both H and g were set to unity and $\beta = 0.5$ in the figure.
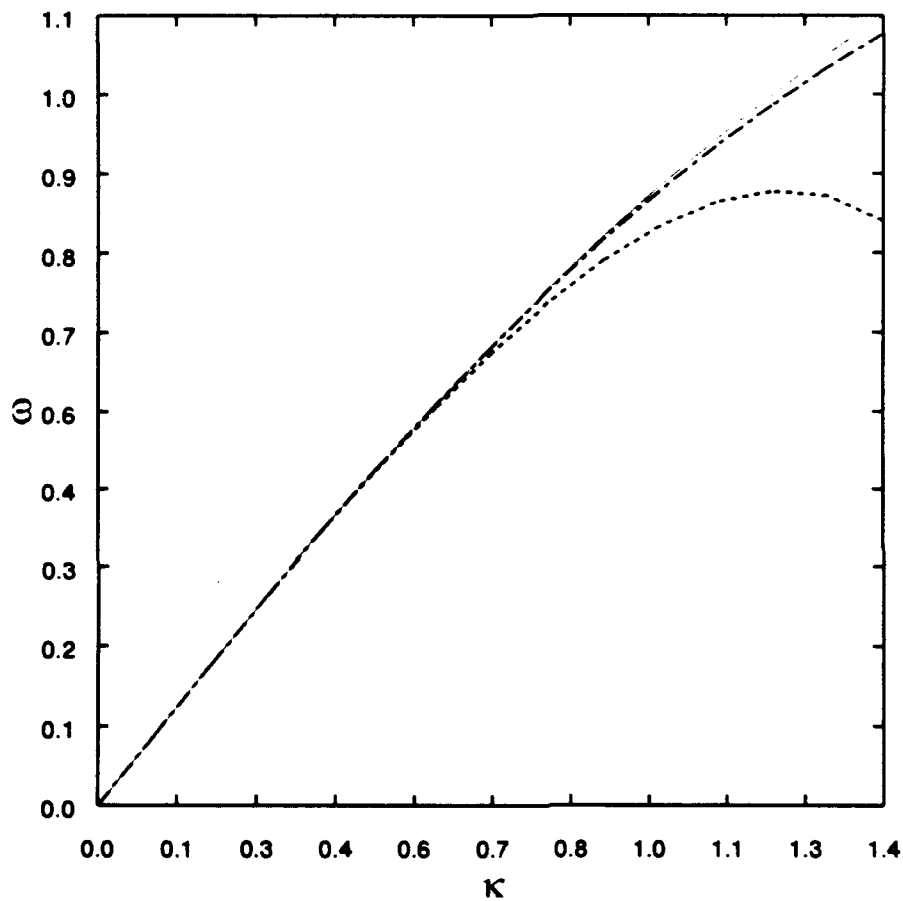
Figure 2.2: Comparison of the full water wave dispersion relation: —————-. BSB: -
- - - - - - -, RB: — — · — —· — —.

Regularization, as performed here, does bring a couple of subtleties that must be kept in mind: (1) Since we are using the lowest order relations, we are assuming that the solutions are wave-like. However, there is no reason to expect that the solution will approximate a traveling wave solution for arbitrary Cauchy data. (2) We have preserved two-way wave propagation. In most instances when regularization is performed, the

Boussinesq equation that results is applicable to strictly one-way wave motion. (3) Since the velocity is in terms of the surface values, rather than in terms of averaged-depth velocity, say, the irrotational condition, with u and v being respectively the shoreward and span-wise velocity components, remains in the simple form

$$u_y = v_x, \tag{2.48}$$

which is quite convenient in the development of three-dimensional problems.

In order to scale the hydrodynamical model developed in the previous section, define a parameter related to the size of the amplitude of the disturbance, and another related to the size of spatial–or temporal–changes. The first one is $\alpha \equiv a/h_0$, which gives an estimate of the degree of nonlinearity in the problem. The second is $\beta^2 \equiv (\lambda/h_0)^2$, which conveys the degree in which dispersive effects are important. The Stokes number, which is a measure of the balance between nonlinear to dispersive effects is defined as the ratio α/β^2. For $U \ll 1$, nonlinear effects are weak, and only a small portion of energy transfer occurs on moderate space-time scales, so that $O(1)$ nonlinear effects are possible only after very large scales. For $U \sim 1$, inertial effects are of the same order as dispersive effects.

Using the convention in what follows that $new \leftarrow scale \times old$, the scaling adopted is

$$t \leftarrow \frac{\sqrt{gh_0}\,t}{\lambda} \quad \mathbf{u} \leftarrow \frac{\sqrt{h_0}\,\mathbf{u}}{\sqrt{g}\,a} \quad \eta \leftarrow \eta/a \quad h \leftarrow \frac{H}{h_0} \quad \mathbf{r} \leftarrow \frac{\mathbf{r}}{\lambda} \tag{2.49}$$

where h_0 is a characteristic depth of the water column.

In addition, we seek to scale span-wise dependence to reflect the fact that we are interested in a case of propagation that is primarily shoreward directed. To do so, it is

assumed that there is a const $\ll$ 1 such that

$$O(|\hat{x}\cdot\mathbf{K}|) = const \times O(|\hat{y}\cdot\mathbf{K}|), \qquad (2.50)$$

for which a consistent uniform expansion of the RB exits, and that is physically relevant. It may be shown that the size of the constant is of the order of the reciprocal of β. Since this parameter has considerable nuisance value, the parameter shall be set $const = 1/\beta$ for the rest of this study. This implies that the span-wise variables must be scaled

$$y \leftarrow \alpha^{1/2}y \qquad \hat{y}\cdot\mathbf{u} \leftarrow \alpha^{-1/2}\hat{y}\cdot\mathbf{u}, \qquad (2.51)$$

which shall alter the regularized system, but shall not affect the irrotational condition, Equation (2.48).

2.2.4 Description of the Bottom Topography

Field data from the continental shelf suggests that there are two time scales, a fast time scale t which measures the evolution of the fluid quantities, and a large time scale T which measures the evolution of the bottom topography. In addition the data suggests that the typical height and slopes of the longshore sand ridges is such that $\varepsilon = O(\nabla^n h) = O(\alpha)$. Furthermore, the type of longshore sand ridge under consideration is such that the measure of longshore spatial variation is larger than the spatial variations of the fluid quantities. It is proposed that the sand ridge shoreward variation be $X = \alpha x$. Hence, two scales of shoreward variation exist, so that

$$\partial_x \rightarrow \partial_x + \alpha\partial_X. \qquad (2.52)$$

Thus the bottom in scaled variables is

$$h(X, y, T) = 1 + \varepsilon f(X, y, T), \qquad (2.53)$$

where the function $f = O(1)$.

2.2.5 Slightly Resonant Interacting Triads

By substituting a uniform expansion of the form

$$\eta = f_0 + \alpha^1 f_1 + \alpha^2 f_2 + \cdots$$

$$\mathbf{u} = \mathbf{g}_0 + \alpha^1 \mathbf{g}_1 + \alpha^2 \mathbf{g}_2 + \cdots \qquad (2.54)$$

into Equations(2.44), (2.45), and (2.48), matching order by order we are able to solve for the surface quantities to lowest orders in α.

For the momentum equation, Equation (2.45), the first three orders are

$$
\begin{aligned}
\alpha^0 : && u_{0t} + \eta_{0x} &= 0 \\
&& v_{0t} + \eta_{0y} &= 0 \\
\alpha^1 : && u_{1t} + u_0 u_{0x} + \eta_{1x} + \eta_{0X} &= 0 \\
&& v_{1t} + u_0 v_{0x} + \eta_{1y} &= 0 \\
\alpha^2 : \quad u_{2t} + u_1 u_{0x} + u_0 u_{1x} + u_0 u_{0X} + v_0 u_{0y} + \eta_{2x} + \eta_{1X} &= 0 \\
v_{2t} + u_1 v_{0x} + u_0 v_{1x} + u_0 v_{0X} + \eta_{2y} &= 0
\end{aligned}
\qquad (2.55)
$$

Similarly, for the irrotational equation, Equation (2.48), we have

$$
\begin{aligned}
\alpha^0 : && u_{0y} - v_{0x} &= 0 \\
\alpha^1 : && u_{1y} - v_{1x} - v_{0X} &= 0 \\
\alpha^2 : && u_{2y} - v_{2x} - v_{1X} &= 0.
\end{aligned}
\qquad (2.56)
$$

Finally, Equation (2.44) yields

$$
\begin{aligned}
\alpha^0 : && \eta_{0t} + u_{0x} - \frac{\beta^2}{3}\eta_{0xxt} &= 0 \\
\alpha^1 : && \eta_{1t} + u_{1x} - \frac{\beta^2}{3}\eta_{1xxt} &= F_1(\eta_0, u_0, v_0, G; x, X, y, t) \\
\alpha^2 : && \eta_{2t} + u_{2x} - \frac{\beta^2}{3}\eta_{2xxt} &= F_2(\eta_0, u_0, v_0, \eta_1, u_1, v_1, G; x, X, y, t),
\end{aligned}
\qquad (2.57)
$$

where $G(X, y, T) = \frac{\varepsilon f(X, y, T)}{\alpha}$,

$$F_1 = -v_{0y} + \frac{\beta^2 \eta_{0yyt}}{3} - u_{0X} - u_0\eta_{0x} - Gu_{0x} - \eta_0 u_{0x} + \frac{2\beta^2(\eta_{0x}X_t + G\eta_{0xxt})}{3} \qquad (2.58)$$

and

$$\begin{aligned}
F_2 =\ & -v_{1y} + \frac{\beta^2 \eta_{1yyt}}{3} - u_{1X} - u_1\eta_{0x} - Gu_{1x} - \eta_1 u_{0x} + \frac{2\beta^2(\eta_{1x}X_t + G\eta_{1xxt})}{3} \\
& -u_0\eta_{1x} - \eta_0 u_{1x} - G_y v_0 - G_X u_0 - v_0\eta_{0y} - Gv_{0y} - \eta_0 v_{0y} + \frac{2\beta^2(G\eta_{0t})_{yy}}{3} \qquad (2.59) \\
& -u_0\eta_{0X} - Gu_{0X} - \eta_0 u_{0X} + \frac{\beta^2 \eta_{0XXt}}{3} + \frac{4\beta^2 G_X \eta_{0xt}}{3} + \frac{4\beta^2 G\eta_{0xXt}}{3}.
\end{aligned}$$

Making use of the appropriate irrotational condition when a simplification is possible, cross-differentiating the momentum and continuity equations, and combining the results into a single equation yields

$$\begin{aligned}
\alpha^0 :\ & \mathcal{L}\eta_0\ = 0 \\
\alpha^1 :\ & \mathcal{L}\eta_1\ = \mathcal{G}_1(\eta_0, u_0, v_0, G; x, X, y, t) \qquad (2.60) \\
\alpha^2 :\ & \mathcal{L}\eta_2\ = \mathcal{G}_2(\eta_0, u_0, v_0, \eta_1, u_1, v_1, G; x, X, y, t),
\end{aligned}$$

where

$$\mathcal{L}\ =\ \partial_{tt} - \partial_{xx} - \frac{\beta^2}{3}\partial_{xxtt}. \qquad (2.61)$$

Note that $\mathcal{L}$ is a linear operator that shows up at every order. The inhomogeneous terms, $\mathcal{G}_1$ and $\mathcal{G}_2$ are, respectively,

$$\begin{aligned}
\mathcal{G}_1\ =\ & (1 + \beta^2\partial_{tt}/3)\eta_{0yy} + G(1 + 2\beta^2\partial_{tt}/3)\eta_{0xx} + 2(1 + \beta^2\partial_{tt}/3)\eta_{0xX} \\
& + (u_0^2/2)_x - (u_0\eta_0)_{xt},
\end{aligned} \qquad (2.62)$$

$$
\begin{aligned}
\mathcal{G}_2 &= (1 + \beta^2\partial_{tt}/3)\eta_{1yy} + G(1 + 2\beta^2\partial_{tt}/3)\eta_{1xx} + 2(1 + \beta^2\partial_{tt}/3)\eta_{1xX} \\
&\quad (1 + \beta^2\partial_{tt}/3)\eta_{0XX} + G(1 + 2\beta^2\partial_{tt}/3)\eta_{0yy} + 2(1 + \beta^2\partial_{tt}/3)\eta_{0xX} \\
&\quad + G_X(1 + 4\beta^2\partial_{tt}/3) + \eta_{0x} + G_y\eta_{0y} + 2\beta^2 G_{yy}\eta_{0tt}/3 + 4\beta^2 G_y\eta_{0tyy}/3 \quad (2.63) \\
&\quad - (\eta_1 u_0 + \eta_0 u_1)_{xt} + (u_1 u_0)_{xx} + (u_0^2)_x X - (u_0\eta_0)_{Xt} + G(u_0^2/2)_{xx} \\
&\quad + (u_0^2/2)_{yy} + (v_0^2/2)_{xx} + (\eta_0^2/2)_{yy} - (\eta_{0t}v_0)_y.
\end{aligned}
$$

Beyond this order the calculation of the uniform expansion is invalid since it is beyond the order to which RB is an approximation to Euler's Equations. The lowest-order theory is suitable since we are only interested in phenomenology, rather than engineering accuracy. Appendix A gives the reader an idea of the sort of things to expect at $O(\alpha^1)$.

The order of RB and the two-scale technique restrict the region of validity of the present model. The lowest order solutions, which are linear, are valid for distances that are less than $O(1/k\alpha)$, the scale over which triads of Fourier modes exchange significant energy. Higher order terms and processes neglected in the expansion restrict the range of the present nonlinear solutions to distances less than $O(1/k\alpha^2)$. Thus, RB is not formally valid for very long evolution distances. Boussinesq equations are strictly valid for $U = O(1)$, but they are quite robust [41]. In this study, the value of U is in the range of 10 to 30.

Assume the shoreward velocity is

$$
\begin{aligned}
u(x, X, y, t) &= \int_{-\infty}^{\infty}[a(k, X, y) + \alpha A(k, X, y)]e^{i(kx - \omega t)}dk + c.c. \\
&\quad + \int_{-\infty}^{\infty}[b(k, X, y) + \alpha B(k, X, y)]e^{i(-kx - \omega t)}dk + c.c.
\end{aligned} \quad (2.64)
$$

where $k \equiv \hat{x}\cdot K$, and further, assume that such solution may be approximated by the

discrete Riemann sum

$$
\begin{aligned}
u(x,X,y,t) &= \sum_{j=1}^{\infty}[a_j(X,y)+\alpha A_j(X,y)]e^{i(k_j x-\omega_j t)} + c.c. \\
&\quad + \sum_{j=1}^{\infty}[b_j(X,y)+\alpha B_j(X,y)]e^{i(-k_j x-\omega_j t)} + c.c.,
\end{aligned}
\tag{2.65}
$$

where c.c. stands for complex conjugate of the expression immediately preceeding its appearance. The a's are the complex incident wave amplitudes, and the b's are the complex reflected wave amplitudes. The reality of the physical variables implies that $a_{-j} = a_j^*$ and $b_{-j} = b_j^*$. The span-wise velocity at the surface must then be

$$
\begin{aligned}
v(x,X,y,t) &= \sum_{j=1}^{\infty} -\frac{i}{k_j}[a_{jy}(X,y)+O(\alpha)]e^{i(k_j x-\omega_j t)} + c.c. \\
&\quad + \sum_{j=1}^{\infty} -\frac{i}{k_j}[b_j(X,y)+O(\alpha)]e^{i(-k_j x-\omega_j t)} + c.c.
\end{aligned}
\tag{2.66}
$$

in order to satisfy Equation (2.48). Since, to lowest order, $u_{0t}+\eta_{0x} = 0$, an expression for the surface amplitude is readily available: the replacement of the lowest order velocity into the momentum equation yields

$$
\begin{aligned}
\eta_0 &= \sum_{1}^{\infty} \frac{\omega_j}{k_j}[a_j(X,y)+\alpha A_j(X,y)]e^{i(k_j x-\omega_j t)} + c.c. \\
&\quad + \sum_{j=1}^{\infty} \frac{\omega_j}{k_j}[b_j(X,y)+\alpha B_j(X,y)]e^{i(-k_j x-\omega_j t)} + c.c.
\end{aligned}
\tag{2.67}
$$

A solution of the form given by Equations (2.65), (2.66) and (2.67) is valid, provided that the following relation holds between the frequency and the wavenumber:

$$
\omega_j^2 - \frac{k_j^2}{1 + \beta^2 \frac{k_j^2}{3}} = 0,
\tag{2.68}
$$

which gives the dispersion relation for the jth mode, the positive root k_j corresponding to the shoreward-directed wave, and the negative to the seaward wave.

The solution must also satisfy a compatibility condition. Since the linear operator $\mathcal{L}$ in Equation (2.60) appears in every order, and terms of lower order appear in the inhomogeneous part, secular terms arise. It is an artifice of having truncated the expansion,

and is typified by the possibility of blow-up due to resonance. This resonance condition for j^{th} interacting waves is,

$$
\begin{aligned}
k_j \pm \cdots \pm k_2 \pm k_1 &= 0 \\
\omega_j + \cdots + \omega_2 + \omega_1 &= 0.
\end{aligned} \tag{2.69}
$$

where the wavenumbers and corresponding frequencies obey the dispersion relation given by Equation (2.46). In the scaling adopted in this study the $O(k_j) = O(\omega_j)$.

The resonance condition is possible for certain wave systems. For isotropic waves, i.e. $\omega = \omega(\kappa)$, the resonance condition, with $\omega(0) = 0$, can always be satisfied if $\omega'(\kappa) > 0$, and $\omega''(\kappa) > 0$. These conditions cannot be satisfied if $\omega'(\kappa) > 0$, $\omega''(\kappa) < 0$.

To prove this, we note that the dispersion relation $\omega(\kappa)$ is convex downwards if $\omega''(\kappa) > 0$. Hence,

$$
\omega(|\kappa_2 - \kappa_1|) < \omega(\kappa_1) + \omega(\kappa_2) < \omega(\kappa_2 + \kappa_1). \tag{2.70}
$$

Let $\mathbf{K_3} = \mathbf{K_2} + \mathbf{K_1}$, so that when the angle between $\mathbf{K_2}$ and $\mathbf{K_1}$ changes between 0 and π, one has that $|\kappa_2 - \kappa_1| \leq \kappa_3 \leq |\kappa_2 + \kappa_1|$. Hence the frequency $\omega_3 = \omega_3(\kappa_3)$ will change continuously between $\omega(|\kappa_2 - \kappa_1|)$ and $\omega(\kappa_2 + \kappa_1)$, and will coincide with $\omega(\kappa_1) + \omega(\kappa_2)$ at some point. If $\omega''(\kappa) < 0$, however, we have $\omega(\kappa_1) + \omega(\kappa_2) > \omega(\kappa_2 + \kappa_1) \geq \omega(\kappa_3)$ and at such point coincidence is impossible.

Since the dispersion relation for gravity water waves is such that $\omega'(\kappa) > 0$, and $\omega''(\kappa) < 0$, perfect coincidence is not possible. At most we expect what we shall refer to as "weak resonance". Furthermore, we shall restrict our attention to the special weakly-resonant triad case in which $k_2 = 2k_1 - \delta$, $\omega_2 = 2\omega_1$, where the detuning parameter $\delta \leq 0$. The compatibility condition is that solutions of the α^{l+1} be orthogonal to the

solutions of order α^l and below, so that resonant solutions are avoided:

$$\frac{jk_1}{2\pi} \int_{X_0}^{X_0+2\pi/jk_1} e^{\pm ijk_1 x}(\mathcal{G}_j + \mathcal{G}_j^*)dx = 0, \text{where } j = 1, 2, 3..., \qquad (2.71)$$

starred quantities conjugated. The case of quartet interactions, to lowest order, appears in Appendix B, and is a straight-forward extention of the ideas presented here.

The justification for using a small number of modes comes from field data. Figure 2.3 suggests that most of the energy in the waves is found in the first few harmonics. This situation is quite typical. The figure also shows the shifting of energy from lower frequencies to higher ones as the wave travels shoreward over a decreasing water column depth.
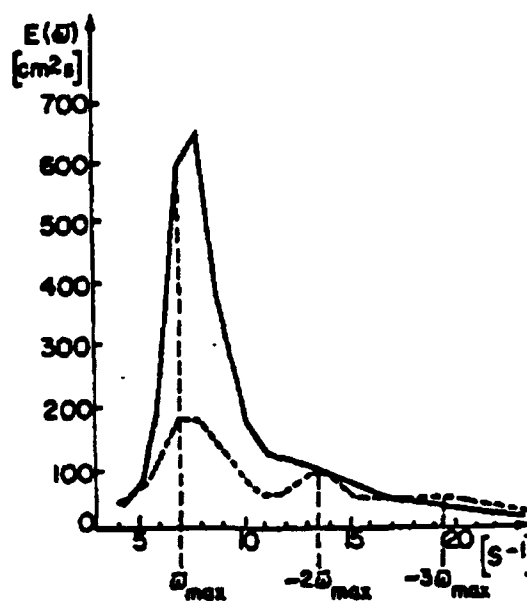
Figure 2.3: Energy for shallow water waves in the Southern Baltic Sea: $h_0 = 6.0m$ ——————-, $h_0 = 2.0m$ — — — — — — —-. From Druet et al. [56].

Application of the compatibility condition to the lowest order terms in Equation (2.63), yields, after some algebra, the evolution equations for the modes in Equation

(2.65), and Equation (2.67)

$$a_{1x} + i\varepsilon f D_1 E_1 a_1 - i\alpha F_1 a_{1yy} + i\alpha D_1 S_1 e^{-i\delta x} a_1^\star a_2 = 0$$

$$a_{2x} + i\varepsilon f D_2 E_2 a_2 - i\alpha F_2 a_{2yy} + i\alpha D_2 S_2 e^{+i\delta x} a_1^2 = 0$$

$$b_{1x} - i\varepsilon f D_1 E_1 b_1 + i\alpha F_1 b_{1yy} - i\alpha D_1 S_1 e^{+i\delta x} b_1^\star b_2 = 0$$

$$b_{2x} - i\varepsilon f D_2 E_2 b_2 + i\alpha F_2 b_{2yy} - i\alpha D_2 S_2 e^{-i\delta x} b_1^2 = 0.$$

(2.72)

to $O(\delta/X)$, after substituting back $X = ax$. The constants are

$$D_j = [2(1 - \beta^2 \tfrac{\omega_j^2}{3})]^{-1}$$

$$E_j = k_j(1 - \tfrac{2}{3}\beta^2 \omega_j^2)$$

$$F_j = 1/2k_j$$

$$S_1 = \tfrac{k_2 - k_1}{\omega_1}\{k_2 - k_1 + \omega_1(\tfrac{\omega_1}{k_1} + \tfrac{\omega_2}{k_2})\}$$

$$S_2 = 2k_1^2/\omega_2 + 2\omega_1^2$$

(2.73)

Equation (2.72), along with appropriate boundary conditions determines in an approximate way the ocean surface. The incident and reflected waves are decoupled owing to the assumptions and restrictions on the spatial variation of the bottom topography. If, on the other hand, the longshore sand ridges being considered were

$$h(x, X, y, T) = 1 + \varepsilon f(x, X, y, T)$$

(2.74)

the resulting modal equations, to lowest order, would be

$$a_{1x} - i\varepsilon f D_1 E_1 \gamma_1 a_1 + i\varepsilon f D_1 E_1 \mu_1^- b_1 - i\alpha F_1 a_{1yy} + i\alpha D_1 S_1 e^{-i\delta x} a_1^\star a_2 = 0$$

$$a_{2x} - i\varepsilon f D_2 E_2 \gamma_2 a_2 + i\varepsilon f D_2 E_2 \mu_2^- b_2 e^{2i\delta x} - i\alpha F_2 a_{2yy} + i\alpha D_2 S_2 e^{+i\delta x} a_1^2 = 0$$

$$b_{1x} + i\varepsilon f D_1 E_1 \gamma_1 b_1 - i\varepsilon f D_1 E_1 \mu_1^+ a_1 + i\alpha F_1 b_{1yy} - i\alpha D_1 S_1 e^{+i\delta x} b_1^\star b_2 = 0$$

$$b_{2x} + i\varepsilon f D_2 E_2 b_2 - i\varepsilon f D_2 E_2 e^{-i2\delta x} \mu_2^+ a_2 + i\alpha F_2 b_{2yy} - i\alpha D_2 S_2 e^{-i\delta x} b_1^2 = 0,$$

(2.75)

to $O(\delta/X)$, with

$$\gamma_j = \frac{jk_1}{2\pi} \int_0^{2\pi/jk_1} (f_{xx} + 2ik_j f_x - k_j^2 f)dx$$

$$\mu_j^- = \frac{jk_1}{2\pi} \int_0^{2\pi/jk_1} (f_{xx} + 2ik_j f_x - k_j^2 f)e^{-2ijk_1 x}dx$$

$$\mu_j^+ = \frac{jk_1}{2\pi} \int_0^{2\pi/jk_1} (f_{xx} + 2ik_j f_x - k_j^2 f)e^{+2ijk_1 x}dx. \tag{2.76}$$

The most striking difference between the way Equations(2.72) and (2.75) describe the surface is that in the former case, the bars do not act as scatterers, and all energy in the reflected component is put into it through the boundary conditions.

2.3 Internal Wave Case

Shallow water weakly nonlinear interfacial waves appear as highly coherent groups having well defined wavelength and are observed propagating shoreward on a density stratification, such as the picnocline. Their crests are generally oriented along isobaths [57,58]. Their wavelengths range from 200 to 1600 meters, depending on the depth, which can be considerably larger than the local water column depth. An estimate of the energy contained in the larger ones is in the order of $0.1 MJ/m^2$. They have been seen to appear twice a day in some areas, coinciding with the tidal cycle, and originate mostly in places where there are sharp changes in the bottom topography, such as on the edge of the continental shelf.

2.3.1 Internal Wave Hydrodynamic Problem

In this section the Hamiltonian formulation to the two-fluid internal wave problem is developed, relying on Bowman's work [50]. Illustrated in Figure 2.4, define the domain $\Omega_1 \approx \mathbf{R}^2 \times [-H, \eta]$, and $\Omega_2 = \mathbf{R}^2 \times [\eta, D]$. The lower layer (1) has a uniform density ρ_1, and the upper layer (2) a density $\rho_2 < \rho_1$. The fluid is subjected solely to gravitational

forcing. The velocity field is now given in each layer by $(\mathbf{u}, w)_i$, where the subscript refers to layer 1 or 2. The interface between the two fluids is given by $z = \eta(\mathbf{r}, t)$ and the bottom by $z = -H(\mathbf{r}, T)$.
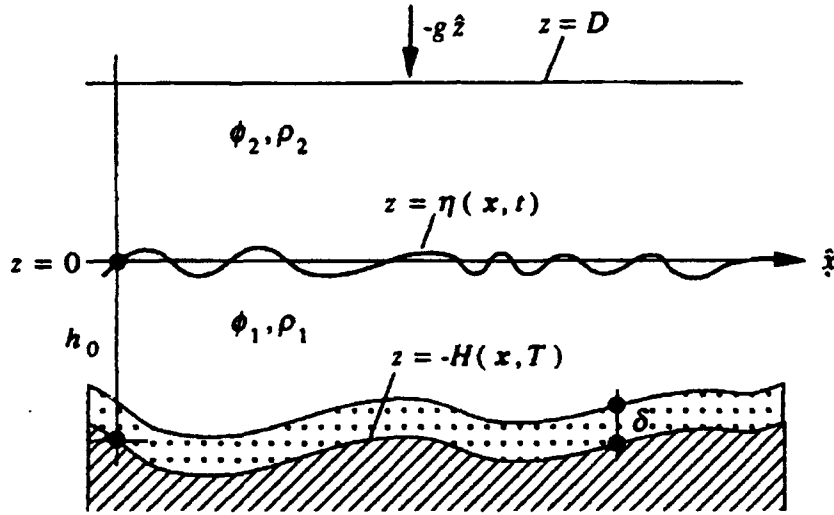
Figure 2.4: Side view, internal wave problem.

Assume the fluid is incompressible and irrotational in each layer. In terms of a scalar potential, the velocity is given by

$$(\mathbf{u}, w)_i = \nabla_3 \phi_i. \tag{2.77}$$

From conservation of mass, Equation (2.4), the equations of motion within the fluid are

$$\Delta_3 \phi_i = 0, \text{ in } \Omega_i. \tag{2.78}$$

At the interface, the pressure is continuous, hence the dynamical boundary condition is

$$\phi_{i,t} = -\frac{1}{2} |\nabla_3 \phi_i|^2 - g\rho_i \eta, \text{ at } z = \eta. \tag{2.79}$$

The bottom, which is assumed impermeable, has a normal velocity that agrees with that of the fluid. Thus

$$\phi_{1,z} = -\nabla H \cdot \nabla \phi_1 \text{ at } z = -H. \tag{2.80}$$

The kinematic condition on the interface is again $\frac{D(z-\eta)}{Dt} = 0$, or

$$\phi_{i,z} = \eta_t + \nabla \phi_i \cdot \nabla \eta \text{ at } z = \eta. \tag{2.81}$$

Finally, we make the simplifying assumption that the normal velocity disappears at the constant air-water interface:

$$\phi_{2,z} = 0, \text{ at } z = D. \tag{2.82}$$

2.3.2 Hamiltonian Formulation of the Internal Wave Problem

The conjugate variables in this case are η and $\mathbf{U} \equiv \rho_2 \nabla \phi_2 - \rho_1 \nabla \phi_1$. The Hamiltonian system takes the form

$$\eta_t = -\nabla \cdot (\frac{\delta E}{\delta U})$$
$$\mathbf{U}_t = -\nabla (\frac{\delta E}{\delta \eta}). \tag{2.83}$$

By virtue of the boundary conditions at the air-water interface, the results from the previous section shall be exploited to arrive at a regularized Boussinesq equation for the internal wave case. The potential energy is simply

$$V = \int_{\mathbf{R}^2} d^2 r \frac{1}{2} g(\rho_1 - \rho_2)\eta^2. \tag{2.84}$$

The total kinetic energy is the sum of contributions from both layers, thus

$$K = \rho_1 \int_{\mathbf{R}^2} d^2 r \int_{-H}^{\eta} \frac{1}{2} |\nabla_3 \phi_1|^2 dz + \rho_2 \int_{\mathbf{R}^2} d^2 r \int_{-\eta}^{D} \frac{1}{2} |\nabla_3 \phi_2|^2 dz = K_1 + K_2. \tag{2.85}$$

The kinetic energy in the lower layer is given by Equation (2.31). We need only to figure

out K_2. The boundary condition given by Equation (2.82) can be exploited to find K_2 as a surface integral, using Green's theorem. Assuming the gradients of the potential tend to zero as $|\mathbf{r}| \to \infty$,

$$K_2 = - \int\limits_{\mathbf{R}^2} d^2 r \rho_2 \nabla \Phi_1 \nabla \Phi_2. \tag{2.86}$$

Define the pseudo-differential operator $G \equiv -k \coth(HkD)$, which comes from satisfying the boundary conditions on the interface and on the ocean surface. Adding the expressions for K_1 and K_2, using the definition of $\mathbf{U}$, and the operator G, the total kinetic energy is

$$K = \frac{1}{2} \int\limits_{\mathbf{R}^2} d^2 r \{ \frac{1}{\rho_1}(H + \eta)\mathbf{U}^2 + \frac{H^2 \rho_2}{\rho_1^2} \mathbf{U} \cdot G\mathbf{U} + \frac{\rho_2 H}{\rho_1^2}(\nabla H \cdot \mathbf{U})^2 \} + O(\alpha^3 \beta^2), \tag{2.87}$$

or rearranging,

$$K = \frac{1}{2} \int\limits_{\mathbf{R}^2} d^2 r \{ \frac{1}{\rho_1}[(H + \eta) - \frac{H^2 \rho_2}{\rho_1^2 D}]\mathbf{U}^2 + \frac{H^2 \rho_2}{\rho_1^2} \mathbf{U} \cdot M\mathbf{U} + \frac{\rho_2 H}{\rho_1^2}(\nabla H \cdot \mathbf{U})^2 \} + O(\alpha^3 \beta^2),$$

$$\tag{2.88}$$

where $M = \frac{1}{D} + G = \frac{1}{D} - k \coth(HkD)$.

Depending on the size of D/λ, there are three physically distinct possibilities:

- if $D/\lambda \ll 1$, then $\mathbf{U} \cdot M\mathbf{U} = O(\alpha^2 D/\lambda^2)$, and $M \approx 1/D - \frac{D\nabla^2}{3}$. For such case, the terms $\eta \mathbf{U} \cdot \mathbf{U}$ and $\mathbf{U} \cdot M\mathbf{U}$ balance if $\alpha^2 D/\lambda^2 \sim 1$. We obtain a Boussinesq system.

- for $D/\lambda \sim 1$ then $\mathbf{U} \cdot M\mathbf{U} = O(\alpha^2/\lambda)$. In such case, if $\alpha\lambda^2/D \sim 1$, we obtain the Intermediate Long-Wave equation.

- Finally, $D/\lambda \gg 1$, so that $\mathbf{U} \cdot M\mathbf{U} = O(\alpha^2/\lambda)$, then $M \approx |k|$. If $\alpha\lambda \sim 1$, the result is the Benjamin-Ono equation.

Note that this last case corresponds to a very deep upper layer, lying over a thinner lower layer, which we do not consider relevant to the problem in this study.

By substituting the expressions for the potential and kinetic energy, Equation (2.84) and Equation (2.88), into Equation (2.83), the general dynamical equation for the dynamics of the internal wave field is obtained:

$$\eta_t = -\nabla\cdot\{[\frac{1}{\rho_1}(H+\eta)-\frac{H^2\rho_2}{\rho_1^2 D}]\mathbf{U}\} - \frac{\rho_2}{\rho_1^2}\nabla\cdot\{H(\nabla H)^2\mathbf{U}+H^2 M\mathbf{U}\}$$
$$\mathbf{U}_t = -\nabla\cdot\{\frac{1}{2\rho_1^2}\mathbf{U}\cdot\mathbf{U}+(\rho_1-\rho_2)g\eta\}. \tag{2.89}$$

The result from linear theory can be recovered by neglecting second and higher order terms in Equation (2.89). The solutions proportional to $\exp\{i(kx-\omega t)\}$ satisfy

$$\omega\eta = (\frac{1}{\rho_1}-\frac{\rho_2 H}{\rho_1^2 D}+\frac{\rho_2 HM}{\rho_1^2})kHU$$
$$\omega U = k(\rho_1-\rho_2)g\eta. \tag{2.90}$$

Thus,

$$c^2 \equiv \frac{\omega^2}{k^2} = \frac{g(\rho_1-\rho_2)}{\rho_1}[1-\frac{\rho_2}{\rho_1}Hk\coth(kD)]. \tag{2.91}$$

The relevant case in this study is the first one. The Boussinesq equation is then

$$\eta_t = -\nabla\cdot\{\frac{1}{\rho_1}(H+\eta)\mathbf{U}\} - \frac{\rho_2}{\rho_1^2}\nabla\cdot\{H(\nabla H)^2\mathbf{U}+\frac{1}{3}H^2 D\nabla\nabla\cdot\mathbf{U}\}$$
$$\mathbf{U}_t = -\nabla\cdot\{\frac{1}{2\rho_1^2}\mathbf{U}\cdot\mathbf{U}+(\rho_1-\rho_2)g\eta\}. \tag{2.92}$$

2.3.3 Regularization and Scaling

The lowest order relations

$$\eta_t = -\nabla\cdot\{\frac{1}{\rho_1}H\mathbf{U}\}$$
$$\mathbf{U}_t = -\nabla\{(\rho_1-\rho_2)g\eta\} \tag{2.93}$$

are used in a manner similar to the surficial case to modify the troublesome parts of the dispersive terms to get the model for the hydrodynamics relevant in this study:

$$\eta_t = -\nabla\cdot\{\frac{1}{\rho_1}(H+\eta)\mathbf{U}\} + \frac{D\rho_2}{3\rho_1^2}\nabla\cdot[\nabla(H\eta_t)]$$
$$\mathbf{U}_t = -\nabla\{\frac{1}{2\rho_1^2}\mathbf{U}\cdot\mathbf{U}+(\rho_1-\rho_2)g\eta\}. \tag{2.94}$$

The scaling is the same as the surficial case, except that U has units of momentum.

Let $\gamma \equiv \frac{(\rho_1 - \rho_2)}{\rho_1}$ be the Boussinesq parameter, and the typical thickness of the lower layer be h_0. The scaling adopted here is

$$t \leftarrow \frac{\sqrt{gh_0}t}{\lambda} \quad \mathbf{U} \leftarrow \frac{\sqrt{h_0}\mathbf{U}}{\sqrt{ga}} \quad \eta \leftarrow \eta/a \quad h \leftarrow \frac{H}{h_0} \quad d \leftarrow \frac{D}{h_0} \quad \mathbf{r} \leftarrow \frac{\mathbf{r}}{\lambda}. \tag{2.95}$$

Equation (2.94) is, in scaled variables,

$$\begin{aligned}
\eta_t + \nabla\cdot\{\frac{1}{\rho_1}(h + \alpha\eta)\mathbf{U}\} - d\beta^2\frac{\rho_2}{3\rho_1}\nabla\cdot[\nabla(h\eta_t)] &= 0 \\
\mathbf{U}_t + \nabla\{\frac{1}{2}\mathbf{U}\cdot\mathbf{U} + \gamma\eta\} &= 0.
\end{aligned} \tag{2.96}$$

Additionally, the span-wise variables are scaled to reflect the weak longshore dependence of the waves:

$$y \leftarrow \alpha^{1/2}y \qquad \hat{y}\cdot\mathbf{u} \leftarrow \alpha^{-1/2}\hat{y}\cdot\mathbf{u}. \tag{2.97}$$

2.3.4 Slightly Resonant Interacting Triads

Once the equations are non-dimensionalized, the procedure used to arrive at the lowest-order theory is the same as was done for the surface case. In this presentation the reflected wave shall be eliminated from the outset.

The uniform expansion, after cross differentiating Equation (2.94), is

$$\begin{aligned}
\alpha^0 : \quad &\mathcal{L}\eta_0 = 0 \\
\alpha^1 : \quad &\mathcal{L}\eta_1 = \mathcal{G}_1(\eta_0, u_0, v_0, G; x, X, y, t) \\
\alpha^2 : \quad &\mathcal{L}\eta_2 = \mathcal{G}_2(\eta_0, u_0, v_0, \eta_1, u_1, v_1, G; x, X, y, t)
\end{aligned} \tag{2.98}$$

where

$$\mathcal{L} = \partial_{tt} - \gamma\partial_{xx} - d\frac{\beta^2\rho_2\partial_{xxtt}}{3\rho_1}, \tag{2.99}$$

The inhomogeneous terms $\mathcal{G}_1$ and $\mathcal{G}_2$ involve terms that appear in the left hand side of

equations of order lower than where they show up. Consider the lowest order, in which

$$
\begin{aligned}
\mathcal{G}_1 &= (\gamma + d\frac{\beta^2 \rho_2 \partial_{tt}}{3\rho_1})\eta_{0yy} + G(\gamma + d\frac{2\beta^2 \rho_2 \partial_{tt}}{3\rho_1})\eta_{0xx} + 2(\gamma + d\frac{\beta^2 \rho_2 \partial_{tt}}{3\rho_1})\eta_{0x}X \\
&+ (u_0^2/2)_x - (u_0\eta_0)_{xt}.
\end{aligned}
\tag{2.100}
$$

The lowest order modal expansion for the surface velocity shall be assumed to be

$$
u_0(x, X, y, t) = \sum_{j=1}^{2} a_j(X, y)e^{i(k_j x - \omega_j t)} + c.c..,
\tag{2.101}
$$

The lowest order relation $u_{0t} + \gamma\nabla\eta_0 = 0$, is used to obtain the surface amplitude

$$
\eta_0(x, X, y, t) = \sum_{j=1}^{2} \frac{\omega_j}{\gamma k_j}a_j(X, y)e^{i(k_j x - \omega_j t)} + c.c..
\tag{2.102}
$$

Substituting Equations (2.101) and (2.102) into Equation (2.98) and applying the compatibility condition, yields the equations for spatial variation of the first two modal amplitudes

$$
\begin{aligned}
a_{1x} + i\varepsilon f D_1 E_1 a_1 - i\alpha F_1 a_{1yy} + i\alpha D_1 S_1 e^{-i\delta x} a_1^* a_2 &= 0 \\
a_{2x} + i\varepsilon f D_2 E_2 a_2 - i\alpha F_2 a_{2yy} + i\alpha D_2 S_2 e^{+i\delta x} a_1^2 &= 0,
\end{aligned}
\tag{2.103}
$$

to $O(\delta/X)$. The constants are

$$
\begin{aligned}
D_j &= 1/2(1 - d\frac{\rho_2\beta^2\omega_j^2}{3\rho_1}) \\
E_j &= k_j(\gamma - d\frac{2\rho_2\beta^2\omega_j^2}{3\rho_1}) \\
F_j &= 1/2k_j \\
S_1 &= \frac{k_2 - k_1}{\omega_1}\{k_2 - k_1 + \frac{\omega_1}{\gamma}(\frac{\omega_1}{k_1} + \frac{\omega_2}{k_2})\} \\
S_2 &= \frac{2}{\omega_2}k_1^2 + 2\omega_1^2.
\end{aligned}
\tag{2.104}
$$

The dispersion relation for the internal waves is

$$
\omega_j^2 - \frac{k_j^2}{\gamma + d\beta^2\frac{\rho_2 k_j^2}{3\rho_1}} = 0.
\tag{2.105}
$$

Chapter 3

The Mass Transport Problem

The drift velocity is the second-order steady state flow that is created by the passage of overlying water waves in the sediment-laden boundary layer that hugs the bottom topography. The boundary layer is assumed to have a characteristic thickness $\delta_{bl} \ll h_0$. The sediment in the boundary layer shall be assumed to move from place to place at a rate equal to the drift velocity. This chapter shall present the lowest order theory, leaving the details of the higher order theory to Appendix A.

In order to subsequently compute the drift velocity, it shall be required to find the fluid velocity immediately outside of the sediment-laden boundary layer. From Equation (2.29) in scaled variables, the shoreward velocity is explicitly

$$
\begin{aligned}
U_b &\equiv \hat{x}\cdot\mathbf{U}(\mathbf{r}, -h, t) \\
&= u(\mathbf{r}, t) - \beta^2\{-h[(hu_{xx}(\mathbf{r}, t)) + \alpha(hv_{xy}(\mathbf{r}, t))] + \tfrac{1}{2}h^2(u_{xx}(\mathbf{r}, t) + \alpha v_{xy}(\mathbf{r}, t))\},
\end{aligned}
\tag{3.1}
$$

and the span-wise velocity

$$
\begin{aligned}
V_b &\equiv \hat{y}\cdot\mathbf{U}(\mathbf{r}, -h, t) \\
&= v(\mathbf{r}, t) - \beta^2\{-h[(hu_{xy}(\mathbf{r}, t)) + \alpha(hv_{yy}(\mathbf{r}, t))] + \tfrac{1}{2}h^2(u_{xy}(\mathbf{r}, t) + \alpha v_{yy}(\mathbf{r}, t))\}
\end{aligned}
\tag{3.2}
$$

in the neighborhood of the boundary layer. Neglecting the reflected component, the

bottom velocities to lowest order are

$$
\begin{aligned}
U_{0b} &= u_0 + \beta^2 \tfrac{h^2}{2} u_{0xx} \\
&= \textstyle\sum_{j=1}^{2} C_j a_j(X,y) e^{i(k_j x - \omega_j t)} + c.c. \\
V_{0b} &= v_0 + \beta^2 \tfrac{(h^2)_y}{2} u_{0x} + \beta^2 \tfrac{h^2}{2} u_{0xy} \\
&= -i \textstyle\sum_{j=1}^{2} \tfrac{1}{k_j}[C_j a_{jy}(X,y) + i\beta^2 \tfrac{k_j}{2}(h^2)_y] e^{i(k_j x - \omega_j t)} + c.c.
\end{aligned}
\tag{3.3}
$$

where $C_j = 1 - \beta^2 k_j^2 \tfrac{h^2}{2}$.

3.1 Hydrodynamics of the Boundary Layer

In the boundary layer the transverse momentum, vertical momentum, and the continuity equations are respectively

$$
\begin{aligned}
\mathbf{u}_t + \mathbf{u}\cdot\nabla\mathbf{u} + w\mathbf{u}_z &= -\tfrac{1}{\rho}\nabla p + \nu\Delta\mathbf{u} + \nu\mathbf{u}_{zz} \\
\bar{w}_t + \mathbf{u}\cdot\nabla\bar{w} + \bar{w}\bar{w}_z &= -\tfrac{1}{\rho}p_z + g + \nu\Delta\bar{w} + \nu\bar{w}_{zz} \\
\nabla\cdot\mathbf{u} + \bar{w}_z &= 0
\end{aligned}
\tag{3.4}
$$

where ν is the eddy viscosity. Across the boundary layer the flow velocity changes from zero at the bottom boundary to some finite value characteristic of the exterior inviscid fluid. The derivatives with respect to z of any flow quantity are thus, in general, much greater than those with respect to x or y. Hence, within the boundary layer, $|\nabla\mathbf{u}| \ll |u_z|$, $|\nabla^2\mathbf{u}| \ll |u_{zz}|$, etc. In view of this, it may be concluded that the transverse momentum in Equation (3.4) is well approximated by

$$
\mathbf{u}_t + \mathbf{u}\cdot\nabla\mathbf{u} + w\mathbf{u}_z = -\frac{1}{\rho}\nabla p + \nu\mathbf{u}_{zz}.
\tag{3.5}
$$

The velocity $\bar{w}$ must also be small. The continuity statement in Equation (3.4) suggests that the boundary layer and $\bar{w}$ are of equal order of smallness. Therefore, none of the terms on the left hand side of Equation (3.5) can be neglected. On the other side of the equation, it is expected that $\nu\mathbf{u}_{zz}$ be of comparable size to the inertial terms. The

magnitude of the inertial terms is represented by the size of $\mathbf{u} \cdot \nabla \mathbf{u}$, hence the balance is such that $O(\mathbf{u} \cdot \nabla \mathbf{u} / \nu \mathbf{u}_{zz}) = 1$ when the Reynolds number is sufficiently large, i.e. so it is mostly true in the whole boundary layer. If $\sqrt{gh_0}$ is representative of the magnitude of the velocity $\mathbf{u}$ and λ represents a distance in the transverse direction over which $\mathbf{u}$ changes appretiably, then $(\sqrt{gh_0})^2 / \lambda = O(\mathbf{u} \cdot \nabla \mathbf{u})$. Since δ_{bl} is the boundary layer thickness, $\nu \sqrt{gh_0} / \delta_{bl}^2$ is a measure of $\nu \mathbf{u}_{zz}$. Thus,

$$O(\delta_{bl}^2 R / \lambda^2) = 1, \text{ where } R = \frac{\sqrt{gh_0}\lambda}{\nu}. \tag{3.6}$$

The dimensionless constant R is the Reynolds number. Equation (3.6) implies that $\delta_{bl} \sim \lambda R^{-1/2}$ as $R \rightarrow \infty$, which suggests that the boundary layer concept improves as $R \rightarrow \infty$, and that $\delta_{bl} \propto \lambda^{1/2} \nu^{1/2}$. In this study λ is large but of finite length. It is assumed that the boundary layer does not change significantly as a function of wave frequency, enabling the replacement of λ by h_0 in R, so that $R = \sqrt{gh_0}h_0/\nu$, arriving, then, at a working definition for the boundary layer thickness

$$\delta_{bl} = \sqrt{\nu / h_0 (gh_0)^{1/2}}, \tag{3.7}$$

which shall be non-dimensionalized by dividing by h_0. In this scaling, it is implied that the size of the Reynolds number and the boundary layer thickness are controlled mostly by the viscous effects, i.e. the size of ν.

To get an estimate of the size of $\bar{w}$, the continuity condition in Equation (3.4) suggests that

$$O(\bar{w}_z / \nabla \mathbf{u}) = \delta_{bl} h_0 / \lambda = \beta \sqrt{gh_0} R^{-1/2} \tag{3.8}$$

thus

$$\bar{w} = O(\beta \sqrt{gh_0} R^{-1/2}). \tag{3.9}$$

With Equation (3.9) in hand, it can be inferred from the vertical momentum balance

that

$$g + \frac{p_z}{\rho} = O(\delta_{bl}),$$ (3.10)

hence $p_z = O(\delta_{bl})$, i.e. the pressure is approximately constant throughout the layer.

We are now in the position of estimating the balance of terms in Equation (3.4). We approach this in stages. Firstly, to make the system in the boundary layer consistent with those in the inviscid fluid, we adopt the inviscid scaling. The equations are now

$$\beta \mathbf{u}_t + \alpha\beta \mathbf{u}\cdot\nabla\mathbf{u} + \alpha\bar{w}\mathbf{u}_z = -\frac{\beta}{\alpha}\nabla p + \frac{\nu}{\sqrt{gh_0 h_0}}[\beta^2 \Delta\mathbf{u} + \nu\mathbf{u}_{zz}]$$

$$\beta\bar{w}_t + \alpha\beta\mathbf{u}\cdot\nabla\bar{w} + \alpha\bar{w}\bar{w}_z = -\frac{1}{\alpha}p_z + 1/\alpha + \frac{\nu}{\sqrt{gh_0 h_0}}[\beta^2 \Delta\bar{w} + \nu\bar{w}_{zz}]$$ (3.11)

$$\beta\nabla\cdot\mathbf{u} + \bar{w}_z = 0.$$

Next, we invoke the boundary layer scaling, and at the same time invoke the weak y dependence scaling. Let

$$\bar{z} = R^{1/2}z$$
$$w = R^{1/2}\bar{w}$$ (3.12)

and consider the boundary layer equations when the Reynolds number is large. The system is

$$\beta u_t + \alpha\beta[uu_x + \alpha vu_y] + \alpha wu_{\bar{z}} = -\frac{\beta}{\alpha}p_x + u_{\bar{z}\bar{z}}$$

$$\beta v_t + \alpha\beta[uv_x + \alpha vv_y] + \alpha wv_{\bar{z}} = -\frac{\beta}{\alpha}p_y + v_{\bar{z}\bar{z}}$$

$$p_{\bar{z}} = O(\delta_{bl})$$ (3.13)

$$\beta(u_x + \alpha v_y) + w_{\bar{z}} = 0.$$

Finally, we translate and stretch the vertical coordinate $\delta_{bl}n = z + h$, so that

$$\beta u_t + \alpha\beta[uu_x + \alpha vu_y] + \alpha wu_n = -\frac{\beta}{\alpha}p_x + u_{nn}$$

$$\beta v_t + \alpha\beta[uv_x + \alpha vv_y] + \alpha wv_n = -\frac{\beta}{\alpha}p_y + v_{nn}$$

$$p_n = O(\delta_{bl})$$ (3.14)

$$\beta(u_x + \alpha v_y) + w_n = 0.$$

A locally flat bed has been assumed. In contrast, suppose that the bed had some finite curvature K, say. This would change the vertical momentum balance in Equation (3.14) to

$$p_n = K O(\mathbf{u}^2).$$ (3.15)

but the pressure change across the layer is still of $O(\delta_{bl})$, so we are justified in the assumption that the bed be locally flat.

The following boundary data is used to solve Equation (3.14):

$$u = v = w = 0 \qquad \text{at } n = 0$$ (3.16)

and

$$u \to U_b$$
$$v \to V_b, \qquad n \to \infty.$$ (3.17)

The velocity (U_b, V_b) immediately outside of the layer gives rise to the following pressure gradients:

$$\begin{aligned} -\frac{\beta}{\alpha} p_x &= \beta U_{bt} + \alpha\beta(U_b U_{bx} + \alpha V_b U_{by}) \\ \frac{\beta}{\alpha} p_y &= \beta V_{bt} + \alpha\beta(U_b V_{bx} + \alpha V_b V_{by}). \end{aligned}$$ (3.18)

We have, thus, all the required information to solve for the velocities in the boundary layer. Performing the usual expansion

$$\begin{aligned} u &= \tilde{u}_0 + \alpha \tilde{u}_1 \cdots \\ v &= \tilde{v}_0 + \alpha \tilde{v}_1 \cdots \end{aligned}$$ (3.19)

the lowest order equations are

$$\beta\tilde{u}_{0t} - \tilde{u}_{0nn} = \beta U_{0bt}$$

$$\beta\tilde{v}_{0t} - \tilde{v}_{0nn} = \beta V_{0bt}$$

$$p_{0n} = 0 \tag{3.20}$$

$$\beta\tilde{u}_{0x} + \tilde{w}_{0n} = 0.$$

The following order is given by

$$\beta\tilde{u}_{1t} - \tilde{u}_{1nn} = -\beta\tilde{u}_0\tilde{u}_{0x} - \tilde{w}_0\tilde{u}_{0n} + \beta U_{0b}U_{0x} + U_{1t}$$

$$\beta\tilde{v}_{1t} - \tilde{v}_{1nn} = -\beta\tilde{u}_0\tilde{v}_{0x} - \tilde{w}_0\tilde{v}_{0n} + \beta U_{0b}V_{0x} + \beta V_{1bt} \tag{3.21}$$

$$\beta\tilde{u}_{1x} + \tilde{w}_{1n} = -\beta\tilde{v}_{0y},$$

and shall be addressed in Appendix A. Note that terms such as U_{1t}, etc., have been dropped. The goal is to compute the drift velocity and these terms do not contribute to the steady part of the drift velocity since the external flow is time harmonic.

A solution of Equation (3.20) of the form

$$\tilde{u}_l = \sum_{j=1}^{2} \alpha^l P_l(x,y,n)e^{i(k_j x - \omega_j t)} + c.c. \tag{3.22}$$

subject to the boundary conditions given by Equations(3.16) and (3.17), is found by integrating Equation (3.20). The same procedure is used to obtain $\tilde{v}$. The result is

$$\tilde{u}_0 = \sum_{j=1}^{2} C_j a_j (1 - e^{-n\Lambda_j})e^{i(k_j x - \omega_j t)} + c.c.$$

$$\tilde{v}_0 = i\sum_{j=1}^{2} k_j(\beta^2(h^2)_y a_j/2 - C_j a_{jy}/k_j^2)(1 - e^{-n\Lambda_j})e^{i(k_j x - \omega_j t)} + c.c. \tag{3.23}$$

$$\tilde{w}_0 = i\beta\sum_{j=1}^{2} k_j C_j a_j (1 - n\Lambda_j - e^{-n\Lambda_j})/\Lambda_j e^{i(k_j x - \omega_j t)} + c.c.$$

where $\Lambda_j = (1 - i)\sqrt{\beta\omega_j/2}$. The vertical velocity $\tilde{w}$ was found by integrating the continuity equation.

3.2 The Drift Velocity

In this section we follow closely Longuett-Higgins' study on mass transport by oscillatory flows [25]. Define the time average of the quantity A as

$$\langle A \rangle \equiv \frac{\omega}{2\pi} \int_t^{t+\frac{2\pi}{\omega}} A(s)ds = \frac{1}{\tau} \int_t^{t+\tau} A(s)ds. \tag{3.24}$$

The drift velocity shall be the time average displacement rate of a fluid particle. As Stokes noted [26], the drift velocity is second order in nature. That is, if $\tilde{u}(\mathbf{r}, z, t)$ is the Eulerian velocity, and the motion is periodic,

$$\tilde{u}(\mathbf{r}, z, t + \tau) = \tilde{u}(\mathbf{r}, z, t), \tag{3.25}$$

and expressible as the asymptotic series

$$\tilde{u} = \tilde{u}_0 + \alpha^1 \tilde{u}_1 + \alpha^2 \tilde{u}_2 + \cdots \tag{3.26}$$

then $\langle \tilde{u}_0 \rangle = 0$ is a statement of this assumption, i.e. the lowest order steady state current is zero. Let $\mathbf{U}(\mathbf{r}_0, z_0, t_0)$ denote the Lagrangian velocity, or velocity of a fluid particle at $t = t_0$ with position $(\mathbf{r}_0, z_0)$. Then, the displacement of the particle from its original position to some other position

$$(\mathbf{r}, z) = (\mathbf{r}_0, z_0) + \int_{t_0}^t \mathbf{U}(\mathbf{r}_0, z_0, \tilde{t})d\tilde{t} \tag{3.27}$$

at time t. It follows that

$$\mathbf{U}(\mathbf{r}, z, t) = \tilde{u}[(\mathbf{r}_0, z_0) + \int_{t_0}^t \mathbf{U}(\mathbf{r}_0, z_0, \tilde{t})d\tilde{t}, t] \tag{3.28}$$

which can be formally expanded in a Taylor series

$$\begin{aligned}
\mathbf{U}(\mathbf{r}, z, t) = \quad & \tilde{u}(\mathbf{r}_0, z_0, t) + \int_{t_0}^t \mathbf{U}d\tilde{t} \cdot \nabla_{(\mathbf{r}_0, z_0)} \tilde{u}(\mathbf{r}_0, z_0, t) \\
& + \frac{1}{2} \{ \int_{t_0}^t \mathbf{U}d\tilde{t} \}^T \cdot H_{(\mathbf{r}_0, z_0)} \tilde{u}(\mathbf{r}_0, z_0, t) \cdot \int_{t_0}^t \mathbf{U}d\tilde{t} + \cdots.
\end{aligned} \tag{3.29}$$

Here H stands for the Hessian, and both the Hessian and gradients have subscripts to remind us as to where they are to be evaluated. The steady state Lagrangian velocity is in fact akin to the drift velocity. An approximate expression for it, in terms of the Eulerian velocity in the boundary layer, can be obtained by expanding

$$\mathbf{U} = \mathbf{U}_0 + \alpha^1 \mathbf{U}_1 + \alpha^2 \mathbf{U}_2 + \cdots \tag{3.30}$$

and substituting Equations (3.30) and (3.26) into Equation (3.29), order by order. After time-averaging we obtain

$$
\begin{aligned}
O(\alpha^0): \quad &\langle \mathbf{U}_0 \rangle = \langle \mathbf{u}_0 \rangle = 0 \\
O(\alpha^1): \quad &\langle \mathbf{U}_1 \rangle = \langle \mathbf{u}_1 \rangle + \langle \textstyle\int^t \mathbf{u}_0 d\tilde{t}\cdot\nabla \mathbf{u}_0 \rangle \\
O(\alpha^2): \quad &\langle \mathbf{U}_2 \rangle = \langle \mathbf{u}_2 \rangle + \langle \textstyle\int^t \mathbf{U}_1 d\tilde{t}\cdot\nabla \mathbf{u}_0 \rangle + \langle \textstyle\int^t \mathbf{U}_0 d\tilde{t}\cdot\nabla \mathbf{u}_1 \rangle + \\
&\quad \tfrac{1}{2}\langle \{\textstyle\int^t \mathbf{u}_0 d\tilde{t}\}^T \cdot H \mathbf{u}_0 \cdot \int_{t_0}^t \mathbf{u}_0 d\tilde{t} \rangle.
\end{aligned}
\tag{3.31}
$$

The drift velocity is then

$$(\mathcal{U}, \mathcal{V}) = \alpha^1 \mathbf{U}_1 + \alpha^2 \mathbf{U}_2 + \cdots \tag{3.32}$$

We shall compute the drift velocity to lowest order in this chapter, and leave consideration of the higher order contribution, which can be rewritten as

$$
\begin{aligned}
\langle \mathbf{U}_2 \rangle = \; &\langle \mathbf{u}_2 \rangle + \langle \textstyle\int^t \mathbf{u}_1 d\tilde{t}\cdot\nabla \mathbf{u}_0 \rangle + \langle \textstyle\int^t \int^{t'} \mathbf{u}_0 dt'\cdot\nabla \mathbf{u}_0 d\tilde{t}\cdot\nabla \mathbf{u}_0 \rangle + \langle \textstyle\int^t \mathbf{u}_0 d\tilde{t}\cdot\nabla \mathbf{u}_1 \rangle + \\
&\tfrac{1}{2}\langle \{\textstyle\int^t \mathbf{u}_0 d\tilde{t}\}^T \cdot H \mathbf{u}_0 \cdot \int_{t_0}^t \mathbf{u}_0 d\tilde{t} \rangle,
\end{aligned}
\tag{3.33}
$$

to Appendix A. Expressing the $O(\alpha)$ in component form, after weak y dependence scaling has been adopted, the drift velocity is

$$
\begin{aligned}
\mathcal{U} &= \langle u_1 \rangle + \langle \textstyle\int^t u_0 d\tilde{t}\, u_{0x} \rangle + \langle \textstyle\int^t w_0 d\tilde{t}\, u_{0n} \rangle \\
\mathcal{V} &= \langle v_1 \rangle + \langle \textstyle\int^t u_0 d\tilde{t}\, v_{0x} \rangle + \langle \textstyle\int^t w_0 d\tilde{t}\, v_{0n} \rangle.
\end{aligned}
\tag{3.34}
$$

3.3 The Mass Transport Equation

3.3.1 Remarks

In regions where sand ridges are found the mean slope of the bottom is very slight. Hence, downslope gravitational transport, important in the shoaling region, plays an undiscernible role in shaping sand ridges in the deeper end of the shelf. The type of sediment transport we have in mind is primarily suspended load. The sediment drifts as a result of the unclosed orbital paths, resulting from the asymmetry in the nonlinear wave motion. In what follows the fluid wave field shall be assumed to be entirely represented by the incident wave. Further, it is assumed that the viscous boundary layer is sediment-laden, composed of cohesionless, rarely interacting, sand particles.

The sediment concentration ρ, in coastal environments has a very weak influence on the fluid flow [59]. Typical values for the concentration are $\rho \sim 10^{-3} - 10^{-4} ppm$, and it shall be assumed that this is the situation thoughout the shelf. Chapalain [59] and Bokzar-Karakiewikz et al. [60] concluded that time independent and vertically uniform parameters of eddy viscosity and eddy diffusivity are adequate in providing satisfactory accuracy for sediment morphology models on the shelf. In this study we shall adopt a very simple model, found in [3], for the sediment concentration.

The equation of continuity for the sediment concentration is the advection-diffusion equation

$$\rho_t + \nabla\cdot(\mathbf{u}\rho) + [(w - v_f)\rho]_n = 0, \qquad (3.35)$$

where v_f is the sediment "fall velocity" and $n = (z + h(X, y, T))/\delta_{bl}$. Assume that, appart from random fluctuations, $\mathbf{u}$ and ρ do not vary much over small transverse spatial scales so that the second term of the above equation may be neglected. In light of this, the

sediment concentration changes at a rate $\partial \rho / \partial n$ proportional to the vertical flux. Hence,

$$w\rho = -\gamma \rho_n \tag{3.36}$$

where γ is the diffusivity constant.

The flux, which is the product of the concentration and the velocity, can be split into a time dependent part C^t and a time independent part C^m. Boczar-Karakiewicz et al. [9] found that in the sand ridge areas, the ratio $C^t / C^m = O(10^{-2})$ for the off-shore case. This situation shall be assumed to apply throughout the shelf, so that the sediment concentration shall be represented solely by the time independent part in this study. Employing this assumption and substituting Equation (3.36) into Equation (3.35), the equation for sediment concentration is now

$$\gamma \rho_n + v_f \rho = 0. \tag{3.37}$$

The boundary condition may be taken as

$$\frac{\gamma}{v_f} \frac{\partial \rho}{\partial n} = P(\mathbf{r}), \tag{3.38}$$

where $P(\mathbf{r})$ is akin to Svendsen's [61] "pick-up function", which incorporates such effects as the degree of wave asymmetry and skewness of sediment flux, and a Shield's parameter, which sets a threshold fluid velocity at which sediment will be picked up, based upon the sediment particles' buoyancy and geometry, and the fluid's velocity field and viscocity. The pick-up function $P(\mathbf{r})$ is obvoiusly an empirically-derived function.

Solving Equation (3.37), the sediment concentration takes the form

$$\rho = P(\mathbf{r})e^{-\sigma n}, \tag{3.39}$$

where $\sigma = v_f / \gamma$. The fall velocity v_f is species-dependent. It is either measured or estimated by calculating the balance of drag to buoyant forces for a particle falling

freely into a static fluid. The diffusivity constant γ is hard to estimate. Sedimentologists usually measure its value in the field. The pick-up function $P(\mathbf{r})$ is an empirically-derived function.

3.3.2 The Transport Equation

For the sake of clarity, the mass transport equation shall be derived assuming transverse dependence in the x direction only. The generalization to variations in y will follow in a straight-forward manner.

Let $T \in [0, \infty)$ and $\Omega_T \in \mathcal{R}^1 \times [h(T), \zeta]$, where $\zeta \geq h(T) + \delta_{bl}$, be the boundary layer time-space domain, and consider a differential "volume" element in such a domain, as shown in Figure 3.1, which on the bottom is bounded by the ocean topography, and on the top by a flat lid $z' = \zeta$. By examining the balance of mass in this differential volume a transport equation can be developed.

It is assumed that the sediment concentration ρ is entirely negligible for $z' > \zeta$, and moves on fast-time scales. In what follows $\rho : \Omega_T \longmapsto \mathcal{R}^1$. The sediment concentration and drift velocity are thought to be $C^1(\Omega_T)$, and the bottom topography $h \in C^1(T)$, and piece-wise linear in Ω_T.

The mass flux per unit length at x in a time interval $[T, T + \Delta T]$ is given by

$$\int_T^{T+\Delta T} d\tau \int_{h(x,\tau)}^{\zeta} dz' \rho(x, z') \mathcal{U}(x, z') \equiv \int_T^{T+\Delta T} d\tau \int_{h(x,\tau)}^{\zeta} dz' M(x, z'). \qquad (3.40)$$

Consider a portion of the region, say $[x, x + \Delta x]$ in a time interval $[T, T + \Delta T]$. Since mass cannot spontaneously vanish or be created, the net amount of sediment between point x and $x + \Delta x$ must be compensated by a change in the concentration of the sediment, or by a topographical change in the bottom surface. The flux difference in the space and
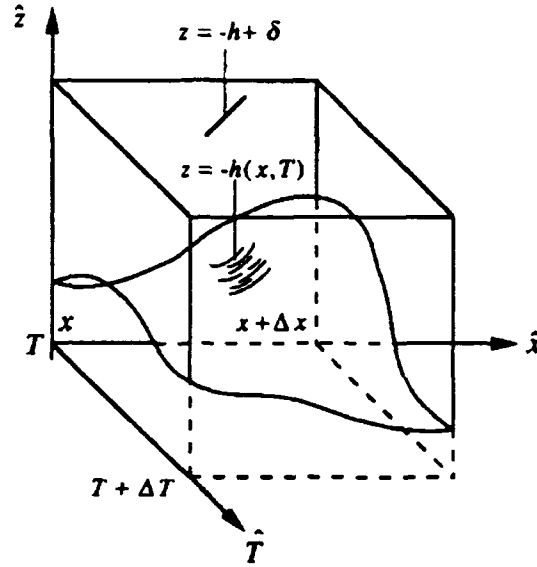
Figure 3.1: Volume element used in the derivation of the mass trasport equation.

time intervals $[x, x + \Delta x]$, $[T, T + \Delta T]$, is thus

$$\int_T^{T+\Delta T} d\tau \int_{h(x+\Delta x,\tau)}^{\zeta} dz' M(x + \Delta x, z') - \int_T^{T+\Delta T} d\tau \int_{h(x,\tau)}^{\zeta} dz' M(x, z'), \quad (3.41)$$

and the total mass in the given portion at time T is gven by

$$\int_x^{x+\Delta x} d\xi \int_{h(\xi,T)}^{\zeta} dz' \rho(\xi, z'). \quad (3.42)$$

The change in total mass in a time interval $[T, T + \Delta T]$ due to net accumulation is given

by

$$\int_x^{x+\Delta x} d\xi \int_{h(\xi,T+\Delta T)}^{\zeta} dz \rho(\xi, z') - \int_x^{x+\Delta x} d\xi \int_{h(\xi,T)}^{\zeta} dz' \rho(\xi, z'), \quad (3.43)$$

or equivalently,

$$\int_x^{x+\Delta x} d\xi \int_{h(\xi,T)}^{h(\xi,T+\Delta T)} dz' \rho(\xi, z'). \quad (3.44)$$

Equating (3.41) and (3.44), dividing by $\Delta x \Delta T$ and formally taking the limit as Δx, and

ΔT go to zero, we have, on the right hand side.

$$\lim_{\Delta T \to 0 \Delta x \to 0} \frac{1}{\Delta x \Delta T} \int_x^{x+\Delta x} d\xi \int_{h(\xi,T)}^{h(\xi,T+\Delta T)} dz' \rho(\xi, z') \sim$$

$$\lim_{\Delta T \to 0 \Delta x \to 0} \frac{1}{\Delta x \Delta T} \int_x^{x+\Delta x} d\xi \int_{h(\xi,T)}^{h(\xi,T)+\Delta T \frac{\partial h(\xi,T)}{\partial T}} dz' \rho(\xi, z') = \qquad (3.45)$$

$$\rho(x, h(x,T)) \frac{\partial h(x,T)}{\partial T}.$$

and on the other side of the equation.

$$\lim_{\Delta T \to 0 \Delta x \to 0} \frac{1}{\Delta x \Delta T} \int_T^{T+\Delta T} d\tau \{ \int_{h(x+\Delta x,\tau)}^{\zeta} dz' M(x+\Delta x, z') - \int_{h(x,\tau)}^{\zeta} dz' M(x,z') \} =$$

$$\lim_{\Delta T \to 0 \Delta x \to 0} \frac{1}{\Delta x \Delta T} \int_T^{T+\Delta T} \{ \int_{h(x+\Delta x,\tau)}^{\zeta} dz' [M(x,z') + \Delta x \frac{\partial M}{\partial x}(x,z') + \cdots] -$$

$$\int_{h(x,\tau)}^{\zeta} M(x,z') \} = \lim_{\Delta T \to 0 \Delta x \to 0} \frac{1}{\Delta x \Delta T} \Delta x \int_{h(x,\tau)+\Delta x \frac{\partial h}{\partial x}}^{\zeta} dz' \frac{\partial M}{\partial x}(x,z') =$$

$$\int_{h(x,T)}^{\zeta} dz' \frac{\partial M}{\partial x}(x,z')$$

$$(3.46)$$

Therefore, the mass transport equation is

$$\frac{\partial h(x,T)}{\partial T} = \frac{K'}{\rho(x, h(x,T))} \frac{\partial}{\partial x} \int_{h(x,T)}^{\zeta} \rho(x,z') \mathcal{U}(x,z') dz' \qquad (3.47)$$

where K' is a constant of proportionality. Since the boundary layer is assumed very thin.

we may define the mass transport flux as

$$\mu \equiv \int_0^{\delta_{bl}} \rho(x,z') \mathcal{U}(x,z')) dz'$$

$$\nu \equiv \int_0^{\delta_{bl}} \rho(x,z') \mathcal{V}(x,z')) dz' \qquad (3.48)$$

so that the transport equation now reads

$$\frac{\partial h(x,T)}{\partial T} = \frac{K}{\rho_0} \mu_x. \qquad (3.49)$$

The generalization of Equation (3.49) to one more space dimension is

$$\frac{\partial h(x,y,T)}{\partial T} = \frac{K}{\rho_0} (\mu_x + \nu_y), \qquad (3.50)$$

where μ and ν are the shoreward mass flux and the longshore mass flux, respectively. Note that when weak y dependence scaling is adopted in Equation (3.50), the longshore mass flux shall be $O(\alpha)$ smaller than all other quantities in the equation.

In the remainder of this study, it shall be assumed, for simplicity, that the sediment concentration is constant and equal to ρ_0 in the boundary layer. In terms of Equation (3.34), and upon use of Equation (3.48), the calculation of the mass flux components, to lowest order, are

$$\mu = \sum_{j=1}^{2} \frac{2k_j C_j^2 |a_j|^2}{\omega_j \sigma_j} \mathcal{I}_{1j} + \sum_{j=1}^{2} \frac{\beta k_j C_j^2 |a_j|^2}{\sigma_j^3} \mathcal{I}_{2j} + c.c. \tag{3.51}$$

where

$$
\begin{aligned}
\mathcal{I}_{1j} =\ & \sigma_j \delta_{bl} - \frac{\beta \sigma_j}{2} - \frac{3}{2} + \frac{1}{2}(1 - \beta \sigma_j)e^{-2\sigma_j \delta_{bl}} \\
& + e^{-\sigma_j \delta_{bl}}[\cos \sigma_j \delta_{bl} - \sin \sigma_j \delta_{bl}][1 - \beta \sigma_j(\sigma_j \delta_{bl} + 1)]
\end{aligned}
\tag{3.52}
$$

and

$$
\begin{aligned}
\mathcal{I}_{2j} =\ & \frac{3}{2}(1/2 - \sigma_j \delta_{bl}) + e^{-2\sigma_j \delta_{bl}}/4 \\
& - e^{-\sigma_j \delta_{bl}}[1 + \delta_{bl}\sigma_j]\cos \sigma_j \delta_{bl} + 2e^{-\sigma_j \delta_{bl}}\sin \sigma_j
\end{aligned}
\tag{3.53}
$$

for the shoreward mass flux, and

$$\nu = \sum_{j=1}^{2} \frac{iC_j^2 a_j^\star a_{jy}}{\omega_j \sigma_j} \mathcal{J}_j + O(\beta^3) + c.c. \tag{3.54}$$

for the longshore directed mass flux, with

$$
\begin{aligned}
\mathcal{J}_j =\ & \sigma_j \delta_{bl} - 1 - \frac{1}{2}(1 - e^{-2\sigma_j \delta_{bl}}) + e^{-\sigma_j \delta_{bl}}(\cos \sigma_j \delta_{bl} - \sin \sigma_j \delta_{bl}) \\
& + \beta \Lambda_j [\frac{1}{2}(1 + e^{-2\sigma_j \delta_{bl}}) + e^{-\Lambda_j \delta_{bl}}(i\delta_{bl}\sigma_j/2 - 1)].
\end{aligned}
\tag{3.55}
$$

The quantities $\mathcal{I}_{11}$, $\mathcal{I}_{21}$ and $\mathcal{J}_1$ are plotted parametrically in Figures 3.2, 3.3, and 3.4.
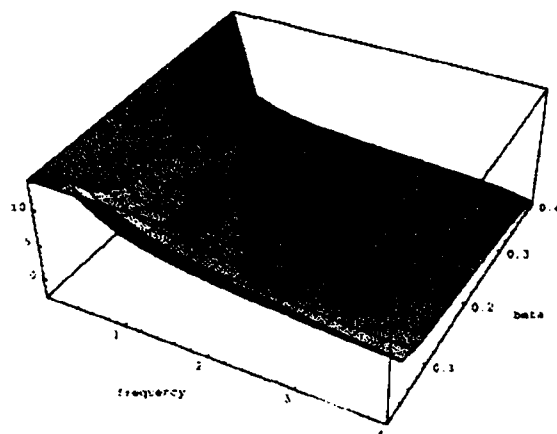
Figure 3.2: Variation of $\mathcal{I}_{11}$, with $\delta_{bl} = 1.0$ fixed.

Before proceeding, two important remarks are in order. Firstly, it is noted that the bottom needn't be slightly perturbed to initiate the development of bars. Even a flat bottom will eventually develop bars given that all the conditions are right. Secondly, we are now in the position to justify the two-time scale solution of the surface/bottom system. The ratio of the magnitude of the time rate of change of the bottom to the Eulerian velocity leads in a straight-forward manner to the conclusion that $t/T = O(\alpha)O(\delta_{bl})O(\rho) \sim O(10^{-7})$, assuming that the boundary layer thickness is typically $O(10^{-2}h_0)$ and the sediment concentration is $O(10^{-4})$ ppm.
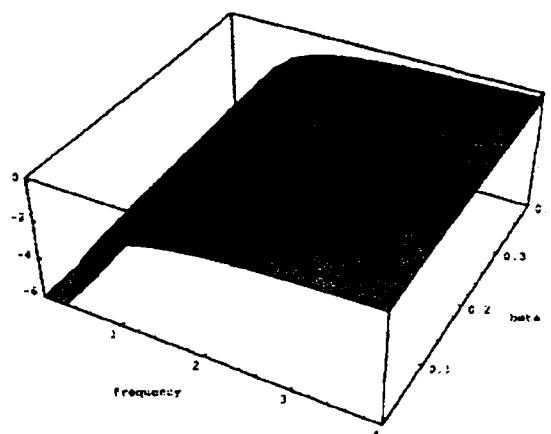
Figure 3.3: Variation of $\mathcal{I}_{21}$, with $\delta_{bl} = 1.0$ fixed.
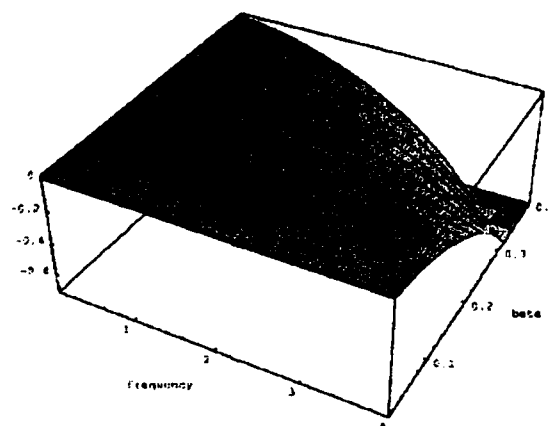
Figure 3.4: Parametric Plot of $\mathcal{J}_1$, with $\delta_{bl} = 1.0$ fixed.

Chapter 4

The Complete Model: Mathematical Analysis

After summarizing the model, this chapter shall be devoted to the details of formal and analytical results, primarily relevant to discerning the behavior and structure of the surface system. Our concentration on the surface system is motivated by the fact that much is known already about the type of equation represented by the mass transport equation, whereas the surface system, insofar as we can tell, is a new mathematical equation. Many of the surface system results presented here are actually not applicable to the oceanic setting in which this equation was derived; additionally, some the results are not entirely new. However, since the surface system is interesting in its own right, and it could serve as a model for other physical processes, the results are still of value.

For the surface, after replacing the multiple scale expansion $X = \alpha x$,

$$a_{1x} - iK_1 a_{1yy} + iK_3 f(x,y)a_1 + iK_5 e^{-i\delta x}a_1^* a_2 = 0$$

$$a_{2x} - iK_2 a_{2yy} + iK_4 f(x,y)a_2 + iK_6 e^{+i\delta x}a_1^2 = 0$$

$$b_{1x} + iL_1 b_{1yy} - iL_3 f(x,y)b_1 - iL_5 e^{+i\delta x}b_1^* b_2 = 0$$

$$b_{2x} + iL_2 b_{2yy} - iL_4 f(x,y)b_2 - iL_6 e^{-i\delta x}b_1^2 = 0$$

$$a_1(x = 0, y) = \mathcal{A}_1(y)$$

$$a_2(x = 0, y) = \mathcal{A}_2(y)$$

$$b_1(x = M, y) = \mathcal{B}_1(y)$$

$$b_2(x = M, y) = \mathcal{B}_2(y)$$

$$(4.1)$$

plus appropriate boundary conditions on $y = 0$ and $y = N$. The K and L coefficients are $O(\alpha, \varepsilon)$, and are implicitly given by Equation (2.72) and Equation (2.73). If the boundary conditions $\mathcal{B}_1$ and $\mathcal{B}_2$ of the reflected wave are small, the reflected component is negligible. Assuming this is the case, the surface system is then

$$a_{1x} - iK_1 a_{1yy} + iK_3 f(x,y)a_1 + iK_5 e^{-i\delta x}a_1^* a_2 = 0$$

$$a_{2x} - iK_2 a_{2yy} + iK_4 f(x,y)a_2 + iK_6 e^{+i\delta x}a_1^2 = 0$$

$$a_1(x = 0, y) = \mathcal{A}_1(y)$$

$$a_2(x = 0, y) = \mathcal{A}_2(y).$$

$$(4.2)$$

Although the linear part of the surface system is identical to its counterpart in the Nonlinear Schrödinger Equation, the nonlinear terms endow the surface system with properties and behavior much unlike the Schrödinger Equation. The bottom evolution, is given by Equation (3.50):

$$\frac{\partial}{\partial T}h(x,y,T) = \frac{K}{\rho_0}(\mu_x + \nu_y)$$

$$h(x,y,0) = \mathcal{H}(x,y).$$

$$(4.3)$$

Equation (4.2) and Equation (4.3) comprise the full model. In Chapter 3 we gave an estimate of the time discrepancy for the evolution of the surface and bottom. This

discrepancy suggests an effective decoupling of the fluid and sediment problem. which permits an iterative solution to the full model. Specifically, begining with some initial bottom configuration $\mathcal{H}(x, y)$, the field on the surface is solved; the flux velocity (μ_x, ν_y) is calculated, and the bottom is updated using the mass transport equation. With this new bottom, the fluid quantities are solved for again and the process is repeated until some T final.

The conditions for which the surface system and the mass transport equation are stable enable us to discern the conditions for the overall stability of the iterative solution of the model. At this point in time the evidence of the surface system's solution stability comes from numerical calculations. Until the issue of stability of the surface system is studied in detail, it shall be assumed the solutions are stable and in what follows, and proceed to find conditions to be met by the mass transport equation so that the overall iterative procedure is stable.

The mass transport equation, from Equation (3.50), is of the form

$$\frac{\partial h(x, y, T)}{\partial T} = K(\mu_y + \nu_y) \text{ in } \mathcal{R}^2 \text{ with } T \in [0, \infty)$$

$$h(x, y, 0) = \mathcal{H}(x, y). \tag{4.4}$$

The properties of this quasi-linear hyperbolic equation are well known [62], and the existence and uniqueness of solutions is well established: provided the initial condition $h(x, y, 0) = \mathcal{H}(x, y)$ is at least in the C^1 class of functions, and the characteristics are nowhere parallel to the manifold on which the initial data is prescribed, we have either solutions in the weak or strong sense, i.e., smooth, or shock-like. A shock solution can either be prescribed as initial data, or can occur at some later time when the characteristics cross in space-time. Regarding the problem in sedimentary transport, a shock-like solution would make little sense as a solution. Since the possibility of such an outcome

exists, it is worth reviewing the conditions for the formation of a shock, and its relevance to the problem of sedimentary structure formation. Equation (4.4) may be recast as

$$\frac{\partial h(x,y,T)}{\partial T} = K(\frac{\partial \mu}{\partial h}h_x + \frac{\partial \nu}{\partial h}h_y)$$

$$h(x,y,0) = \mathcal{H}(x,y) \tag{4.5}$$

assuming that the indicated differentiations can be performed. If in the above system we identify $\mathbf{c} \equiv (\frac{\partial \mu}{\partial h}, \frac{\partial \nu}{\partial h}) \equiv (c_1, c_2)$ as propagation speeds, we may reinterpret the problem in terms of simple wave dynamics. Assuming the solution is wave-like, it may be inferred that

$$h - \mathcal{H}(x - Tc_1(h)) = O(\alpha) \tag{4.6}$$

since $\nu_y = O(\alpha)$ the second term on the right hand side of Equation (4.5) affects the outcome very minimally. Assume that $\mathcal{H}$ is differentiable. Using the implicit function theorem

$$h_T \approx -\frac{\mathcal{H}'}{1 + \mathcal{H}'c_{1h}T}$$

$$h_x \approx \frac{\mathcal{H}'}{1 + \mathcal{H}'c_{1h}T}. \tag{4.7}$$

It is evident from this pair of equations that, for $c_{1h} > 0$, if $\mathcal{H}' \geq 0$ for all x, both h_T and h_x shall remain bounded for all time. On the other hand, if $c_{1h} < 0$ at some point, h_T and h_x shall diverge as $1 + \mathcal{H}'c_{1h}T \to 0$. The situation is the reverse if $c_{1h} < 0$, of course. In the sediment problem, as is evident from Figures 4.1 and 4.2, it is typical for c_1 to be oscillatory in nature. Hence the characteristics have wave-like spatial dependence.

We need to reiterate the issue at hand: as the waves shoal, they "see" a bottom that is essentially fixed. Only after the passage of many waves do we expect to see changes on the bottom topography. Insofar as the solution of the model's system, we are concerned with the issue of stability in the iterative solution of the surface/bottom system, which
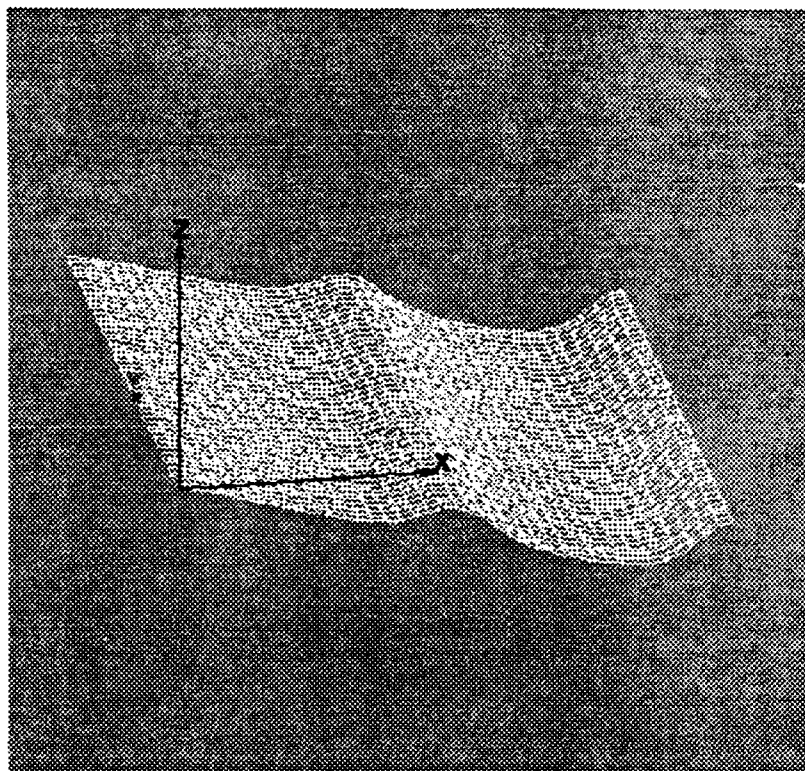
Figure 4.1: $c_1(T = 0)$ for bottom $f(T = 0) = 0.01x$. $\beta = 0.08$, $\varepsilon = 0.2$, $\alpha = 0.1$, $\omega_1 = 1.2$.

comprises the full model. We think of $\mathcal{H}$ as an entirely new initial condition as input to the conservation law at each value of T. We may ask then, when do the characteristics cross so that the solution is no longer valid? In what follows we think of $\mathcal{H}$ as an entirely new initial condition and T as the time between any two iterates of the full model. Set

$$1 + \mathcal{H}'c_{1h}T = 0. \tag{4.8}$$

If there is crossing of the characteristics, it shall occur at

$$T = -\frac{1}{\mathcal{H}'c_{1h}}. \tag{4.9}$$
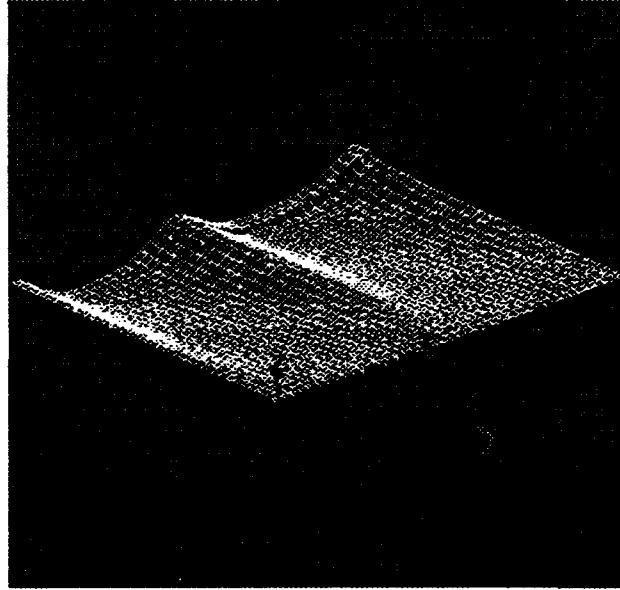
Figure 4.2: $c_1(T = 0)$, when $f(T = 0) = 0.01y$, $\beta = 0.08$, $\varepsilon = 0.2$, $\alpha = 0.1$, $\omega_1 = 1.2$.

For the two-dimensional case

$$c_{1h} = -\gamma_1 a_1^2 f_1(h) - \gamma_2 a_2^2 f_2(h),$$

$$\gamma_j = 4K\beta^2 k_j^3 H_j / \mu_j \omega_j$$

$$f_j = 1 - \frac{3}{2}\beta k_j^2 h^2 \tag{4.10}$$

thus, crossing occurs when

$$T = \frac{1}{\mathcal{H}'[\gamma_1 a_1^2 f_1(h) + \gamma_2 a_2^2 f_2(h)]}. \tag{4.11}$$

By assumption, $\mathcal{H}' = O(\varepsilon) = O(\alpha)$. Since k_j, ω_j, K, H_j are all $O(1)$, and $\mu_j = O(\beta^{1/2})$,

then $\gamma_j = O(\beta^{3/2})$. Thus, an estimate for the time at which crossing may occur is

$$T = \frac{1}{O(\alpha)O(\beta^{3/2})} \tag{4.12}$$

which can be quite a large interval assuming that $|a_i|$ remains bounded and less than one. This estimate applies to the three-dimensional case reasonably well since y variation is $O(\alpha)$ smaller than x variations. Equation (4.12) gives an upper bound on the time intervals between each iteration. Recall that we are considering each iterate as a new initial condition, and that the drift velocities will be different at each time step. Hence, if the upperbound in T given by Equation (4.12) is never reached –i.e., the model's assumptions are never violated – the iteration procedure yields a stable result.

4.1 The Surface Equations

As mentioned earlier, the surface system is a new equation whose properties and structure are presently unknown. In what follows, we present what we have been able to discern thus far about the structure of this new system.

4.1.1 Hamiltonian Structure

The following scaling,

$$x \leftarrow K_5(K_6E_0)^{1/2}x \quad y \leftarrow K_5^{1/2}(K_6E_0)^{1/4}y \quad \Delta Q \leftarrow \frac{\delta}{K_5(K_6E_0)^{1/2}}$$
$$u \leftarrow \frac{\sqrt{2}\phi}{(K_5E_0)^{1/2}} \qquad v \leftarrow \frac{\sqrt{2}\psi}{(K_6E_0)^{1/2}}, \tag{4.13}$$

shall be adopted in what follows in order to facilitate the derivation of the surface equation Hamiltonian structure. For a flat bottom, the system is thus

$$u_x - iK_1 u_{yy} + ie^{-i\Delta Qx} u^* v = 0$$

$$v_x - iK_2 v_{yy} + ie^{+i\Delta Qx} u^2/2 = 0 \tag{4.14}$$

Assume compact support in y for the dynamical variables. Define the Lagrangian density,

$$\mathcal{L} = iu_x u^* - iu_x^* u + iv_x v^* - iv_x^* v - \Re[(u^*)^2 v e^{-i\Delta Qx}] - K_1|u_y^2| - K_2|v_y^2| \qquad (4.15)$$

where $\Re$ stands for "the real part of", and the canonical momenta

$$
\begin{aligned}
\Pi_1 &= \frac{\partial \mathcal{L}}{\partial u_x} = iu^* \\
\Pi_2 &= \frac{\partial \mathcal{L}}{\partial v_x} = iv^* \\
\Pi_1^* &= \frac{\partial \mathcal{L}}{\partial u_x^*} = iu \\
\Pi_2^* &= \frac{\partial \mathcal{L}}{\partial v_x^*} = iv.
\end{aligned}
\qquad (4.16)
$$

The requirement that $L = \int \mathcal{L} dy$ be stationary, yields the Euler-Lagrange equations, which in turn lead to (4.14):

$$
\begin{aligned}
\frac{\partial \mathcal{L}}{\partial u^*} - \frac{d}{dy}\frac{\partial \mathcal{L}}{\partial u_y^*} &= iu_x + K_1 u_{yy} - e^{-i\Delta Qx} u^* v = 0 \\
\frac{\partial \mathcal{L}}{\partial v^*} - \frac{d}{dy}\frac{\partial \mathcal{L}}{\partial v_y^*} &= iv_x + K_2 v_{yy} - e^{+i\Delta Qx} u^2/2 = 0
\end{aligned}
\qquad (4.17)
$$

and its complex conjugates. The Hamiltonian H and its density $\mathcal{H}$ are given by

$$
\begin{aligned}
H &= \int \mathcal{H} dy \\
\mathcal{H} &= \Re[(u^*)^2 v e^{-i\Delta Qx}] + K_1|u_y|^2 + K_2|v_y|^2.
\end{aligned}
\qquad (4.18)
$$

Note that the Hamiltonian is not conserved, i.e.,

$$\frac{\partial L}{\partial x} = -\frac{\partial H}{\partial x} \neq 0, \qquad (4.19)$$

except when $\Delta Q = 0$. The Hamiltonian, in terms of the conjugate momenta is

$$\mathcal{H} = -i\Re[\Pi_1^2 \Pi_2^* e^{-i\Delta Qx}] + K_1|\Pi_{1y}|^2 + K_2|\Pi_{2y}|^2. \qquad (4.20)$$

The Hamiltonian admits a Poisson structure: Defining the Poisson bracket as

$$\{A, B\} \equiv \int dy [\frac{\partial A}{\partial u}\frac{\partial B}{\partial \Pi_1} - \frac{\partial A}{\partial \Pi_1}\frac{\partial B}{\partial u}] + c.c. + \int dy [\frac{\partial A}{\partial v}\frac{\partial B}{\partial \Pi_2} - \frac{\partial A}{\partial \Pi_2}\frac{\partial B}{\partial v}] + c.c. \qquad (4.21)$$

so that the evolution of a dynamical variable A is given by

$$A_x = \{A, H\}. \tag{4.22}$$

In fact, Equation (4.14) is recovered if A is replaced by u and v in the above equation:

$$
\begin{aligned}
u_x = \{u, H\} = \frac{\partial H}{\partial \Pi_1} &= -i\Pi_1 \Pi_2^* e^{-i\Delta Qx} - \Pi_{1yy}^* \\
&= iu^* v e^{-i\Delta Qx} + iu_{yy} \\
v_x = \{v, H\} = \frac{\partial H}{\partial \Pi_2} &= -i(\Pi_1^*)^2 e^{+i\Delta Qx}/2 - \Pi_{2yy}^* \\
&= iu^2 e^{+i\Delta Qx}/2 + iv_{yy}. \tag{4.23}
\end{aligned}
$$

In addition,

$$
\begin{aligned}
\Pi_{1x} = \{\Pi_1, H\} &= -\frac{\partial \mathcal{H}}{\partial u} \\
\Pi_{2x} = \{\Pi_2, H\} &= -\frac{\partial \mathcal{H}}{\partial v} \tag{4.24}
\end{aligned}
$$

yield the complex conjugate equations.

Equation (4.14) may be recast in the form of an autonomous system. For such a system, the Hamiltonian is a conserved quatity. Let $\tilde{v} = v e^{-i\Delta Qx}$, and substitute in Equation (4.14), resulting in

$$
\begin{aligned}
u_x - iK_1 u_{yy} + iu^* \tilde{v} &= 0 \\
\tilde{v}_x - iK_2 \tilde{v}_{yy} + i\Delta Q\tilde{v} + iu^2/2 &= 0. \tag{4.25}
\end{aligned}
$$

The Hamiltonian corresponding to Equation (4.25) is

$$\tilde{H} = \Re[(u^*)^2 \tilde{v}] + K_1 |u_y|^2 + K_2 |\tilde{v}_y|^2 + \Delta Q|\tilde{v}|^2/2. \tag{4.26}$$

As a check:

$$u_x = \{u, \mathcal{H}\} = -\frac{\partial \mathcal{H}}{\partial u^\star} \quad = \quad -iu^\star\tilde{v} + iK_1 u_{yy}$$

$$\tilde{v}_x = \{\tilde{v}, \mathcal{H}\} = -\frac{\partial \mathcal{H}}{\partial \tilde{v}^\star} \quad = \quad -i\Delta Q\tilde{v} - iu^2/2 + iK_2 v_{yy}. \tag{4.27}$$

Hence, the above substitution leads to a Hamiltonian with the property

$$\frac{d\mathcal{H}}{dx} = 0 \tag{4.28}$$

for any ΔQ.

Another conserved quantity of this Hamiltonian can be shown to be

$$\frac{1}{2}(|u|^2 + |\tilde{v}|^2)_x = -\Im(K_1 u_y u^\star + K_2 \tilde{v}_y \tilde{v}^\star)_y, \tag{4.29}$$

where $\Im$ reads as "the imaginary part of".

4.1.2 An Exactly Solvable Case

When the bottom is flat, and the boundary conditions are constant, the surface system becomes

$$a_{1x} + iK_5 e^{-i\delta x} a_1^\star a_2 = 0$$

$$a_{2x} + iK_6 e^{+i\delta x} a_1^2 = 0$$

$$a_1(x = 0, y) = \mathcal{A}_1 \tag{4.30}$$

$$a_2(x = 0, y) = \mathcal{A}_2,$$

where, $\mathcal{A}_j$ are constants. The above system is very familiar to the nonlinear optics community–c.f. Arsmtrong et al. [63]. Replacing $a_i = A_i(x)\exp\theta_i(x)$ in Equation (4.30) changes the system to

$$A_{1x} - K_5 A_1 A_2 \sin\Omega = 0$$

$$A_{2x} + K_6 A_1^2 \sin\Omega = 0 \tag{4.31}$$

for the real part, and

$$\theta_{1x} + K_5 A_2 \cos \Omega = 0$$
$$A_2 \theta_{2x} + K_6 A_1^2 \cos \Omega = 0$$

(4.32)

for the imaginary part, where $\Omega = 2\theta_1 - \theta_1 + \delta x$. Combining the equations from the imaginary part,

$$\Omega_x + \delta + [K_6 A_1^2/A_2 - 2K_5 A_2] \cos \Omega = 0.$$

(4.33)

Thus, Equation (4.30) is equivalent to

$$A_{1x} - K_5 A_1 A_2 \sin \Omega = 0$$

$$A_{2x} + K_6 A_1^2 \sin \Omega = 0$$

$$\Omega_x + \delta + [K_6 A_1^2/A_2 - 2K_5 A_2] \cos \Omega = 0$$

$$A_1(0) = \mathcal{A}_1$$

$$A_1(0) = \mathcal{A}_1$$

$$\Omega(0) = \Omega_0.$$

(4.34)

To continue, let

$$X = A_2 \sin \Omega$$

(4.35)

$$Y = A_2 \cos \Omega$$

(4.36)

$$Z = A_1^2.$$

(4.37)

Multiplying the second equation of Equation (4.34) by $\sin \Omega$, using the third expression of Equation (4.34) it can be discerned that

$$X_x = -K_6 Z - \delta Y + 2K_5 Y^2,$$

(4.38)

since $X_x = A_{2x}\sin\Omega + A_2\Omega_x\cos\Omega$. Multiplying the third expression of (4.34) by $A_2\sin\Omega$,

$$Y_x = \delta X - 2K_5 XY, \tag{4.39}$$

after making use of the second equation in Equation (4.34). The Z variable may be eliminated from Equation (4.38) by noting that from the real part of the original system that conservation of energy is given by

$$K_5(X^2 + Y^2) + K_6 Z = E_0. \tag{4.40}$$

Eliminating Z using Equation (4.40), dividing Equation (4.38) by Equation (4.39), leads to

$$\frac{dX}{dY} = \frac{K_5(X^2 + 3Y^2) - \delta Y - E_0}{(\delta - 2K_5 Y)X}, \tag{4.41}$$

which may be used to investigate the structure of the phase plane of A_2. The dynamics of A_1 follow immediately from the conservation of the energy constraint, Equation (4.40). Three cases, depending on the size of the detuning parameter δ, are investigated. A plot of the detuning parameter as a function of frequency and β is shown in Figure 4.3, for the dispersion relation given by Equation (2.46). When $\delta/2\sqrt{E_0} \sim 0$, the phase plane is shown in Figure 4.4. Note that $dX/dY = 0$ and $X = 0$ gives the two centers, at $(X, Y) = (0, \pm\sqrt{E_0}/\sqrt{3K_5})$. Setting $Y = 0$, $dX/dY = 0$ gives the radius of the bounding circle, at $\sqrt{E_0}/\sqrt{K_5}$, beyond which the orbits diverge. Additionally, there are two saddle points at $(X, Y) = (\pm\sqrt{E_0}/\sqrt{K_5}, 0)$. Motion along the limiting circle takes place in such a way that $A_1 = 0$, and $A_2 = E_0/\sqrt{K_5}$. If we start, for example, with $A_1 \neq 0$ and $A_2 = 0$, motion in the plane takes place along the line $Y = 0$ up to the limiting curve, the phase Ω is then equal to $\pi/2$. From the imaginary part of the original system, it may be deduced that the variation of Ω in this limit is described by

$$\Omega_x - 2K_5 E_0^{1/2}\cos\Omega = 0. \tag{4.42}$$
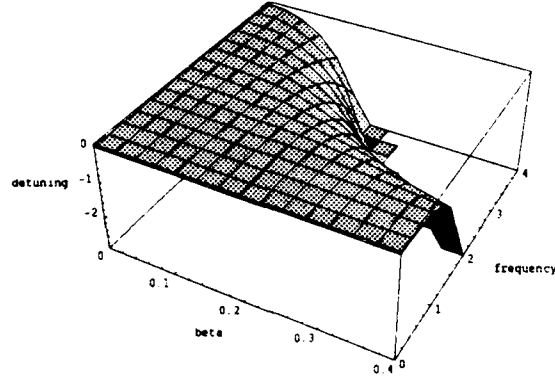
Figure 4.3: Detuning parameter dependence on ω_1 and β.

The transition from the state $\sin\Omega = 1$ to $\sin\Omega = -1$ occurs along the limiting circle. The distance x at which this transition occurs is infinite, but it can be estimated by solving Equation (4.42). The solution is

$$\Omega = \tan^{-1}[\exp(-2K_5 E_0^{1/2} x)\tan\Omega_0], \qquad (4.43)$$

and hence an estimate of the spatial length at which the energy of the first harmonic makes an almost complete transition to the second harmonic is

$$L \approx 1/2K_5 E_0^{1/2}, \qquad (4.44)$$

which shall subsequently be seen as related to the "interaction length". The variation of the amplitude of A_2 along $Y = 0$ may be discerned from

$$A_{2x} = K_5 A_2^2 - E_0, \qquad (4.45)$$
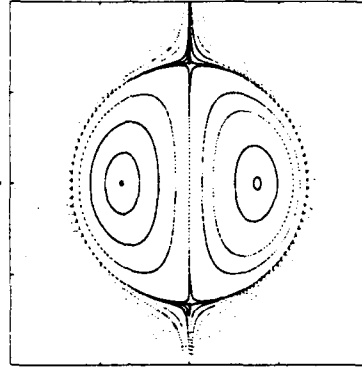
Figure 4.4: Phase plane for A_2 for $\delta \sim 0$. X axis is vertical.

which is obtained by eliminating Z from Equation (4.38), and making use of the energy relationship.

The solution of Equation (4.45) is

$$A_2 = (E_0/K_5)^{1/2} \tanh[K_5^{1/2} E_0^{1/2}(x - x_0)], \tag{4.46}$$

with $\mathcal{A}_2 = (E_0/K_5)^{1/2} \tanh[(K_5 E_0)^{1/2} x_0]$. At the begining of the growth process, $A_1 \gg A_2$ so that $\sin \Omega = 1$ and the growth of the second mode is independent of $\mathcal{A}_2$. With the solution of A_2 in hand, using Equations (4.39) and the first expression of Equation (4.34), it may be shown that

$$A_1(x) = \frac{\mathcal{A}_1}{\sqrt{1 - \tanh^2[K_5^{1/2} E_0^{1/2} x_0]}} sech \sqrt{K_5 E_0}(x - x_0). \tag{4.47}$$

From this solution it is concluded that irreversible energy conversion takes place for $\delta = 0$. This solution is not stable, however, since the stationary states are reached by motion along the limiting curve on the phase plane. The smallest of δ invariably results in motion along homoclinic orbits with consequent of beat in the amplitude of A_1 and

A_2.

For the case $\delta \neq 0$, but small compared to $2E_0^{1/2}$, the curves have similar structure to the case previously discussed. The phase is described by

$$\Omega_x + \delta - 2K_5 E_0^{1/2} \cos \Omega = 0. \tag{4.48}$$

Consequently, the interaction length is decreased:

$$L = \frac{1}{\sqrt{4K_5 E_0^{1/2} - \delta^2}}. \tag{4.49}$$

The centers are now at $(X, Y) = (0, \frac{\delta}{6K_5}[1 \pm \sqrt{1 + \frac{12K_5 E_0}{\delta^2}}])$, and the line $Y = 0$ is no longer the line of symmetry. Also, the line $Y = \frac{\delta}{6K_5}$ does not generally intersect the limiting circle, as can be seen in Figure 4.5. Instead of two pairs of stationary solutions,
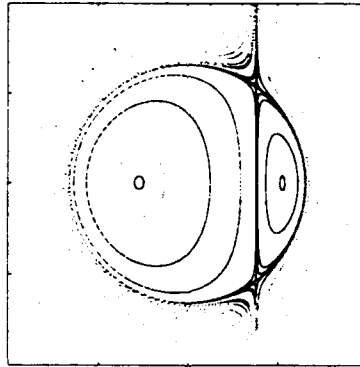
Figure 4.5: Phase plane for A_2 for $\delta/2E_0^{1/2} \ll 1$. X axis is vertical.

only one is possible, and the energy is concentrated mainly in the lower mode. The two modes interact weakly, and the spatial beats get smaller and shallower as the detuning paramenter is increased. In fact, when $\delta/2E_0^{1/2} \gg 1$, $A_1(x) \sim \mathcal{A}_1$, and $A_2(0) = \mathcal{A}_2$, the

first two terms in Equation (4.33) are dominant, so that the phase is

$$\Omega = \delta x + \pi/2. \tag{4.50}$$

Substituting the above expression into the second expression of Equation (4.34) we obtain

$$A_2 = \mathcal{A}_2 + \frac{K_6}{\delta}\mathcal{A}_1^2 \sin \delta x. \tag{4.51}$$

The phase portrait for this case is shown in Figure 4.6.
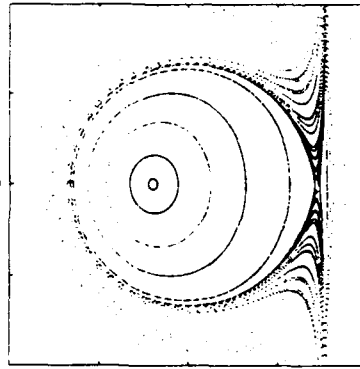
Figure 4.6: Phase plane for A_2 for $\delta/2E_0^{1/2} \gg 1$. X axis is vertical.

Note that of the three cases considered here, the only ones physically relevant to the sandbar generation problem are the first two cases. The large detuning parameter case violates assumptions on the size of the wavenumber/frequency in the model. However, much is to be learned about the surface system from looking at the high frequency case in detail.

When ω_1 is large, or equivalently, when δ is large. the amount of energy from the first mode transferred to the second one may be quite small. As was just mentioned, in such case the first mode has nearly constant amplitude. Assume that the boundary conditions

are constant, i.e. $a_j(0) = \mathcal{A}_j$. Thus, $a_1(x) \sim \mathcal{A}_1$, and the second mode expression of Equation (4.2) may be integrated, yielding

$$a_2(x) = \frac{K_6}{\delta}\mathcal{A}_1^2 e^{\delta x}. \tag{4.52}$$

Substituting Equation (4.52) into the first mode equation

$$a_{1x}(x) \approx \frac{iK_5}{\delta}a_1|\mathcal{A}_1^2|e^{-\delta x}, \tag{4.53}$$

which can readily be integrated to yield

$$a_1(x) = \mathcal{A}_1 e^{\sigma x}, \tag{4.54}$$

where $\sigma = K_5 K_6/\delta|\mathcal{A}_1^2|$. Thus $a_1(x)$ is approximately sinusoidal with a wavelength proportional to $|\mathcal{A}_1^2|$.

For a nonzero bottom an exact solution is not possible. Consider, however, the case

$$\begin{aligned} A_{1x} - K_5 A_1 A_2 \sin\Omega + \chi_1 A_1 &= 0 \\ A_{2x} + K_6 A_1^2 \sin\Omega + \chi_2 A_2 &= 0 \end{aligned} \tag{4.55}$$

where χ_j represent constants. We still cannot solve this system analytically, unless $\chi_1 = \chi_2 = \chi$, in which case, conservation of energy is given by

$$K_5 A_1^2 + K_6 A_2^2 = E_0 e^{-2\chi x}. \tag{4.56}$$

Introducing new variables

$$\begin{aligned} X &= \tilde{X} E_0^{1/2} e^{-\chi x} \\ Y &= \tilde{Y} E_0^{1/2} e^{-\chi x} \end{aligned} \tag{4.57}$$

and the reduced distance

$$\xi = 2E_0^{1/2}(1 - e^{-\chi x})/\chi, \tag{4.58}$$

assuming $\delta = 0$, we obtain, using Equation (4.56) the system's phase plane equation

$$2\frac{d\tilde{X}}{d\tilde{Y}} = \frac{1 - \tilde{X}^2 - 3\tilde{Y}^2}{\tilde{X}\tilde{Y}}, \tag{4.59}$$

which has the same structure in the phase plane as that shown in Figure 4.4. The important distinction is that ξ is related nonlinearly to x. Whence, the damping of the waves is characterized by

$$\tilde{\chi} = \chi/(2K_5E_0^{1/2}). \tag{4.60}$$

For $\tilde{\chi} \ll 1$, there is weak damping and the waves travel a considerable distance before the energy is fully dissipated. On the other hand, if $\tilde{\chi} \gg 1$, only a small arc of the trajectory in phase plane is traversed. The wave substantially attenuates in a short distance. The relevant case, at least approximately, to the oceanic problem considered in this study is the former case, in which the size of the bottom makes the coefficient analogous to χ in the above presentation of $O(\alpha)$ in size relative to the other terms in Equation (4.55).

With an understanding of the dynamics of the system, we now present the analytical solution to this special case, Equation (4.30). Our development follows closely Armstrong et al. [63]. For the sake of tidiness, let us scale Equations(4.30), using

$$w(x) = \frac{|a_1(x)|}{\sqrt{K_5E_0}}$$

$$v(x) = \frac{|a_2(x)|}{\sqrt{K_6E_0}}$$

$$\tilde{x} = K_5\sqrt{K_6E_0}x$$

$$\Delta Q = \frac{\delta}{K_5\sqrt{K_6E_0}}. \tag{4.61}$$

In these new variables, conservation of energy assumes the simple form

$$v^2(x) + w^2(x) = 1 \tag{4.62}$$

and Equation (4.30) is expressed as

$$\frac{dw}{d\tilde{x}} = -wv\sin\Omega$$

$$\frac{dv}{d\tilde{x}} = w^2\sin\Omega$$

$$\frac{d\Omega}{d\tilde{x}} = \Delta Q + \cot\Omega\frac{d}{d\tilde{x}}(\ln(w^2v)). \tag{4.63}$$

$\Omega = 2\theta_1(\tilde{x}) - \theta_2(\tilde{x}) + \Delta Q\tilde{x}$ here. For $\Delta Q = 0$, i.e. perfect phase match, Equation (4.63) provides another constant of integration

$$\Gamma = w^2v\cos\Omega = w^2(0)v(0)\cos\Omega(0). \qquad \cdot \tag{4.64}$$

Thus, making use of this constant of integration, and conservation of energy, it readily follows from Equation (4.63) that

$$\frac{dv^2}{d\tilde{x}} = \pm 2[v^2(1-v^2)^2 - \Gamma^2]^{1/2}, \tag{4.65}$$

with the sign being determined by the sign of $\sin\Omega(0)$. Hence

$$\tilde{x} = \pm\int_{v^2(0)}^{v^2(\tilde{x})}\frac{d(v)^2}{[v^2(1-v^2)^2 - \Gamma^2]^{1/2}} \tag{4.66}$$

which is the Complete Elliptic Integral. Since v is real and less than or equal to 1, v^2 is constrained to move between the two lowest roots of $v^2(1-v^2)^2 - \Gamma^2$. Call these $v_a < v_b$. We then arrive at a general definition for the interaction length–c.f. Equation (4.44)– which is the spatial expanse in which the solution goes from one root to the other.

$$L_{\tilde{\lambda}} \equiv \int_{v_a^2}^{v_b^2}\frac{d(v)^2}{[v^2(1-v^2)^2 - \Gamma^2]^{1/2}}. \tag{4.67}$$

If the boundary conditions are such that $\Gamma = 0$, $v_a^2 = 0, v_b^2 = 1$, and $L_{\tilde{\lambda}} \rightarrow \infty$, the solutions would be

$$v_{\Gamma=0} = \tanh(\tilde{x} + \tilde{x}_0)$$

$$w_{\Gamma=0} = sech(\tilde{x} + \tilde{x}_0). \qquad (4.68)$$

The case $\tilde{x}_0 = 0$ corresponds to $\mathcal{A}_2 = 0$. On the other hand, if $\mathcal{A}_1 = 0$, then $\tilde{x}_0 \to \infty$.

If both $\mathcal{A}_j \neq 0$ and $\theta_2(0) - 2\theta_1(0) = \pm\pi/2$, depending on $sin\Omega(0) = \pm 1$, the second harmonic or the fundamental gets amplified first. If the fundamental gets amplified first ($\tilde{x}_0 < 0$), the second harmonic decreases to zero and then increases until all the energy is in the second harmonic. If the second harmonic is amplified first ($\tilde{x}_0 > 0$), there is complete energy conversion.

To write down the explicit solutions, define $v_c^2 > v_b^2 > v_a^2$, the third root of

$$v^2(1 - v^2)^2 - \Gamma^2 = 0. \qquad (4.69)$$

Let

$$y^2 = \frac{(v^2 - v_a^2)}{(v_b^2 - v_a^2)},$$

$$\gamma^2 = \frac{v_b^2 - v_a^2}{(v_c^2 - v_a^2)} \qquad (4.70)$$

be the argument and modulus, then

$$\tilde{x} = \frac{\pm 1}{\sqrt{(v_c^2 - v_a^2)}} \int_{y(0)}^{y(\tilde{x})} \frac{dy}{[(1 - y^2)(1 - \gamma^2 y^2)]^{1/2}} \qquad (4.71)$$

and the amplitude squared solutions are, in terms of Jacobi Elliptic functions "sn",

$$v^2(\tilde{x}) = v_a^2 + (v_b^2 - v_a^2)sn^2[(v_c^2 - v_a^2)^{1/2}(\tilde{x} + \tilde{x}_0); \gamma]$$

$$w^2(\tilde{x}) = 1 - v^2(\tilde{x}), \qquad (4.72)$$

with $\tilde{x}_0$ being determined by the boundary condition $y^2(0)$ and the value of γ. Note that $\Gamma_{max}^2 = 4/27$, as determined from Equation (4.72) and Equation (4.69).

The solutions for imperfect phase matching, $\Delta Q \neq 0$, can be found, using variation

of parameters. Equation (4.64) is now

$$\Gamma_{\Delta Q} = w^2 v \cos \Omega + \frac{1}{2} \Delta Q v^2, \tag{4.73}$$

so that

$$\Gamma_{\Delta Q} = \Gamma + \frac{1}{2} \Delta Q v^2(0). \tag{4.74}$$

Equation (4.66) in this instance is given by

$$\tilde{x} = \pm \frac{1}{2} \int_{v^2(0)}^{v^2(\tilde{x})} \frac{d(v)^2}{[v^2(1-v^2)^2 - [\Gamma^2 - \frac{1}{2}\Delta Q(v^2 - v^2(0))]^2]^{1/2}}. \tag{4.75}$$

The three roots are given by

$$v^2(1-v^2)^2 - [\Gamma^2 - \frac{1}{2}\Delta Q(v^2 - v^2(0))]^2 = 0. \tag{4.76}$$

The interaction length is now

$$\tilde{L}_\lambda = \frac{2K}{(v_c^2 - v_a^2)^{1/2}} \tag{4.77}$$

where

$$K = K(\gamma) = \int_0^{\pi/2} (1 - \gamma^2 \sin^2 y)^{-1/2} dy \tag{4.78}$$

is the Complete Elliptic Integral. In terms of the unscaled variables,

$$L_\lambda = \frac{2K}{(v_c^2 - v_a^2)^{1/2} K_5 (K_6 E_0)^{1/2}}. \tag{4.79}$$

By way of illustration, the case when $\mathcal{A}_1 = 0.5$ and $\mathcal{A}_2 = 0$, yields a particularly simple expression. In this case $\Gamma_{\Delta Q} = 0$; $v_a = 0 = \tilde{x}_a$, $v_c = 1/v_b$, and $\gamma = v_b^2$. Let $m = v_b^2$. Since $v_b^2 = v_c^{-2} = (1 + (\frac{\Delta Q}{4})^2)^{1/2} - \frac{\Delta Q}{4}$, then

$$\tilde{L}_\lambda = 2K(m),$$

$$v^2 = m sn^2[m^{-1/2}\tilde{x}; m]. \tag{4.80}$$

The solution for small ΔQ and large ΔQ is graphically depicted in Figure 4.7. In

the first case, v_b and $\tilde{L}_\lambda$ are relatively insensitive to ΔQ and substantial power transfer occurs, the interaction length is very large. On the other hand, for $\Delta Q \gg 1$, there is less power transfer and the interaction length is shorter. Figure 4.8 shows how the interaction length varies nonlinearly with m (and hence with ΔQ), and in Figure 4.9 and Figure 4.10 illustrate the dependence of the interaction length on the size of the nonlinear parameter α, and the dispersion parameter β. The relevant size of the parameters α and β in the oceanic application under consideration is as high as 0.15 for α, and $0.005 < \beta < 0.15$. Hence, from the graphs it may be inferred that the interaction length is more sensitive to dispersion than to nonlinearity for the above-mentioned ranges of α and β.
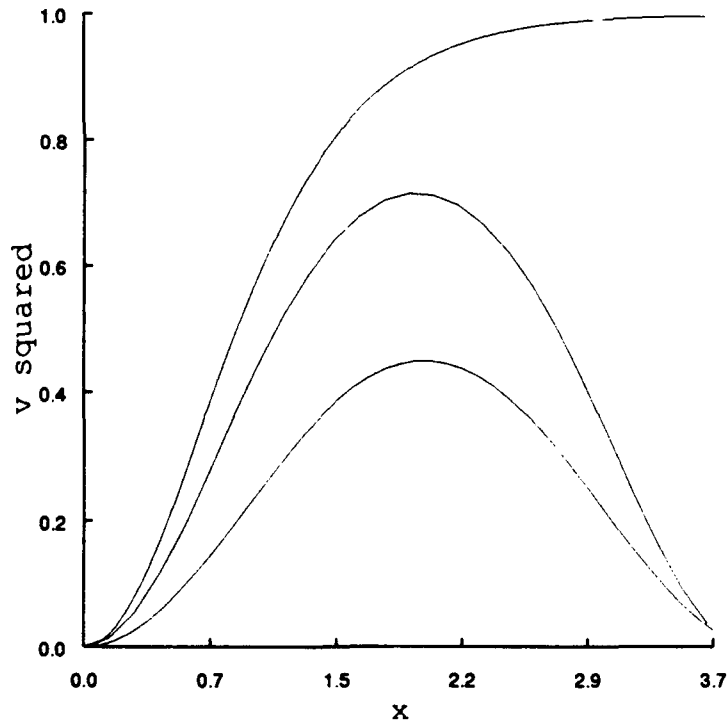
Figure 4.7: v^2 dependence on the detuning parameter. In all cases $w^2(x = 0) = 1$. The interaction length and the power transferred to v^2 decreases as ΔQ increases.

As a way to assess the evolution of waves with periodicity in the longshore direction,
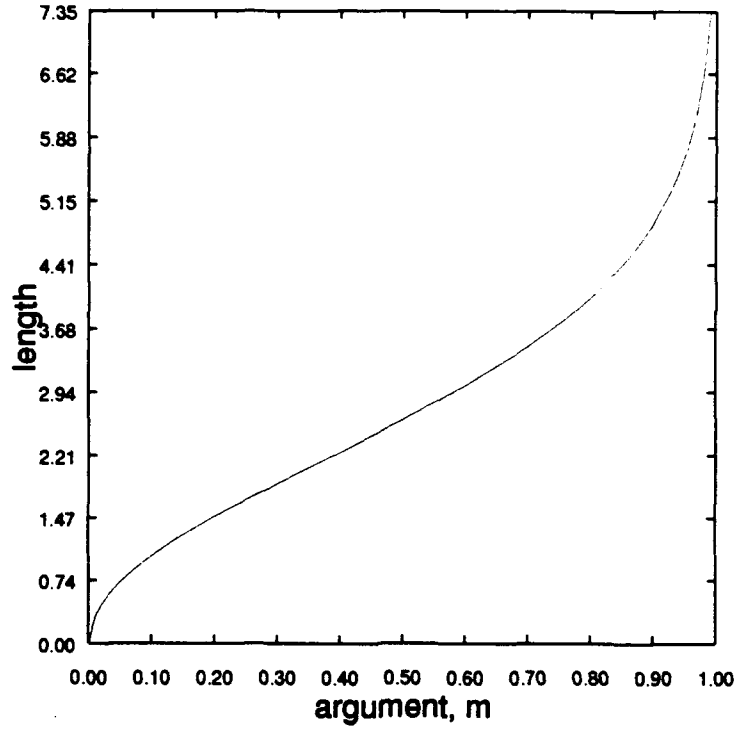
Figure 4.8: Interaction length dependence on the nonlinear parameter ΔQ.

suppose

$$
\begin{aligned}
a_1(x,y) &= u(x,y)e^{i(k_1x-\omega_1t+l_1y)} \\
a_2(x,y) &= v(x,y)e^{i(k_2x-\omega_2t+l_2y)}
\end{aligned}
\tag{4.81}
$$

Then the system (4.2) is now

$$
u_x + il_1^2K_1u + iK_5u^\star ve^{-i(\gamma y+\delta x)} = 0
\tag{4.82}
$$

$$
v_x + il_2^2K_2v + iK_6u^2e^{+i(\gamma y+\delta x)} = 0,
\tag{4.83}
$$

where $\gamma = l_2 - 2l_1$, which can be zero. Consideration shall be made here to the high frequency case. For ω_1 large, $u(x,y) \sim u^0$. Hence Equation (4.83) may be integrated,
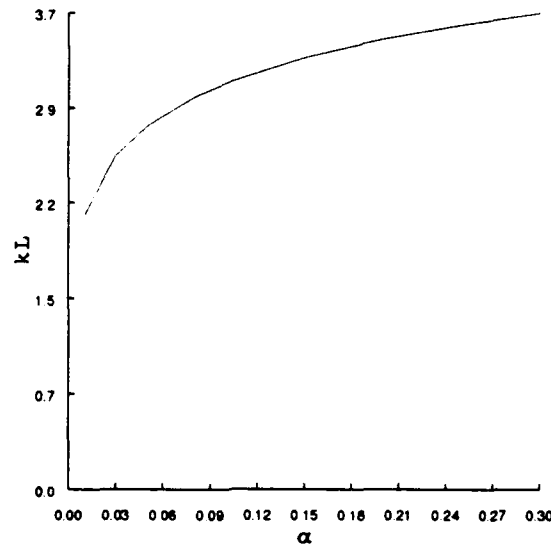
Figure 4.9: Interaction length dependence on the nonlinear parameter α.

yielding

$$v = -\frac{K_6 u^2 e^{i(\gamma y + \delta x)}}{\delta + l_2^2 K_2},$$ (4.84)

assuming $v(x = 0, y) = 0$ and $u(x = 0, y) = u^0$ constant. Using this expression in Equation (4.82),

$$u(x, y) = u^0 \exp[-il_1^2 K_1 x + i\frac{K_5 K_6 |u^0|^2 x}{\delta + l_2^2}].$$ (4.85)

Hence v oscillates with lines of constant phase normal to the $\tan^{-1}(\frac{\gamma}{\delta})$ direction, where the angle is taken with respect to the shoreward direction. When $l_2 = 2l_1$ exactly, the direction of constant phase orthogonals is the shoreward direction. On the other hand, u oscillates in the x direction, with a repetition length

$$L_\gamma = \frac{\delta + l_2^2 K_2}{2\pi} \{K_5 K_6 |u^0|^2 - (\delta + l_2^2 K_2) l_1^2 K_1\}^{-1}.$$ (4.86)

Furthermore, v can develop a singularity when

$$\delta + l_2^2 K_2 = 0.$$ (4.87)
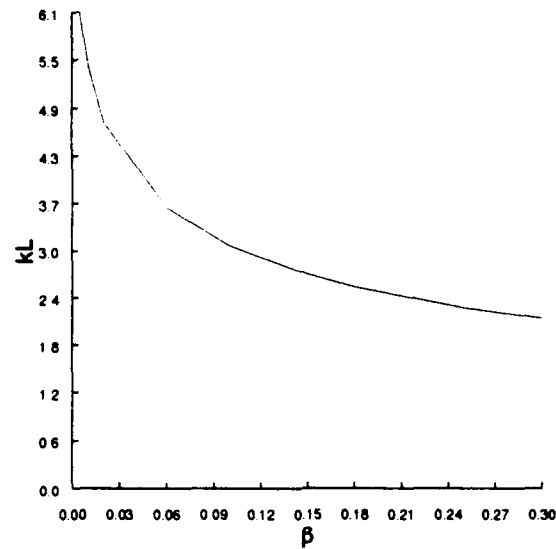
Figure 4.10: Interaction length dependence on the dispersion parameter β.

that is, when $l_2 = \pm\sqrt{-\delta/K_2}$ (note that $\delta \leq 0$). In terms of the y component of the wavenumber, the singularity occurs when

$$l_2 = \pm\sqrt{\frac{-2\delta k_2}{\alpha}}. \qquad (4.88)$$

An l_2 of such value is not at all unreasonable to consider. A singularity must be investigated much further, since it is most likely a result of the method of analysis used here. However, there is a change in sign in v on either side of the location at which the singularity is predicted.

Yet another interesting feature is the situation when

$$|u^0|^2 = (\delta + l_2^2 K_2)l_1^2 K_1/K_5 K_6 \qquad (4.89)$$

again, a reasonable value. In such an event, the modulation of u practically disappears. Then

$$u(x,y) \approx u^0 = \pm\sqrt{(\delta + l_2^2 K_2)l_1^2 K_1/K_5 K_6} \qquad (4.90)$$

and

$$v(x,y) = -\frac{l_1^2 K_1 e^{i(\delta x + \gamma y)}}{K_5} \tag{4.91}$$

which is a simple sine wave. Hence, one could conceivably use modulations in the y direction to nonlinearly produce linear sine wave signals of the second harmonic with amplitude given by l_1^2. If $l_2 = 2l_1$ exactly, the wave oscillates in the shoreward direction.

Carrying out this high frequency analysis further, we can consider the effect of the bottom topography under special circumstances: the case when $f(x,y) = f(y)$ leads in a straight-forward manner to

$$v = -\frac{K_6 u^2 e^{i(\gamma y + \delta x)}}{\delta + l_2^2 K_2 + K_4 f(y)}, \tag{4.92}$$

again, assuming $v(x = 0, y) = 0$ and $u(x = 0, y) = u^0$ constant, and

$$u(x,y) = u^0 \exp[-il_1^2 K_1 x + i\frac{K_5 K_6 |u^0|^2 x}{\delta + K_2 l_2^2 + K_4 f(y)}]. \tag{4.93}$$

Thus, the effect of the bottom in this case is to change the amplitude of v, and at the same time modulate the oscillations of u. Again, the possibility of a singularity and a change in sign in v exists.

Finally, the same method may be employed to assess the effect of a mildly sloping bottom on the high frequency solution. Assume $f(x,y) = \nu x/2$, where ν is small. The same procedure leads to

$$
\begin{aligned}
v &\approx -\frac{(u^0)^2 K_6 e^{i(\gamma y + \delta x)}}{\delta + K_2 l_2^2} \\
&\quad [1 - i\frac{2K_4 \nu}{(\delta + K_2 l_2^2)^2}\{(\delta + K_2 l_2^2)^2 x^2/2 + i(\delta + K_2 l_2^2)x - 1\}]e^{-iK_4 \nu x^2} \\
u &\approx u^0 \exp\{-i(K_1 l_1^2 \\
&\quad -\frac{|u^0|^2 K_5 K_6}{(\delta + K_2 l_2^2)^2})x - i(K_3 - \frac{|u^0|^2 K_4 K_5 K_6}{(\delta + K_2 l_2^2)^2})\nu x^2\} \\
&\quad \exp -\frac{2|u^0|^2 K_4 K_5 K_6 \nu}{(\delta + K_2 l_2^2)^3}(x - \frac{(\delta + K_2 l_2^2)^2 x^2}{2})
\end{aligned} \tag{4.94}
$$

The result is only valid for $K_4\nu x^2 \ll 1$. That is, since K_4 is of the same order as $k_2\varepsilon$, it is valid for $x \ll O(1/\sqrt{k_2\varepsilon\nu})$. In order to discern what is fundamentally different about the sloping case, consider the situation in which u^0 has no y dependence, so that Equation (4.94) has the form

$$v \approx -\frac{(u^0)^2 K_6 e^{i\delta x}}{\delta}$$
$$[1 - i\frac{2K_4\nu}{\delta^2}(\frac{\delta^2 x^2}{2} - i\delta x - 1)]e^{-iK_4\nu x^2}$$
$$u \approx u^0 \exp\{i|u^0|^2 K_5 K_6 x/\delta - i(K_3 - \frac{|u^0|^2 K_4 K_5 K_6}{\delta^2})\nu x^2\}$$
$$e^{\frac{-2|u^0|^2 K_4 K_5 K_6 \nu}{\delta^3}(x-\delta^2 x^2/2)} . \tag{4.95}$$

From Equation (4.95) it is readily apparent that v oscillates proportionally to $\epsilon^{i\delta x}$, its maximum amplitude δ/K_6 times smaller than u^2. The phase will drift quadratically with distance and proportionally to $K_4\nu$. The amplitude drops linearly at a rate proportional to the size of $K_4\nu$ and $K_3\nu$; the wave decays exponentially at a rate controlled by the last exponential in the above expression. To properly interpret the decay, recall that $|\delta| \gg 1$ and δ is strictly negative in this analysis. The second term in the exponential implies that decay/blow up would be a possible outcome of the original model. However, this is an artifice of the present analysis. If the assumption $u(x) \sim$ constant is violated, the above expressions are not valid. Thus, for our interpretation to be valid, it is required that $2|u|^2 K_4 K_5 K_6 \nu x/\delta^3 \ll 1$.

A very important question that arises in the applicability of slightly resonant interacting triad expansion techniques to oceanic waves, is that we may be neglecting very important side-band modulations. These can be producing interesting structure, control-

ling the stability of the primary waves, or affecting very minimally the structure of the evolving waves. A general result on this issue is forthcoming. but for now we limit our attention to the high frequency case. The problem of bands, rather than isolated modes, and its effect on the evolution of individual waves has been examined by Hasselmann [64] in the context of deep oceanic waves. We would like to find the effect of side bands on the main waves for the shallow water case. The following analysis follows closely work done by Brekhovskikh and Goncharov [65] in connection with this issue.

Firstly, the modal expansion is replaced by the more familiar expression for the lowest order velocity

$$u_0(x,t) = \int_{-\infty}^{\infty} a_\omega(x) e^{-i\omega t} d\omega \qquad (4.96)$$

where $a_\omega(x) \equiv a(x,\omega)$, and $a_\omega^*(x) = a_{-\omega}(x)$ since u_0 is real. Assume $a_\omega = \rho_\omega \exp(ik_\omega x)$, where $k_\omega = k(\omega)$ is found via the dispersion relation. Again reality means that $k_\omega^* = k_{-\omega}$ and $\rho_\omega^* = \rho_{-\omega}$. Substituting Equation (4.96) into the original equations and using the compatibility conditions, an expression for the amplitude of the incident waves is

$$\frac{\partial}{\partial x}\rho_\omega = -i\alpha\omega \int_{-\infty}^{\infty} \rho_q \rho_s \exp(-i\Delta_{qs\omega}x)dq \qquad (4.97)$$

where $s = \omega - q$, and $\Delta_{qs\omega} = q + s - k_\omega$. If the incoming harmonic wave $u(0,t) = a_1(0)e^{-i\omega_1 t} + c.c.$, i.e. $\rho_\omega(0) = a_1(0)\delta(\omega - \omega_1) + a_1^*(0)\delta(\omega + \omega_1)$, the spectrum of $u(x,t)$ remains discrete at any time: the only non-zero components are $\omega_n = n\omega_1$, $k_n = k(\omega_n), n = \pm 1, \pm 2, \cdots$ and

$$a_\omega(x) = \sum_n a_n(x)\delta(\omega - \omega_n). \qquad (4.98)$$

Then Equation (4.97) yields

$$\frac{\partial}{\partial x}a_n = -i\alpha\omega_n \sum_m a \; a_l e^{-i\Delta_{mln}x}, \qquad (4.99)$$

$l = n - m$, $\Delta_{mln} = k_m + k_l - k_n$, $a_n = a_n^*$, and $a_0 = 0$.

Taking ω_1 as the principal harmonic and $\delta\omega$ as the width of the spectral band, we extend Equation (4.30) to include the interactions of spectral components of the wave train with long-wavelength waves. Except for a constant multiplying the integral, the spectral amplitude equation is

$$
\begin{aligned}
\frac{\partial}{\partial x}\rho(\omega) &= -i\alpha\omega \int_{\Delta\omega}[\rho_{\omega_1+\xi}\rho_{\omega-\omega_1-\xi}e^{i\Delta_+ x} + \rho_{-\omega_1+\xi}\rho_{\omega+\omega_1+\xi}\epsilon^{i\Delta_- x}]d\xi, \\
\Delta_\pm &= k_\omega \mp k_{\omega_1+\xi} \pm k_{\omega_1+\xi\mp\omega} \approx k_\omega \mp k_{\omega_1} \pm \frac{dk}{d\omega}\big|_{\omega_1}\xi, \\
\pm k_{\omega_1} \pm \frac{dk}{d\omega}\big|_{\omega_1}(\xi-\omega) &= k_\omega - c_g^{-1}\omega = [c_{ph}^{-1}(0) - c_g^{-1}]\omega = \Delta_\omega
\end{aligned}
\tag{4.100}
$$

where c_g is the group velocity and c_{ph} is the phase velocity. Approximating,

$$
\begin{aligned}
\rho_{\omega_1+\xi} &\approx \rho_{\omega_1+\omega+\xi} \approx \rho_{\omega_1}, \\
\rho_{-\omega_1+\omega+\xi} &\approx \rho_{-\omega_1+\xi} \approx \rho_{-\omega_1}.
\end{aligned}
\tag{4.101}
$$

the equation for the amplitude is

$$
\frac{\partial}{\partial x}\rho_\omega \approx -i\alpha\omega|\rho_{\omega_1}|^2 e^{i\Delta_\omega x}\Delta\omega.
\tag{4.102}
$$

As was done in the discrete case, assume the frequency is sufficiently high so that $\rho_{\omega_1} \approx$ constant. Thus,

$$
\rho_\omega(x) \approx -\alpha\frac{\omega}{\Delta_\omega}|\rho_{\omega_1}|^2 e^{i\Delta_\omega x}\Delta\omega = -\frac{\alpha|\rho_{\omega_1}|^2 e^{i\Delta_\omega x}\Delta\omega}{[c_{ph}^{-1}(0) - c_g^{-1}(\omega_1)]}
\tag{4.103}
$$

The following equation for ρ_ω corresponds to such an interaction:

$$
\rho_\omega = -i\alpha\omega \int_{\Delta\omega}\rho_\xi\rho_{\omega-\xi}e^{-i\Delta_\xi x}d\xi \approx \frac{i\alpha^2\omega_1|\rho_{\omega_1}|^2\rho_\omega(\Delta\omega)^2}{[c_{ph}^{-1}(0) - c_g^{-1}(\omega_1)]}
\tag{4.104}
$$

where $|\omega - \omega_1| \leq \Delta_\omega$. Let $a_1 = \rho_\omega\Delta_\omega$ stand for the amplitude of the principal harmonic. Then, taking into account the term corresponding to the interactions with the

second harmonic, we obtain, instead of Equation (4.53),

$$\frac{\partial}{\partial x}a_1 = i\alpha^2\omega^2|a_1|^2\{\Delta^{-1} + \omega^{-1}[c_{ph}^{-1}(0) - c_g^{-1}(\omega_1)]^{-1}\}a_1. \qquad (4.105)$$

Its solution is $a_1 = a_1(0)e^{i\sigma x}$, corresponding to waves with "spatial" shift of $\sigma = -\alpha^2\omega^2|a_1|^2\{\Delta^{-1} + \omega^{-1}[c_{ph}^{-1}(0) - c_g^{-1}(\omega_1)]^{-1}\}$. Hence, in the high frequency the main difference between the discrete and the banded spectrum case is that the latter has an additional term in the nonlinear shift as compared with the case of Equation (4.53).

4.2   Remarks

The conditions for the stability of the surface system and of the full model, as of this writing, have not been analyzed in detail. However, it is possible to infer from the results of this chapter that the stability of the surface system does not depend on the frequency of the water waves since only weak resonance is possible, which in turn means that less energy is shifted from the lower modes to the higher ones the higher the frequency of the fundamental mode.

Evidence from numerical calculations and of our preliminary analytical work on the subject suggests that the stability is controlled by the size of α, by the possibility of a singularity in the denominators of the coefficients K_5 and K_6 by the right combination of parameters–see Figures 5.3 and 5.4– or by the choice of boundary conditions $\mathcal{A}_i$.

As shall be shown in Chapter 6, there are a number of ways in which refraction occurs in the modes. The model's assumptions places a restriction on the degree of y dependence of the solutions, and care must be exercised so as to not violate the assumption, especially when the domain involved is large. It may be possible, however, even when weak y dependence assumptions are not violated, for the solutions to lose their stability due to severe refraction. At a later stage in this study we shall pursue this issue with the hopes

of arriving at an estimate of when and how this form of instability occurs.

Chapter 5

Numerical Solution of the Model

This chapter is devoted to the details of the numerical solution of the full system and to a performance evaluation of the various computational schemes. As mentioned previously, the two disparate time scales effectively decouple the fluid and sediment problems, enabling us to solve the full model iteratively. The input to the model is comprised of an initial bottom configuration and the mode amplitudes at the line $x = 0$. The required dynamical parameters are the fundamental frequency, an estimate of the size of α and β, and the dimensions of the rectangular patch, $0 \geq x \geq M$, $0 \geq y \geq N$, of ocean on which the solution is to be computed.

Finite difference techniques were adopted in this study for a number of reasons, the primary one being that they are very well suited for the numerical solution of the hyperbolic equation of the type represented by the mass transport equation. Other reasons have to do with practicality: there are 3 equations to implement (the mass transport equation plus the two-component surface system), which are most conveniently solved on the same grid. In addition, synthetic boundary conditions on the lateral boundaries were found to be easily handled using finite difference techniques. In this study a uniform grid was found to be adequate for our purposes and hence, used exclusively.

5.1 Implementation of the Mass Transport Equation

The mass transport equation shall be implemented numerically using a Two-Step Lax-Wendroff scheme, which is second order accurate in time and space. Since this technique is very well established, we shall not report on such standard issues as consistency, convergence, and uniqueness. The reader is directed to Smith [66] for those details.

We shall define the following difference operators:

$$
\begin{aligned}
\Delta_q &= u(q_{j+1}) - u(q_j) &\quad \text{forward difference} \\
\nabla_q &= u(q_j) - u(q_{j-1}) &\quad \text{backward difference} \\
\delta_q &= u(q_{j+1/2}) - u(q_{j-1/2}) &\quad \text{central difference} \\
A_q &= u(q_{j+1}) + u(q_j) &\quad \text{forward average}
\end{aligned}
\tag{5.1}
$$

in the independent variable q, say. The physical space is given by $\mathcal{R}^2 \times T \equiv [0 \le x \le M, 0 \le y \le N] \times \{T \ge 0\}$. Define $\mathcal{R}^2_\Delta \times T_\Delta \equiv (x_r, y_s) \times T_n = (r\Delta x, s\Delta y) \times n\Delta T \in \mathcal{R}^2 \times T$. Furthermore, there are integers m and n, such that $M = m\Delta x$, $N = n\Delta y$.

Equation (3.50) is approximated by the following computational module:

$$
\begin{aligned}
h^{n+1/2}_{r+1/2} &= \frac{1}{4}(A_x + A_y)h + \frac{\Delta T}{2\Delta x}\Delta_x \mu + \frac{\Delta T}{2\Delta y}\Delta_y \nu \\
h^{n+1}_j &= h^n_j + \frac{\Delta T}{\Delta x}\delta_x T\mu + \frac{\Delta T}{\Delta y}\delta_y T\nu
\end{aligned}
\tag{5.2}
$$

on $\mathcal{R}^2_\Delta \times T_\Delta$. The module is illustrated in Figure 5.1 for one space dimension.

For the sake of clarity, the stability criteria shall be established in the shoreward direction only. Since $\mu_x = \mu_h h_x$ substituting in Equation (5.2) yields

$$
h^{n+1}_j = h^n_j - \xi_x[\frac{1}{2}(\Delta_x + \nabla_x)h - \frac{1}{2}\xi_x(\Delta_x - \nabla_x)h]
\tag{5.3}
$$

where $\xi_x = -\mu_h \Delta T/2\Delta x$. A local stability criteria may be established by replacing $h = \zeta^n \exp(ir\Delta x)$ in Equation (5.3), from which it follows that the growth factor is such
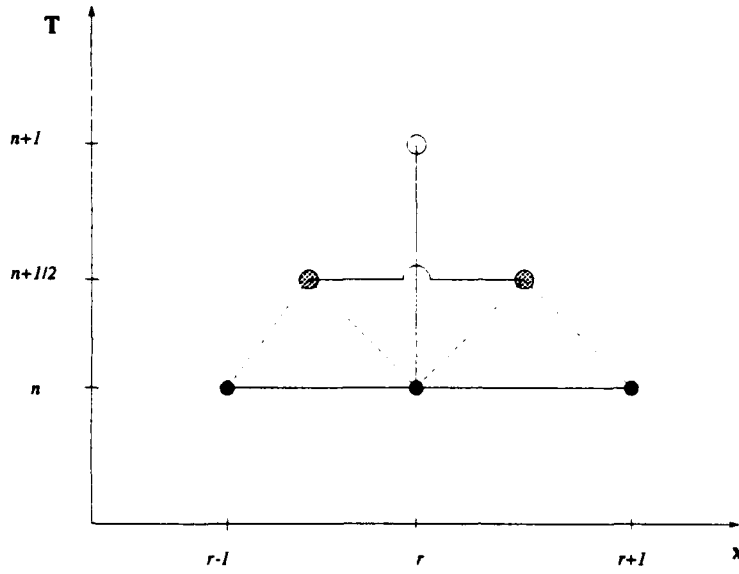
Figure 5.1: Computational module for the mass transport equation.

that

$$|\zeta|^2 = 1 - \xi_x(1 - \xi_x^2)(1 - \cos(r\Delta x))^2, \qquad (5.4)$$

and formal linearized stability shall result if $|\zeta| \leq 1$, which restricts $\xi_x^2 \leq 1$.

Using the same argument the stability criterion in the span-wise direction can be found, so that the stability of Equation (5.2) in two space dimensions requires that $\xi = -(\mu_h h_x \Delta T/2\Delta x, \nu_h h_y \Delta T/2\Delta y)$ be less than one in component form. Since

$$\mu_h = -\sum_{j=1}^{2} \frac{4\beta^2 k_j^3}{\mu_j \omega_j}(1 - \beta^2 h^2 k_j^2/2)H_j|a_j|^2$$

$$\nu_h = -\sum_{j=1}^{2} \frac{4\beta^2 k_j h}{\mu_j \omega_j}(1 - \beta^2 h^2 k_j^2/2)J_j[I_j R_{jy} - I_{jy}R_j], \qquad (5.5)$$

where I_j and R_j are respectively the real and imaginary parts of a_j. It is possible to show that the maximum value attained by either $|\mu_h|^2$, or $|\nu_h|^2$ is of the order of $16\beta^3|a_j|^4$.

Hence, for stability the grid size is determined by the constraint

$$\frac{\Delta T}{\Delta x} \leq \frac{1}{4}\beta^{3/2}|a_j|^2,\tag{5.6}$$

a result which sits well with the need to be economical about computer resources and that, as will be referred to subsequently, will not conflict with the stability criteria of the overall iterative scheme of the full model. Thus, in component form, for $\xi_x \leq 1$, and assuming $|a_j| \leq 1$ over the whole domain,

$$\frac{\Delta T}{\Delta x} \leq \beta^{-3}\alpha,\tag{5.7}$$

and for $\xi_y \leq 1$, the same argument leads to

$$\frac{\Delta T}{\Delta y} \leq \beta^{-3}.\tag{5.8}$$

Dissipation is known to occur except when $\xi_x^2 = 1$. The effect, however, can be quite small–fourth order in Δx–if the wavelengths are restricted to being much greater than the grid size [66].

5.2 The Surface Equations

5.2.1 Numerical Solution of the Two-dimensional Surface System

The numerical solution of the two-dimensional surface system

$$\begin{aligned}
a_{1x} &= -iK_3 f(x)a_1 - iK_5 e^{-i\delta x}a_1^* a_2 \\
a_{2x} &= -iK_4 f(x)a_2 - iK_6 e^{+i\delta x}a_1^2 \\
a_1(x=0) &= \mathcal{A}_1 \\
a_2(x=0) &= \mathcal{A}_2,
\end{aligned}\tag{5.9}$$

where $\mathcal{A}_1$ and $\mathcal{A}_2$ are constants, shall be used later in the evaluation of the imple-

mentation of the three-dimensional surface system. A standard fourth-order explicit Runge-Kutta scheme

$$\phi_{r+1} = \phi_r + \frac{1}{6}(\mathbf{P}_1 + 2\mathbf{P}_2 + 2\mathbf{P}_3 + \mathbf{P}_4)$$

$$\mathbf{P}_1 = \Delta x \mathbf{F}(\phi_r, x_r)$$

$$\mathbf{P}_2 = \Delta x \mathbf{F}(\phi_r + \frac{1}{2}\mathbf{P}_1, x_r + \frac{1}{2}\Delta x)$$

$$\mathbf{P}_3 = \Delta x \mathbf{F}(\phi_r + \frac{1}{2}\mathbf{P}_2, x_r + \frac{1}{2}\Delta x)$$

$$\mathbf{P}_4 = \Delta x \mathbf{F}(\phi_r + \mathbf{P}_3, x_r + \Delta x), \qquad (5.10)$$

where $\mathbf{F}$ is the right hand side of Equation (5.9), and the vector $\phi_r \equiv [a_1(x_r), a_2(x_r)]$, was used to numerically solve this system. For details on the applicability of such a scheme to the solution of Equation (5.9) we refer the reader to Boczar-Karakiewicz, Bona, and Cohen [1].

5.2.2 The Three-Dimensional Model

For the surface equations, we rewrite Equation (4.2)

$$a_{1x} - iK_1 a_{1yy} + iK_3 f(x, y) a_1 = -iK_5 e^{-i\delta x} a_1^* a_2$$

$$a_{2x} - iK_2 a_{2yy} + iK_4 f(x, y) a_2 = -iK_6 e^{+i\delta x} a_1^2$$

$$a_1(x = 0, y) = \mathcal{A}_1(y)$$

$$a_2(x = 0, y) = \mathcal{A}_2(y)$$

$$a_{1y}(x, y = 0) = 0 \qquad (5.11)$$

$$a_{1y}(x, y = 0) = 0$$

$$a_{2y}(x, y = M) = 0$$

$$a_{2y}(x, y = M) = 0$$

to separate the linear and nonlinear parts. The first two boundary conditions are inherent in the physics of the problem. The remaining boundary conditions are artificial.

These Neumann boundary conditions, combined with a computational procedure that will be explained presently, ensures that the overall structure of the solutions shall remain negligibly affected by the choice of lateral boundary conditions. We call this technique the "zero-flux procedure".

In order to explain why this procedure is needed, let us spell out what sort of problem we are faced with: Since we need to compute a solution over a finite domain, care must be exercised in imposing boundary conditions on the lateral sides so that we avoid the introduction of structure in the solution that is strictly mathematical rather than physical[1] in nature. To avoid this situation we use appropriate boundary conditions along the lateral sides, and in addition, place restrictions on the initial bottom configuration and the boundary condition at $x = 0$ so that we can compute an oceanic event on a swath of what amounts to be an effectively unbounded domain. We have found that this zero flux procedure is superior to other synthetic boundary conditions in minimizing unwanted structure in the solutions.

The Neumann boundary conditions make the problem well-posed, however, by themselves, would introduce a great deal of structure. Physically, these boundary conditions correspond to placing hard barriers on the lateral sides of the domain. A posteriori we know that the solution to the model is two dimensional if neither the bottom nor the boundary condition at $x = 0$ has y dependence. In such a case the zero flux condition on the lateral sides has no effect on the solution over any part of the domain, i.e., it does not add y dependence to the solution. We perform the calculation of the system over a computational domain which we divide into three regions. The large central region, flanked by two sufficiently wide lateral strips, is one in which y variation in the initial

---

[1]A possible way to compute a solution of the problem over an effectively unbounded domain over a finite grid is to impose periodic boundary conditions. However, periodicity imposes unwanted symmetries on the structure of the computed solutions.

bottom or in the boundary condition at $x = 0$ is possible. In the lateral strips no y dependence in the above mentioned quantities is permitted. The solution in these lateral strips is discarded. The initial bottom and the boundary condition at $x = 0$ are connected smoothly in all three regions so that a minimal amount of structure is introduced in the solutions. The size of the lateral strips is determined by what amounts to an educated guess.

An efficient, simple, and sufficiently accurate method to implement the above non-stiff, "locally" nonlinear system numerically is now the focus of our attention. Several issues have motivated the particular choice of scheme: (1) The accuracy requirements are not very sophisticated, since we wish to explore a phenomenological question rather than achieve engineering accuracy; (2) a uniform grid is preferred over a variable one, so that both the surface and mass transport equations may be easily computed on the same grid; (3) the computational domain is fairly large for the sort of problem presented in this study. The method presented here has, among its best features, low storage requirements and high speed as measured by its low operation count; it is easy to implement on conventional hardware using recursive data structures, and to a certain extent, parallelizable on vector machines.

Define the following vectors,[2] with all $K's$ real:

$$\mathbf{k} = i[K_1, K_2]^T$$

$$\mathbf{k_f} = if(x, y)[K_3, K_4]^T$$

$$\phi = [a_1(x, y), a_2(x, y)]^T \in \mathcal{C}^2 \qquad (5.12)$$

with $(x, y) \in \mathcal{R}^2_\Delta$, so that the system, Equation (5.11), is now recast on the discrete grid

---

[2]The superscript T means "transpose" in what follows.

$\mathcal{R}^2_\Delta$ as

$$[\partial_x - k\partial_{yy} + k_f]\varphi = b(x, y, \phi), \qquad (5.13)$$

with the linear part on the left hand side and the nonlinear terms on the right of the equals sign, plus boundary conditions,

$$\phi_y = 0 \quad \text{on } y=0, y=N$$
$$\phi = \phi_0 \quad \text{on } x=0, \qquad (5.14)$$

The term $b(x, \phi)$ represents the nonlinear terms. Succinctly, the above equation may be written as

$$\mathcal{L}\phi = b \qquad (5.15)$$

where $\mathcal{L}$ is the linear operator. Let L be a suitable discretization of such linear operator. Suppose the value of the vector ϕ at level r for all s is known. Making use of fixed point methods the value of the vector at level $r + 1$ may be found. Computationally, the calculation is performed in two steps: let l be the index of the iteration and let $\overline{\phi}$ be an intermediate result. Then the following computational scheme is proposed:

$$L\overline{\phi} = b(x, y, \phi^l)$$
$$L\phi^{l+1} = b(x, y, \overline{\phi}). \qquad (5.16)$$

Formally, Equation (5.16) is equivalent to

$$L\phi^{l+1} = \check{b}(x, y, \phi^l). \qquad (5.17)$$

To start the iteration, the value of the field variables at the rth level in x is used, i.e., $\phi^0 = \phi_r$. The condition for convergence of Equation (5.16) is found by appealing to the fixed point theorem.

For the purpose of determining the convergence criteria, define $\mathcal{C}$, a region in $\mathcal{C}^4$, the generalization of the four dimensional real space to complex variables. Let Φ and $\mathbf{h} \in \mathcal{C}$ be two vectors in that space. Hence, the derivative of $\mathbf{A}$ with respect to Φ is defined as

$$\mathbf{A}_\Phi \equiv \mathbf{J}(\Phi) = \frac{\partial A_i}{\partial \Phi_j}. \tag{5.18}$$

If the second derivative is continuous for all $\Phi \in \mathcal{C}$, then it satisfies

$$\| \mathbf{A}_{\Phi\Phi}(\Phi, \mathbf{h}, \mathbf{h}) \| \leq R \| \mathbf{h} \|^2 \tag{5.19}$$

for all Φ.

Furthermore, let $\| \cdot \|_p$, with $p = 1, 2, \infty$, represent the induced norms

$$L_1 = \max_{1 \leq j \leq n} \{\textstyle\sum_{i=1}^n |A_{ij}|\} \qquad L_2 = \{\textstyle\sum_{i=1}^n \sum_{j=1}^n A_{ij} A_{ij}^\star\}^{1/2}$$
$$L_\infty = \max_{1 \leq i \leq n} \{\textstyle\sum_{j=1}^n |A_{ij}|\}. \tag{5.20}$$

Finally, define a super-system on $\mathcal{R}_\Delta^2$ as

$$[\partial_x - \mathbf{K}\partial_{yy} + \mathbf{K_f}]\Phi \quad = \quad \mathbf{B}(x, y, \Phi) \tag{5.21}$$

plus boundary conditions,

$$\Phi_y = 0 \quad \text{on y=0, y=N}$$
$$\Phi = \Phi_0 \quad \text{on x=0} \tag{5.22}$$

composed of (5.11) and its complex conjugate, with

$$\mathbf{K} \quad = \quad [\mathbf{k}, \mathbf{k}^\star]^T \in \mathcal{C}$$
$$\mathbf{K_f}(x, y) \quad = \quad [\mathbf{k_f}, \mathbf{k_f}^\star]^T$$
$$\Phi \quad = \quad [a_1(x, y), a_2(x, y), a_1^\star(x, y), a_2^\star(x, y)]^T \in \mathcal{C}. \tag{5.23}$$

Let $\mathbf{L}$ be the resulting discrete operator of the super-system, composed of L and its complex conjugate. Choosing L non-singular (hence $\mathbf{L}$ is non-singular), and multiplying

both sides of (5.21) by $\mathbf{L}^{-1}$.

$$\Phi^{l+1} = \mathbf{A}(x, y, \Phi^l). \tag{5.24}$$

Define the iteration discrepancy as

$$\| \delta\Phi^{l+1} \|_p \equiv \| \Phi^{l+1} - \Phi^l \|_p . \tag{5.25}$$

Appealing to the Fixed Point Theorem, it can be surmised that

$$
\begin{aligned}
\| \delta\Phi^{l+1} \|_p &= \| \mathbf{A}(\Phi^l) - \mathbf{A}(\Phi^{l-1}) \|_p \\
&\approx \| \mathbf{J}(\Phi^{l-1})\delta\Phi^l \|_p \leq \| \mathbf{J}(\Phi^{l-1}) \|_p \| \delta\Phi^l \|_p \\
&\leq \| \mathbf{J}(\Phi^{l-1}) \|_p \| \mathbf{J}(\Phi^{l-2}) \|_p \| \delta\Phi^l \|_p \leq \cdots \\
&\leq \prod_{l=0}^{k-1} \| \mathbf{J}(\Phi^l) \|_p \| \delta\Phi^0 \|_p,
\end{aligned}
\tag{5.26}
$$

provided

$$0 < \| \mathbf{J}(\Phi^l) \|_p < 1. \tag{5.27}$$

Equation (5.27) is in fact the convergence criteria for the iteration process.

To establish an estimate of the rate of convergence, let $r > 0$ be given such that the set of vectors $\mathcal{S} = \{\Phi : \| \Phi - s \|_p < r\}$ contains a fixed point s of $\mathbf{A}(s)$, i.e.,

$$s = \lim_{l \to \infty} \Phi^l = \lim_{l \to \infty} \mathbf{A}(\Phi^l) = \mathbf{A}(s). \tag{5.28}$$

Further, let $\mathcal{S} \subseteq \mathcal{C}$, $\mathbf{J}(s)$ continuous on $\mathcal{S}$ and $\| \mathbf{J}(s) \|_p < 1$. Then there exists an $\varepsilon > 0$ such that the fixed point iteration is convergent whenever $\| \Phi^0 - s \|_p < \varepsilon$. Define $\| e^{l+1} \|_p$, the measure of difference between the $(l+1)^{th}$ iterate and the root. Hence

$$\| e^{l+1} \|_p = \| \Phi^{l+1} - s \| \approx \| \mathbf{J}(s)e^l + \mathbf{A}''(\zeta; e^l, e^l) \|_p \leq \| \mathbf{J}(s)e^l \| + R \| e^l \|^2 . \tag{5.29}$$

Quadratic convergence is possible if $\mathbf{J(s)} = 0$.

$$\lim_{l \to \infty} \frac{\| \, \mathbf{e}^{l+1} \, \|_p}{\| \, \mathbf{e}^l \, \|_p} \leq R. \tag{5.30}$$

For the problem in question, however, the best rate of convergence will be linear since $\mathbf{J(s)} \neq 0$:

$$\lim_{l \to \infty} \frac{\| \, \mathbf{e}^{l+1} \, \|_v}{\| \, \mathbf{e}^l \, \|_p} \leq \| \, \mathbf{J(s)} \, \|_p . \tag{5.31}$$

A measure of resources required in the computation is the size of the resulting matrix problem. The slightly better flexibility in the choice of discretization for the linear operator L is the key advantage of this method over others. The most economical discretizations are those that lead to a tri-diagonal or quinta-diagonal matrix. In our study

$$L = (\frac{3}{2\Delta x}\Delta_x - \frac{1}{2\Delta x}\nabla_x)\phi_r^s - (\frac{k}{\Delta y^2}\delta_y^2 + k_{f_{r+1}^s})\phi_{r+1}^s, \tag{5.32}$$

which leads to an $n \times n$ tri-diagonal matrix. Its computational module is illustrated in Figure 5.2, and is commonly known as the Douglas scheme. L has eigenvalues
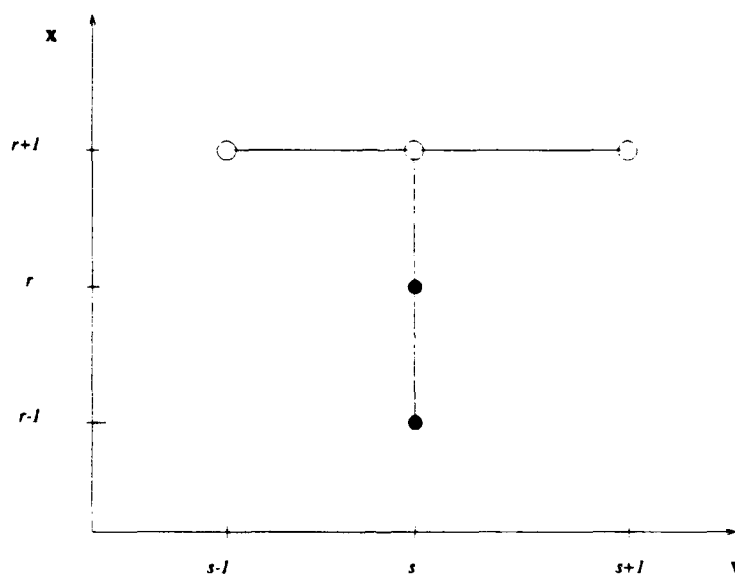

Figure 5.2: Computational module for the linear operator of the surface system.

$$\lambda_s = -(3 + 2\rho + 2\Delta x \mathbf{k_f}) + 2\rho \cos[\tfrac{s\pi}{n+1}] \qquad s = 1, \cdots n , \qquad (5.33)$$

and the eigenfunctions are given by

$$\{\sin \frac{s\pi}{n+1}, \sin \frac{2s\pi}{n+1}, \cdots, \sin \frac{s\pi}{n+1}\}^T \; s = 1, \cdots, n. \qquad (5.34)$$

Furthermore, the operator L is diagonally dominant, since

$$\sum_{\substack{j \neq i}}^{n+1} |L_{ij}| \leq |L_{ii}| \qquad i = 1, \cdots n \qquad (5.35)$$

the L_{ij}'s being the entries of the matrix L, and non-singular since

$$|L_{ii}| > |L_{ii+1}| > 0 \qquad\qquad i = 1, \cdots n - 1$$

$$|L_{ii}| \geq |L_{ii+1}| + |L_{ii-1}| \quad L_{ii+1}L_{ii-1} \neq 0 \quad i = 2, \cdots n - 1$$

$$|L_{ii}| > |L_{ii-1}| \qquad\qquad i = 2, \cdots n. \qquad (5.36)$$

If $\phi = \xi^r e^{i\theta}$, where $\theta = \alpha \Delta y s$, and $\rho = 2\frac{\Delta x}{\Delta y^2}\mathbf{k}$, upon substituting these quantities in L the magnification factor is

$$\xi = \frac{1}{2\rho(1 - \cos\theta) + 2\Delta x \mathbf{k_f} + 3}\{2 \pm \sqrt{1 - 2\rho(1 - \cos\theta) - 2\Delta x \mathbf{k_f}}\}, \qquad (5.37)$$

from which it is clear that $|\xi| \leq 1$. Thus the linear operator is unconditionally stable.

An estimate of the accuracy of the discretization of the linear operator, and a check on its consistency with the continuous operator on the grid, is given by

$$(L - \mathcal{L})\phi = \frac{\Delta x^2}{2}\phi_{xx} + \mathbf{k}\frac{\Delta y^2}{12}\phi_{yyyy} + \cdots, \qquad (5.38)$$

where $\mathcal{L}$ is the continuous linear operator. Equation (5.38) implies that the scheme is $O(\Delta x^2 + \Delta y^2)$ accurate.

This order of accuracy is an upper-bound on the accuracy of the overall scheme, hence attempting to reduce the error $\| \mathbf{e}^l \|$ much below this is pointless. Since the real root is

not known *a priori*, the iteration procedure is carried out until we are safely below the above-quoted error, but not much beyond that. This, in effect, is the criteria used in the code for stopping the root-finding iteration procedure.

Consistency of the discretization is readily established by comparing the continuous problem with its discretization in the limit as the grid size gets smaller. It may be shown that the discretization approaches the continuous operator on the grid uniformly.

Since the Douglas scheme is inapplicable at $r = 0$, a standard Backwards Euler scheme,

$$\frac{1}{\Delta x}\Delta_x \phi_r - \frac{1}{\Delta y^2}k\delta^2 \phi_{r+1} + A_x(k_f\phi)_{r+1}, \tag{5.39}$$

is used to discretize L for the first step in x, which can be shown to be unconditionally stable as well.

Having made a choice on the particular form of the operator L, the condition that $\| \mathbf{J}(\mathbf{x}) \|_p < 1$ for the surface system, must be determined explicitly, so that convergence is established for the sand ridge problem. To estimate the size of $\mathbf{J}(\mathbf{x})$ we make use of the super-system, Equation (5.24),

$$\Phi^{l+1} = \mathbf{L}^{-1}\mathbf{B}(\Phi^l) \tag{5.40}$$

$$\Phi^l = \mathbf{L}^{-1}\mathbf{B}(\Phi^{l-1}) \tag{5.41}$$

$$\Phi^{l-1} = \text{etc.} \tag{5.42}$$

Thus,

$$\delta\Phi^{l+1} \approx \mathbf{J}(\Phi^l)\delta\Phi^l \tag{5.43}$$

$$\delta\Phi^l \approx \mathbf{J}(\Phi^{l-1})\delta\Phi^{l-1} \tag{5.44}$$

$$\text{etc.} \tag{5.45}$$

with

$$\mathbf{J} = \mathbf{L}^{-1}\mathbf{B}'(\mathbf{\Phi}), \tag{5.46}$$

where

$$\mathbf{B}'(\mathbf{\Phi}^l) = \begin{pmatrix} 0 & -iK_5 e^{-i\delta x_{r+1}} a_1^{*l} & -iK_5 e^{-i\delta x_{r+1}} a_2^l & 0 \\ -i2K_6 e^{-i\delta x_{r+1}} a_1^l & 0 & 0 & 0 \\ iK_5 e^{+i\delta x_{r+1}} a_2^{l*} & 0 & 0 & iK_5 e^{+i\delta x_{r+1}} a_1^l \\ 0 & 0 & i2K_6 e^{+i\delta x_{r+1}} a_1^{l*} & 0 \end{pmatrix}. \tag{5.47}$$

for the lth iterate. In Equation (5.47), it is understood that the $a's$ are only defined on the grid.

From Equation (5.46), $\| \mathbf{J} \|_p < 1$ if the size of $\mathbf{L}$ is greater than the size of $\mathbf{B}'$. In the L^2 norm, the convergence condition is

$$\| \mathbf{J} \|_2 = \| \mathbf{L}^{-1}\mathbf{B}' \|_2 \leq \| \mathbf{L}^{-1} \|_2 \| \mathbf{B}' \|_2 \leq 1, \tag{5.48}$$

but

$$\| \mathbf{L}^{-1} \|_2 \leq \| \mathbf{I} \|_2 / \| \mathbf{L} \|_2 = 2/ \| \mathbf{L} \|_2 . \tag{5.49}$$

Replacing (5.49) into (5.48) yields

$$\| \mathbf{J} \|_2 \leq 2 \| \mathbf{B}' \|_2 / \| \mathbf{L} \|_2 \leq 1. \tag{5.50}$$

Working out the above inequality gives the condition for convergence in our particular case:

$$2\sqrt{(K_5^2 + 4K_6^2)|a_1|^2 + K_5^2|a_2|^2}/ \| \mathbf{L} \|_2 \leq 1. \tag{5.51}$$

Since $\mathbf{L}\mathbf{L}^\dagger = \mathbf{L}^\dagger\mathbf{L}$, where $\mathbf{L}^\dagger$ is the Hermitian matrix of $\mathbf{L}$, then

$$\| \mathbf{L} \|_2 = \sqrt{\rho(\mathbf{L}\mathbf{L}^\dagger)} = \sqrt{4max_{s=1,n}|\lambda_s|}, \tag{5.52}$$

or using Eq.(5.33),

$$\sqrt{(K_5^2 + 4K_6^2)|a_1|^2 + K_5^2|a_2|^2}/(3 + 4\rho + 2\Delta x k_f) < 1. \qquad (5.53)$$

where the L_∞ in y is used to estimate the size of the vectors, i.e., $a_i = \max_{1 \le s \le n} a_i^s$, i=1,2. Hence, Equation (5.53) gives constraints on ρ, Δx, and a_i, to be satisfied in order to guarrantee convergence in the solution of our problem. Another constraint we impose in the numerical implementation is to restrict Δx to be less than $2\pi/\delta$, so as to minimize the phase error. In Figure 5.3 and 5.4 the parametric plots of K_5 and K_6 are shown, and are included to complete the picture of the relevant size of all the quantities involved in Equation (5.53).
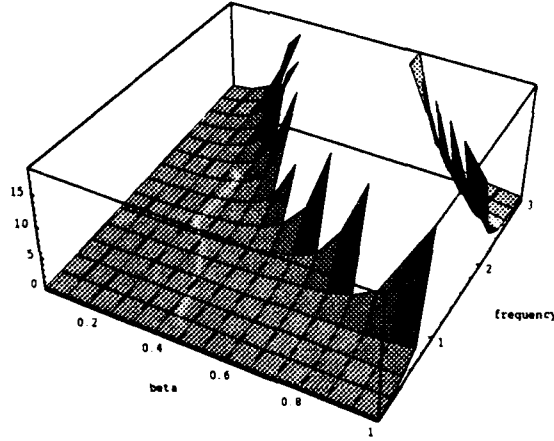

Figure 5.3: Plot of K_5/α versus the fundamental frequency ω_1, and β.

It must be noted that owing to the nature of the nonlinearity of our particular problem, we had to rely on the super-system to arrive at a convergence criteria, but we do not actually use it for the computation of the field variables. Note also that although
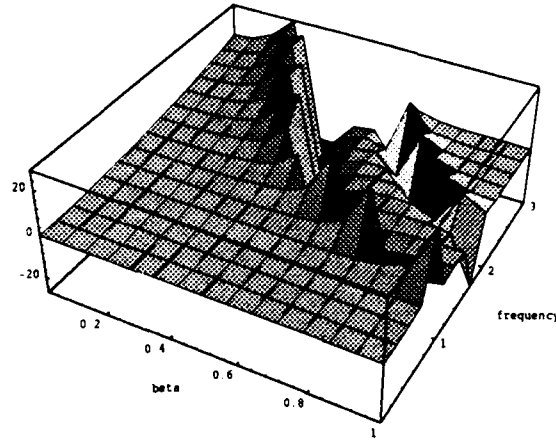
Figure 5.4: Plot of K_6/α versus the fundamental frequency ω_1, and β.

inverse matrices appear establishing the estimates of convergence, they are not actually required in the computation of the field variables themselves.

5.3 Performance Evaluation of the Numerical Schemes

5.3.1 Evaluation of the Mass Transport Equation Scheme

For the Lax-Wendroff Scheme, we ran a few test runs in order to confirm qualitatively the scheme's stability, consistency and accuracy, checking for agreement with the well established theoretical results. Of more concern to us was the issue of damping and of phase drift. In order to quantify the scheme's dissipation and drift we used a model problem for which an exact solution is known.

The model problem used was

$$h_T + khh_x = 0, \ x \in \mathcal{R}^1, T > 0 \tag{5.54}$$

with initial condition

$$h(x,0) = \begin{cases} 1 & x < 0 \\ 1 + \varepsilon x & 0 \le x \le l \\ 1 + \varepsilon l & x > l \end{cases} \tag{5.55}$$

in which $0 < k < 1$, and $\varepsilon < 1$. The exact solution of Equations (5.54) and (5.55) is

$$h(x,T) = \begin{cases} 1 & x < kT \\ 1 + \varepsilon \frac{x - kT}{1 + \varepsilon kT} & kT \le x \le l + k(1 + \varepsilon l)T \\ 1 + \varepsilon l & \text{otherwise.} \end{cases} \tag{5.56}$$

We tried different values of k – it scales the time step–, but we report our results for $k = 0.1$, and for such a case convergence is possible if $h\Delta T/\Delta x < 10$ in the time interval 0 to T. Since Equation (5.54) conserves a quantity proportional to h^p, we compared the computed value h_Δ against the theoretical value h as a function of $a \equiv k\Delta T/\Delta x$ and as a function of time T to get an idea of the scheme's dissipation. Specifically, we monitored the constant of motion

$$c(T,a) = \sum_{r=0}^{M/\Delta x} h_\Delta^2(T, r\Delta x) r\Delta x + \frac{2}{3}kT[h_\Delta^3(T,M) - h_\Delta^3(T,0)], \tag{5.57}$$

where M is a very large value in x_r. For an estimation of the phase drift, we computed

$$e^2(a,T) = \sum_r |h_\Delta(T,x_r) - h(T,x_r)|^2 / \sum_r |h(T,x_r)|^2. \tag{5.58}$$

Figure 5.5 and 5.6 show parametric plots of c and e^2 respectively.

5.3.2 Performance of the Runge-Kutta Scheme

The accuracy and dissipation of the explicit fourth-order Runge-Kutta was investigated. The domain was 128 units in extent, or roughly 10 interaction lengths. To measure the dissipation, we monitored the energy, given by Equation (4.62). This quantity was conserved by all trials to within 2% for all reasonable grid sizes.
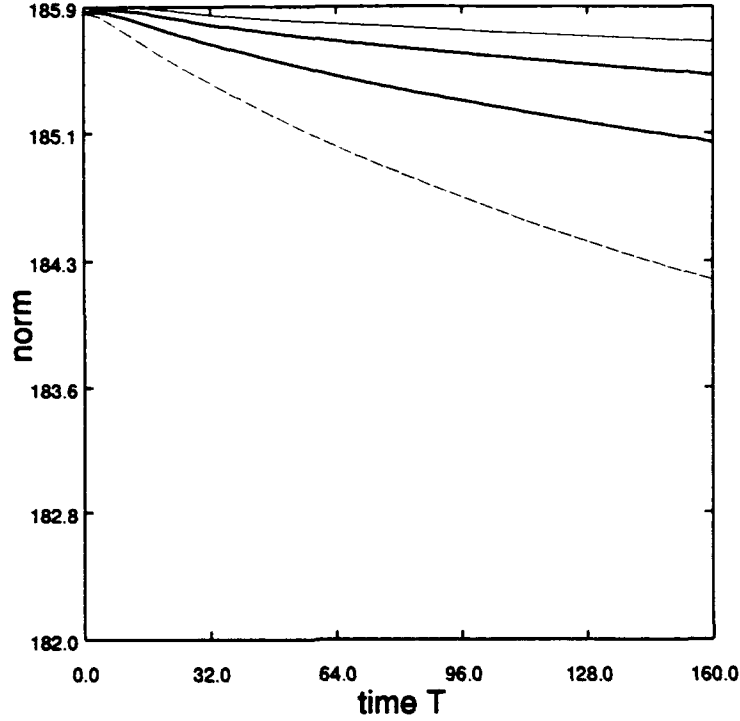
Figure 5.5: Dissipation as a function of a and T with $k = 0.1$ for the Lax-Wendroff Scheme. From top to bottom, $a = 0.4, 0.2, 0.1, 0.05$ respectively.

To estimate the accuracy and error of the scheme we compared the outcome of the numerical solution to the exact solution (4.72) using the following measures:

$$
\begin{aligned}
l_\infty &= \frac{\max\{\sum_r |\chi(r\Delta x) - \chi'(x_r)|\}}{\max\{\sum_r |\chi'(r\Delta x)|\}} \\
l_1 &= \frac{\sum_r |\chi(r\Delta x) - \chi'(x_r)|}{\sum_r |\chi'(r\Delta x)|} \\
l_2 &= \frac{[\sum_r |\chi(r\Delta x) - \chi'(x_r)|\}^2]^{1/2}}{[\sum_r |\chi'(r\Delta x)|^2]^{1/2}},
\end{aligned}
\tag{5.59}
$$

where χ is the calculated value of a_i, and χ' the exact value at the grid location. The exact solution χ', was computed using the algorithm given in [67], p189. The error as a function of grid size is plotted in Figure 5.7, from which one can conclude that the
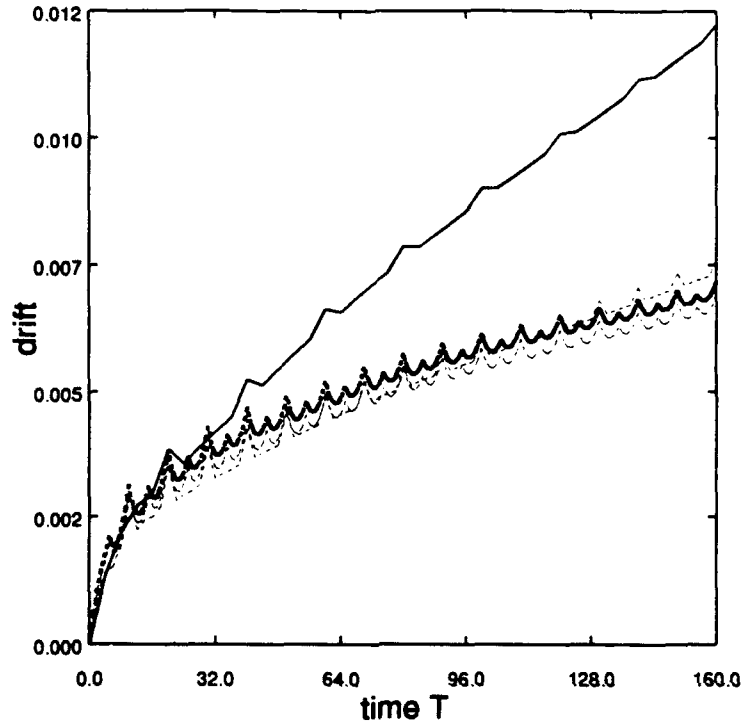
Figure 5.6: Phase drift for the Lax-Wendroff scheme as a function of a and T with $k = 0.1$. From top to bottom, $a = 0.4, 0.2, 0.1, 0.05$ respectively.

scheme is in fact fourth order accurate and consistent, i.e. the error drops more or less by a factor of 2^4 every time the grid size is halved. For the accuracy and dissipation trials $\mathcal{A}_1 = 0.5$, $\mathcal{A}_2 = 0$, in Equation (5.9), a flat bottom and parameters $\alpha = 0.3$, $\beta = 0.1$, $\omega_1 = 0.5$, were used. Roughly, 10 interaction lengths was the extent of the domain.

5.3.3 Fixed Point Method Performance and Evaluation

Since we do not have an exact solution to the three-dimensional system we sought to discern the accuracy of the Fixed Point Method (FPM) using local analysis. Let Δ be the size in x or y of each grid element–as mentioned previously, the grid size is uniform in the domain. A comparison of the computed solution at a particular point, using Δ.
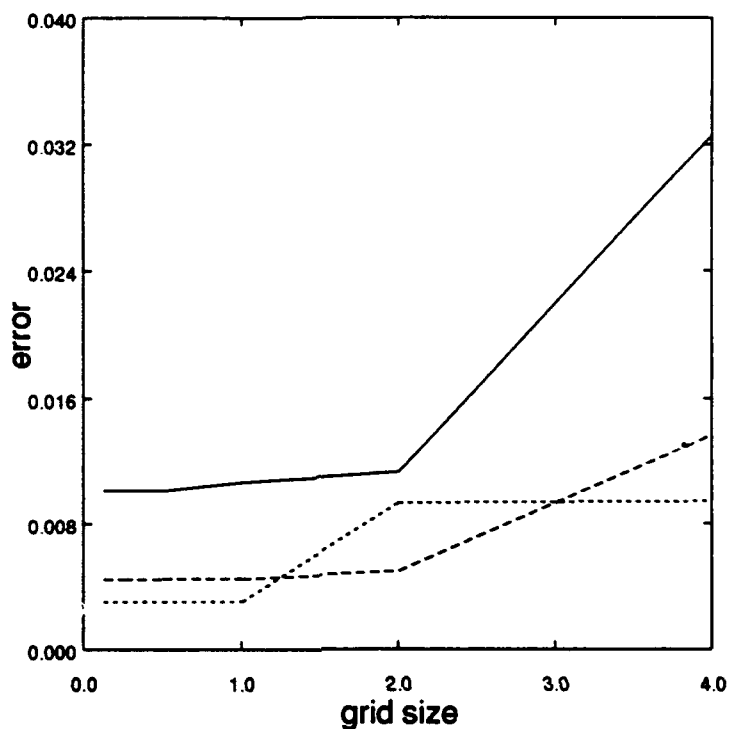
Figure 5.7: Error as a function of grid size for the Runge-Kutta method. l_1: $\cdots\cdots\cdots$ l_2: $-\ -\ -\ -\ -\ -$, l_∞: $\rule{2cm}{0.4pt}$.

and a solution with grid size $\Delta/2$ yields

$$|\chi_\Delta - \chi_{\Delta/2}| \equiv k_1 = CO'[(\Delta/2)^p].$$

(5.60)

Halving the grid size again

$$|\chi_{\Delta/2} - \chi_{\Delta/4}| \equiv k_2 = CO[(\Delta/4)^p].$$

(5.61)

Thus, using Equation (5.60) and Equation (5.61) we can solve for p to get an estimate of the order of accuracy of the scheme:

$$p = \frac{\log k_1 - \log k_2}{\log 2}.$$

(5.62)

Using the same parameters and boundary conditions as those used in connection with the Runge-Kutta scheme, and a domain with length of 128 and span of 32, we found that the Fixed Point Method ... ids an average value of $p = 1.8$, with a standard deviation of 0.5. Values of both field quantities were used, and they were taken from various points in the domain.

We did not perform a systematic study of the convergence of the method. We observed, however, that the computed values tended to converge as the grid size was refined. Since comparisons of the computed solutions with an exact expression for the three-dimensional case were not possible, we compared the cross-sectional values of an effectively two-dimensional solution computed using FPM along the whole length in x and midway in the span-wise direction y, with a solution computed using the Runge-Kutta Method with a very fine grid spacing. A measure of the error is given by the

$$
\begin{aligned}
l_\infty(\Delta x, \Delta y) &= \frac{\max\{\sum_r |\chi(r\Delta x, mid) - \chi'(x_r)|\}}{\max\{\sum_r |\chi'(r\Delta x)|\}} \\
l_1(\Delta x, \Delta y) &= \frac{\sum_r |\chi(r\Delta x, mid) - \chi'(x_r)|}{\sum_r |\chi'(r\Delta x)|} \\
l_2(\Delta x, \Delta y) &= \frac{[\sum_r |\chi(r\Delta x, mid) - \chi'(x_r)|\}^2]^{1/2}}{[\sum_r |\chi'(r\Delta x)|^2]^{1/2}}
\end{aligned}
\tag{5.63}
$$

norms, where χ represents the solution obtained using FPM and χ' the solution computed with the Runge-Kutta scheme.

For the case $\Delta x = \Delta y$, the result is shown in Figure 5.8. The same result is obtained when we fix $\Delta y = 0.25$, and we vary Δx. On the other hand, when $\Delta x = 0.25$ is fixed and Δy is varied, very little sensitivity in the norms is obtained. In this last case, the $l_1 \approx 4.4 \times 10^{-3}$, $l_1 \approx 4.4 \times 10^{-3}$, and $l_1 \approx 4.4 \times 10^{-3}$ for all sizes of the grid in the y direction that we tried [3].

The rate at which the iteration converges in FPM as a function of the grid size was

---

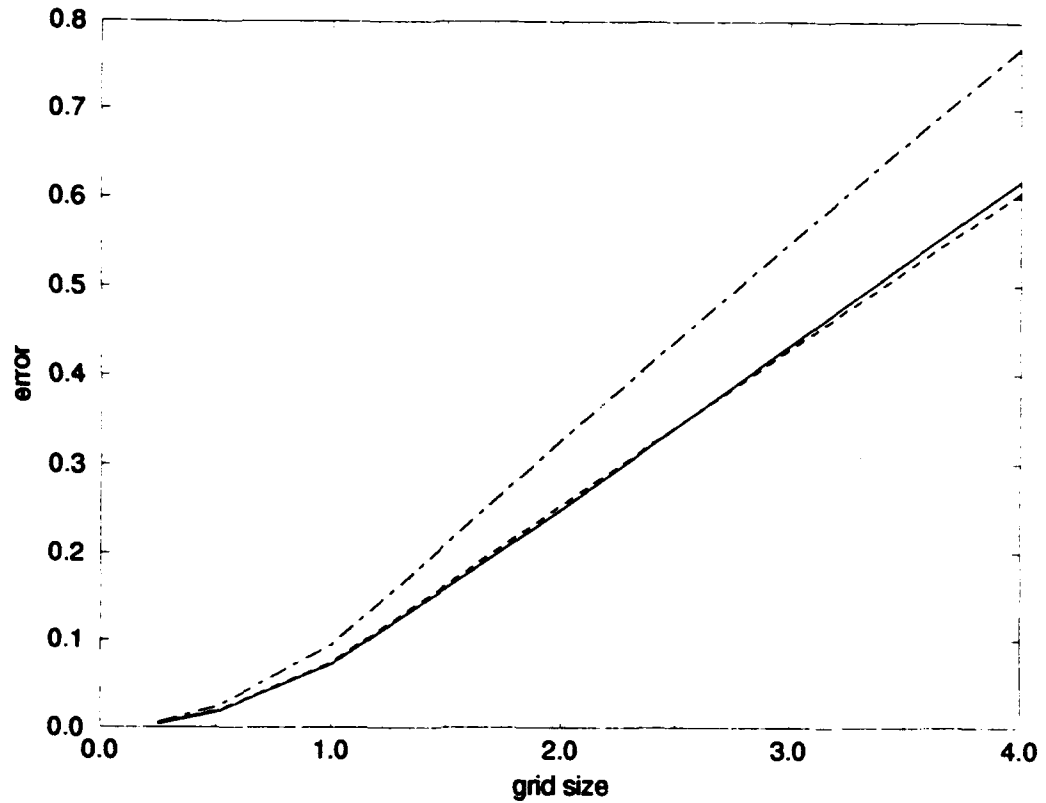[3] Note that there is no y dependence in the solution for this particular trial.

Figure 5.8: Error as a function of grid size, with $\Delta x = \Delta y$. l_∞:—·——·——·—, l_1: ·········, l_2:————— .

also investigated. With $\alpha = 0.3$, $\beta = 0.08$, $\omega_1 = 0.5$, and boundary conditions $\mathcal{A}_1 = 0.5$ and $\mathcal{A}_2 = 0.1$, and a flat bed, we monitored the iteration discrepancy at a particular value of x in a fairly large domain. As expected, we found that the number of iterations required to meet a certain iteration tolerance decreases as the grid was refined. Figure 5.9 shows how the quantity

$$\log_{10}[\max\{\sum_{s=0}^{n} |\phi^{l+1}(x, s\Delta y) - \phi^{l}(x, s\Delta y)|\}] \tag{5.64}$$

drops after each iteration l for a number of different grid sizes. It is evident from the graphs that a finite and small number of iterations are required to reach adequate error tolerances using reasonably-sized grids.

We examined the iteration convergence at the first step in x as well. Recall that for the first step a Backwards Euler scheme was used to discretize the linear operator instead of the Douglas scheme. We found that the number of iterations was roughly double the number required elsewhere in the domain, where the Douglas scheme is used.
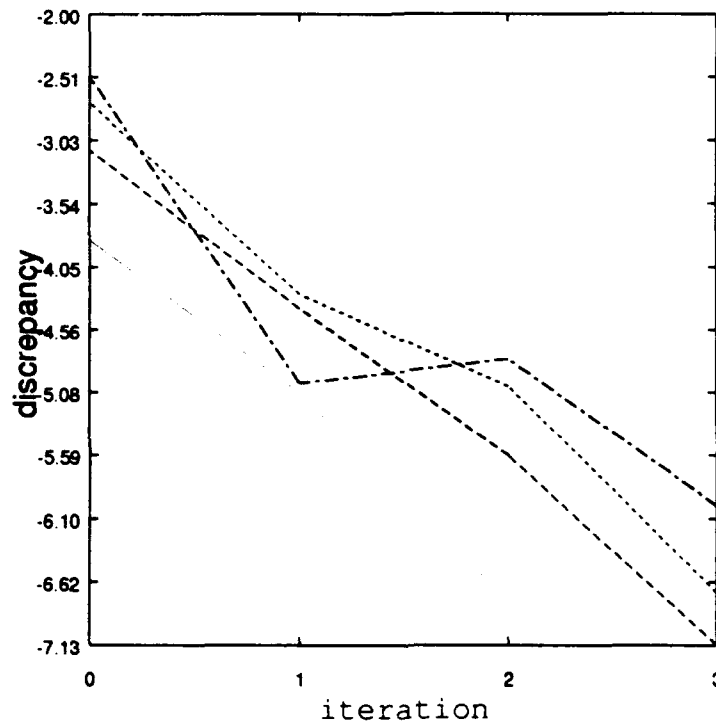

Figure 5.9: Iteration discrepancy as a function of grid spacing. The number of iterations drops as $\Delta = 4, 2, 1, 0.5$ respectively.

Before we examine the model's speed and storage requirements, we shall present an overview of the implementation of the surface equations using Newton's Iterative Method, the point being that a comparison of the standard approach with FPM enables us to make specific claims regarding the resource economy of the Fixed Point Method.

In the most straightforward application of Newton's Method we either use the super-system, or separate the regular system into real and imaginary parts. We shall opt for

the second alternative. Let

$$
\begin{aligned}
a_1 &= u + iv \\
a_2 &= w + iz
\end{aligned}
\tag{5.65}
$$

and use some suitable discretization, such as the Douglas or Backwards Euler scheme, say. Let

$$
\mathbf{F} = (f_1, f_2, f_3, f_4) = 0
\tag{5.66}
$$

represent the four resulting equations—here we have placed the nonlinear terms of Equation (5.11) on the left hand side of the equals sign—for the values of the field variables at level $r + 1$. If a second order implicit discretization of the operator ∂_{yy} is used, such as would be the case if the Douglas or Backward Euler schemes were implemented, the vector $\mathbf{F}$ has the following dependence:

$$
\mathbf{F} = \mathbf{F}(\mathbf{x}_{r+1}),
\tag{5.67}
$$

with

$$
\mathbf{x}_{r+1} = (u^{s-1}, u^s, u^{s+1}; v^{s-1}, v^s, v^{s+1}; w^{s-1}, w^s, w^{s+1}; z^{s-1}, z^s, z^{s+1})_{r+1}.
\tag{5.68}
$$

Put

$$
\mathbf{x}_{r+1} = \mathbf{X}^l + \delta\mathbf{X}^l
\tag{5.69}
$$

where

$$
\mathbf{X}^l = (U^{s-1}, U^s, U^{s+1}; V^{s-1}, V^s, V^{s+1}; W^{s-1}, W^s, W^{s+1}; Z^{s-1}, Z^s, Z^{s+1})^l
\tag{5.70}
$$

is the lth iteration to the approximation $\mathbf{X}$ of the exact solution $\mathbf{x}$ which is being sought, and

$$
\delta\mathbf{X}^l = (\varepsilon^s, \beta^s, \gamma^s, \zeta^s).
\tag{5.71}
$$

Expand $\mathbf{F}$ about $\mathbf{X}^l$ to linear terms,

$$\mathbf{F}(\mathbf{x}_{r+1}) \approx \mathbf{F}(\mathbf{X}^l) + \mathbf{J}(\mathbf{X}^l) \cdot \delta \mathbf{X}^l. \tag{5.72}$$

The resulting linear system for the unknown vector $\delta \mathbf{X}^l$ is to be solved. Let $\mathbf{X}^{l+1} = \mathbf{X}^l + \delta \mathbf{X}^l$ and iterate until

$$max_{1 \le s \le n} \parallel \delta \mathbf{X}^l \parallel \le O(f(\Delta x, \Delta y)) \tag{5.73}$$

where $O(f(\Delta x, \Delta y))$ is the order of accuracy of the discretization. As a first guess, we set $\mathbf{X}^0 = \mathbf{x}_r$.

The linear system resulting from an implicit scheme, which needs to be solved and recomputed after each iteration, has the following structure:

$$[A_i, B_i, C_i, D_i] \cdot \delta \mathbf{X}^l = [P_i], \quad i = 1, 4 \tag{5.74}$$

where for each i, one of the matrices in A through D is tri-diagonal, and the other three are diagonal. Hence, the full system

$$M\mathbf{x} = \mathbf{b} \tag{5.75}$$

is $4n \times 4n$, and while sparse, it has a large bandwidth.

If, on the other hand, an explicit scheme was used, the matrix to be computed and solved for each iteration would have been 4×4 in size and full. In such a case it was found that the accuracy is only first order in x, and the grid spacing must be impracticably small.

In order to compare the Fixed Point and the Newton schemes insofar as economy of resources, we need to present details of the solution of the matrix problem in Equation (5.75). A way to efficiently solve Equation (5.75), which by no means is implied to be the optimum way, is to use a pre-conditioning matrix. See [68], p527.

For each iteration, we need to solve Equation (5.75), which can be recast as

$$\tilde{M}\tilde{\mathbf{x}} = \tilde{\mathbf{b}},$$

in which

$$\tilde{M} = C^{-1}MC^{-1}$$

$$\tilde{\mathbf{x}} = C\mathbf{x}$$

$$\tilde{\mathbf{b}} = C^{-1}\mathbf{b}. \tag{5.76}$$

where C is a pre-conditioning matrix such that

- $\| C^{-1}M \| \leq \| M \|$, for convergence,

- The condition number $\kappa(C^{-1}M) \leq \kappa(M)$, where $\kappa(M) = \| M \| / \| M^{-1} \|$,

- C is easily invertible,

- C optimally has small storage requirements.

The iterative matrix solution process itself is thus

$$\mathbf{x}^{\nu+1} = \mathbf{x}^\nu + \alpha(C^{-1}\mathbf{b} - C^{-1}M\mathbf{x}^l). \tag{5.77}$$

The two goals, which can be in many instances incompatible, are high speed, measured in number of computations, and low storage requirements. In what follows, we shall compromise on storage economy for the sake of speed, i.e. suppose the computational domain, which is always fairly large, is not too large. A good choice for C, since M is strongly diagonally dominant in our problem, is to use the symmetric positive definite tri-diagonal part of M. In order to achieve efficiency, the key is to juditiously carry out the multiplies of Equation (5.77), so that operations are performed on vectors as soon as possible, rather than matrices. For example, after computing C^{-1}, which incidentally

will be a full matrix but that needs to be computed only once for each x_r, we find $M\mathbf{x}^l = \mathbf{q}$, a vector; next, compute $C^{-1}\mathbf{q}$, another vector, and so on.

The operation count, for the Newton Method can be estimated as follows: for each value of x_r, we need to solve iterably for the lth value of $\delta\mathbf{X}$, and for each $\delta\mathbf{X}^l$ we need to iterably solve Equation (5.77). First, since M is a $4n \times 4n$ matrix, we require at most $O(n^2)$ operations to find C^{-1}. This calculation needs to be done only once for the solution of Equation (5.77) since we use the same C^{-1} until the iteration of Equation (5.77) converges, for each ν, we have $O(n^2)$ operations. This number of operations is in turn performed ν times to find the $(\nu + 1)^{th}$ vector. The estimate for the number of iterates needed to solve for $\mathbf{x}^{\nu+1}$ depends on the specific form of M. However, we guess that the number of iterations required is perhaps as good as a conjugate gradient method, which is typically of $O(n)$. In addition, we need to iterate l times to get the $l + 1$ iterate of $\delta\mathbf{X}^l$. An estimate of this number is hard to estimate, but we expect that the Newton converges quadratically, whereas the Fixed Point Method, as we showed previously, converges linearly. Finally, we require this whole process be performed at all values of x, m times. Hence, all told, we have $m \times \nu \times l \times (O(n^2) + O(n))$ operations, and if we suppose $\nu = O(n)$, we conclude that the total count is approximately $m \times l \times O(n^3)$.

An estimate for the operation count for the FPM is as follows. Equation (5.16) leads to the problem

$$L\phi = \mathbf{b} \tag{5.78}$$

for the unknown ϕ, where L is a $2n \times 2n$ tri-diagonal matrix, m times to cover all values of x in the domain. The efficient way to solve Equation (5.78) is to decompose the problem in two steps: let $L = WU$, where W is a lower triangular matrix and U and upper triangular matrix. Then, solve

$$W\mathbf{g} = \mathbf{b} \tag{5.79}$$

is solved for **g**, followed by

$$U\varphi = \mathbf{g}. \qquad (5.80)$$

to finally obtain φ. The total operation count for the solution of Equations(5.79) and (5.80) is $(5n - 4)$ multiplies and $(3n - 3)$ adds. All told, $O(16n)$ operations. In turn, this process is performed l times to compute the $(l + 1)^{th}$ iterate, and finally m times to cover all values of x. The total is $m \times l \times O(n)$. Thus, the operation count ratio for these two methods is $O(\sqrt{l} \times n^2)$, having assumed that the Newton method converges quadratically in the iteration process. Hence, the Fixed Point Method is considerably faster.

We can also compare storage requirements. For FPM, we need to store the old and the new vector at each x, and another vector for the iteration process, hence we store $6n$ values–note that for our problem each entry in the vector is of size $2n$. In addition, we need to store all the entries of a tri-diagonal matrix of size $2n \times 2n$, or roughly $6n$ values.[4] The total is thus $12n$, or $O(n)$ values. For the Newton Method, we have $12n$ values which constitute the old and new vector elements plus a storage vector for the iteration plus roughly $24n$ for the matrix M entries, with an additional n^2 for the pre-conditioning matrix. The total is $O(n^2)$. The ratio of storage requirements of the two methods is $O(n)$.

The FPM, as we hope we have been able to show, has many attractive features. Note that its economy of resources hinges upon the simplicity of the matrix that the discretization generated. If higher order accuracy is required, the matrix will probably be more complicated than the simple tri-diagonal matrix that was used in this study, requiring greater computational resources. A somewhat unavoidable problem with the

---

[4]In fact, we could be even more economical and use multipliers in the entries of L, so that only one half of the tri-diagonal matrix entries need to be stored.

FPM is that the method has noticeable dissipation. As we shall show, however, the dissipation can be made tolerable at the expense of greater computational resources. We do not know with certainty the cause for the dissipation and further study is required, perhaps by applying this scheme on a nonlinear equation for which a great deal more is known about its behavior and its solution.

To illustrate the degree of dissipation in the surface system FPM implementation we used the same parameters and domain that was used in connection with the iteration issue, and we fixed the iteration tolerance at 10^{-6}. Two types of trials were carried out, both were carried out using a flat bottom. In the three-dimensional trial we assumed the boundary conditions were $\mathcal{A}_1 = 0.5 + 0.01y$, and $\mathcal{A}_2 = 0.1 + 0.01y$, and monitored the conserved quantity, Equation (4.26), along the length in the x direction, midway in the span-wise direction. The derivatives that appear in Equation (4.26) were second-order center-differenced. In the two-dimensional trial, we set $\mathcal{A}_1 = 0.5$, and $\mathcal{A}_2 = 0.1$, and monitored the conserved quantity, Equation (4.62), along the same ray. The outcome of both trials was qualitatively similar: the computed conserved quantity oscillated with a period equal to the interaction length. The difference between the peak value and the minimum value increased as the grid size was made larger. In addition, dissipation, i.e. the drop of the peak value as a function of position x increased as the grid size was made larger, and as a result, the resulting local interaction length grew since the amplitude of the modes were attenuated. While we were unable to find the cause for such an outcome, we do know that it is not related to the discretization of the ∂_{yy} operator or to boundary effects, since the problem also arises in the two-dimensional trial, which has no y dependence. We also tried changing the iteration discrepancy tolerance and saw no correlation between the value of this parameter and the dissipation. We did find, however, that the dissipation and oscillation of the conserved quantities can be made negligible by

Grid Size Δ	Fluctuation
4.00	0.1002
2.00	0.0627
1.00	0.0168
0.50	0.0050
0.25	0.0014

Table 5.1: Energy fluctuation vs. grid size. Equilateral grid case.

making the grid size small. We also found that the effect is much more pronounced when $\mathcal{A}_2 = 0$ exactly, which yields solutions with very sharp minimas in the field variables. Table 5.1 shows the difference between succesive maxima and minima for the second trial as a function of grid size, with $\Delta x = \Delta y$. We also report the outcome of fixing $\Delta x = 0.25$ and varying Δy, in Table 5.2, and the opposite settings are illustrated in Table 5.3. The two-dimensional trials for $\Delta x = 0.25$ and $\Delta y = 4$ showed significant discrepancies when compared to the Runge-Kutta calculation, and the energy for this case oscillated in a somewhat irregular pattern. While it is expected that any discretization of the surface system will have inherent dissipation due to truncation, especially manifesting itself for large grid sizes, it is not at all obvious at this stage of the research that the root cause is truncation rather than some other cause.

To conclude this section, we report the wall-clock times for three runs of the surface equations, as discretized using the Fixed Point Method. The code was written in Fortran 77-because of issues related to code portability-in a straight-forward manner, except that recursion was used in the iteration procedure. For the size of these runs, the use of recursion was probably marginally slower than opting for repeated subroutine calls. No

Grid Size Δy	Fluctuation
4.00	0.0018
2.00	0.0013
1.00	0.0013
0.50	0.0012
0.25	0.0014

Table 5.2: Energy fluctuation vs. Δy. $\Delta x = 0.25$ fixed.

Grid Size Δx	Fluctuation
4.00	0.1415
2.00	0.0628
1.00	0.0198
0.50	0.0049
0.25	0.0014

Table 5.3: Energy fluctuation vs. Δx. $\Delta y = 0.25$ fixed.

Machine	$\Delta = 1$, (50×50)	$\Delta = 0.5$, (100×100)	$\Delta = 0.25$, (200×200)
Sun Sparc SLC	7.43	25.42	78.8
Sun Sparc 2	2.29	7.81	23.13
Ardent Titan 2X P1	3.9	13.9	44.81

Table 5.4: Wall-clock times in seconds vs. grid size (number of grid points per domain) for the computation of the surface system over the whole domain using the Fixed Point Method.

Machine	$\Delta = 1$, (50×50)	$\Delta = 0.5$, (100×100)	$\Delta = 0.25$, (200×200)
Sun Sparc SLC	0.16	0.25	0.50
Sun Sparc 2	0.06	0.08	0.15
Ardent Titan 2X P1	0.08	0.13	0.29

Table 5.5: Wall-clock times in seconds for the computation of the surface system for all values of y at a particular x using the Fixed Point Method.

machine optimization, or floating point accelerators were utilized.[5] The time trials were carried out with an initial bottom configuration $f = 0.01x$. All other parameters and physical quantities were the same as those used previously. The domain was a square with 50 units to its side. Two times are reported, the first one, in Table 5.4, corresponds to the total time required to find the field variables everywhere in the domain, and a second one, given in Table 5.5, is the time required to compute all values in the y direction, for a particular x.

---

[5] The Titan's vectorizability was not exploited either. Otherwise, its reported performance would not compare so unfavorably.

Chapter 6

Qualitative Features of the Solutions to the Full Model

The main qualitative features of the full model are presented in this chapter, using examples computed numerically with the Fixed Point Method. The main points of the chapter are: To present the effects of different initial bottom configurations and boundary conditions on the surface and on the eventual bottom topography after the passage of many surface waves; and to show that when the slopes of the ocean bottom are very mild and the back-wash negligible, the reflected wave plays a relatively minor role in determining the shape of the ocean surface and therefore of the sand-ridge topography.

6.1 General Behavior of the Solutions

To better discern the effects of different bottom topographies on the surface waves and on the eventual bottom topography after the passage of many waves, attention will now be given to the case in which the initial bottom configurations are strictly x-dependent and the boundary conditions are constant. Briefly, in this case, a larger number of bars form when the gradient is slight. the distance separating the bars increases seaward for the positively sloped case, and initial bottom discontinuities in the x direction tend get "smoothed out" after the passage of many waves.

The modes for waves that are traveling normal to the shore over topography described as $f = 0.006x$ are displayed in Figure 6.1. Figure 6.2 shows the eventual topography of a bottom which was initially the sloped but featureless profile of the last example. Superimposed, but not drawn to scale, is the actual ocean surface, composed exclusively of an incident wave field pictured at $T = 0$. Figure 6.3 shows the eventual topography of a bottom which initially had a step in its profile. Note the smoothing effect due to the passage of many waves. All of these figures had $\alpha = 0.1, \varepsilon = 0.2, \beta = 0.08, \omega_1 = 1.8$. For the same range of parameters, Figure 6.4 shows the effect on the surface and on the eventual bottom, of an initial topography that is approximately tuned to the interaction length of the surface waves.
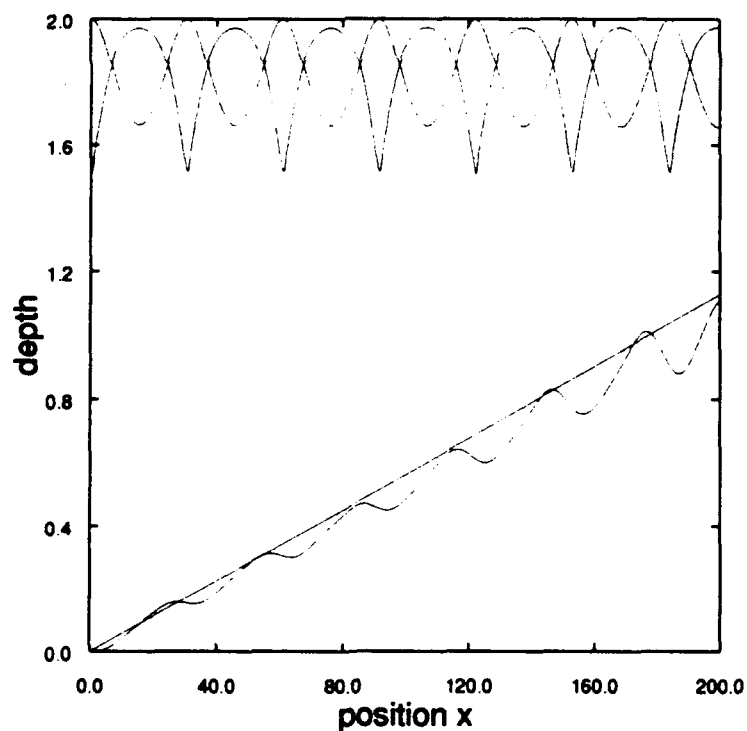
Figure 6.1: a_1 and a_2, for $f(x,y) = 0.006x$. $a_1(x = 0) = 0.5$, $a_2(x = 0) = 0.01$

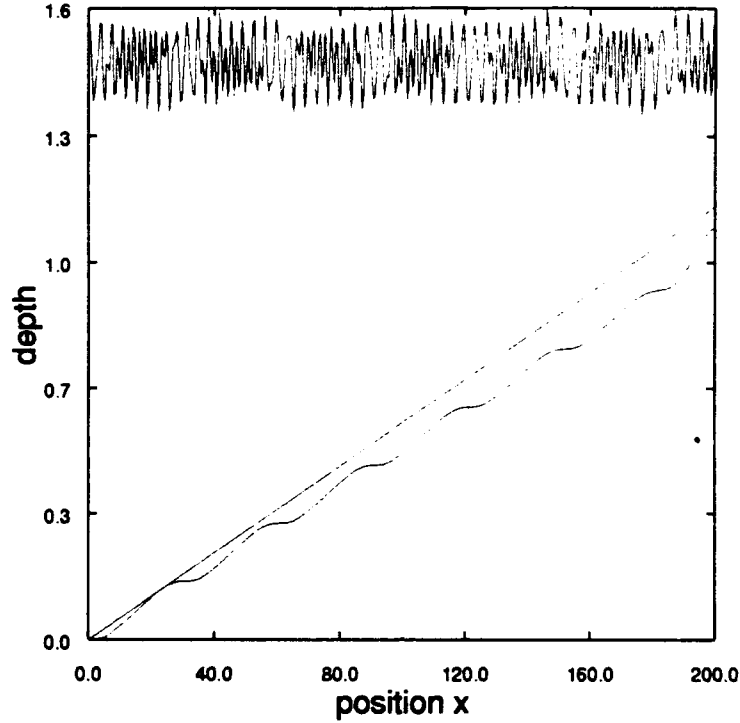A bottom which initially had gradients in the y direction bends the water waves

Figure 6.2: Ocean surface at $T = 0$, and below, bottom topography at $T = 0$ and $T = 100\Delta T$. Not drawn to scale.

affecting the eventual bottom topography by producing a series of bars with refractive features. Consider, for example, the case in which the initial bottom topography is $f(x,y) = 0.01y$, with all other parameters as before. except $\omega_1 = 1.2$. Figure 6.5 shows a_2 at $T = 0$ and Figure 6.6 shows the refracting bottom at $T = 400\Delta T$. A striking way in which refraction takes place can be seen in the case for which the boundary conditions at $x = 0$ are y dependent. The case for which $f(x,y) = 0$ at $T = 0$ and the boundary conditions are $\mathcal{A}_1 = 0.5 + 0.01y$ and $\mathcal{A}_2 = 0.1 + 0.01y$, corresponding to an incoming gravity wave that has slightly higher amplitude at one end than at the other, is shown in Figures 6.7, 6.8 for $a_2(T = 0)$ and $f(T = 400\Delta T)$, respectively.

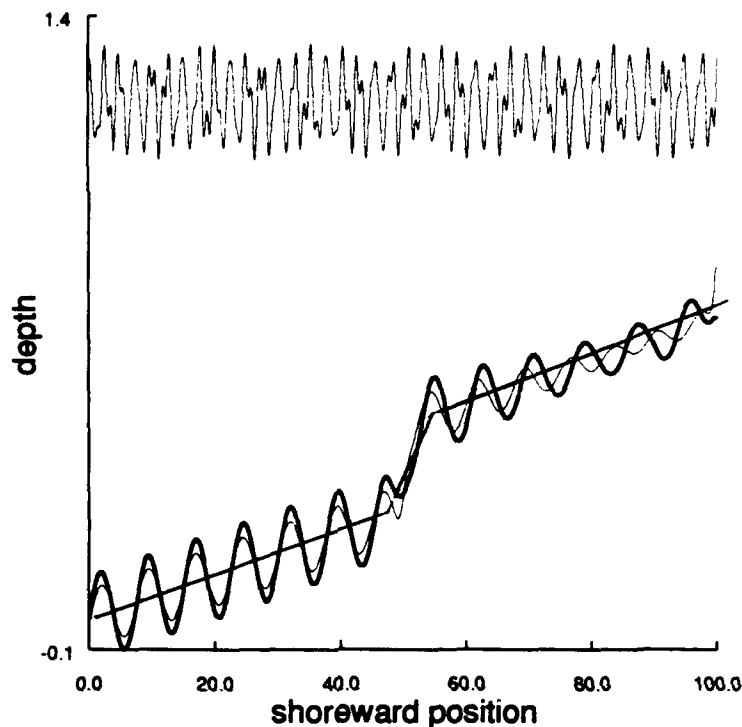Interesting configurations are achieved when the above-mentioned effects are com-

Figure 6.3: The fate of the topography which initially contained a step, shown at three different times.

bined. Figure 6.9 illustrates the outcome, after $T = 400\Delta T$, on a bottom topography for which $\mathcal{A}_1 = 0.5 - 0.01y$, $\mathcal{A}_2 = 0.1 - 0.01y$, and the bottom at $T = 0$ was $f(x,y) = 0.01y$.

The eventual fate of a bottom which initially was smooth but sloped in the longshore direction is illustrated in Figure 6.10. The boundary conditions in this example were $\mathcal{A}_1 = 0.5, \mathcal{A}_2 = 0.1$, the initial bottom is described in the figure. Of note is the apparent growth, and motion of the sand ridges in the shoreward direction, particularly where the water column is deepest.
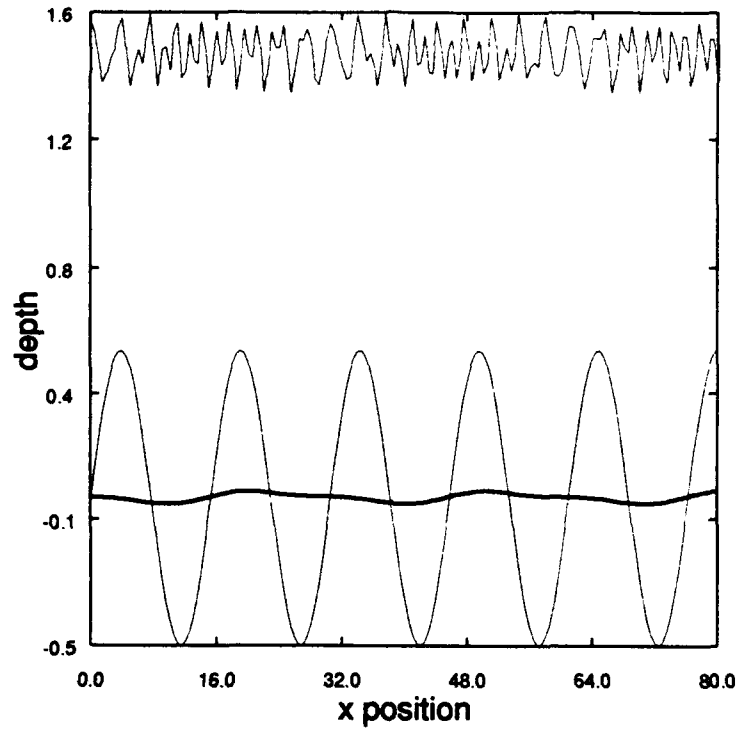
Figure 6.4: Effect of a tuned bottom, $f = 0.5\sin(0.412x)$ at $T = 0$, on the eventual topography and ocean surface: Light solid line. Bottom at $T = 100\Delta T$: Dark solid line.

6.2 Contribution of the Reflected Component to the Surface Waves

Shown in Figure 6.11 is the cross-section of mode $a_1(x,y)$, and in Figure(6.12) a comparison of the eventual bottom with and without contributions from the reflected field. Both figures were computed using Equation (4.1), with $A_1 = 0.5$, $A_2 = 0.01$, $B_1 = 0.2$, and $B_2 = 0.$; $\varepsilon = 0.2$, $\alpha = 0.1$, $\beta = 0.08$. The bottom was $f(x,y) = 0.006x$ at $T = 0$. The domain was 200 units long.

As was discussed in chapter 2, the reflected and incident fields are completely decoupled, owing to the assumptions made concerning the bottom topography. The deformations on the bottom topography due to the reflected component are entirely determined
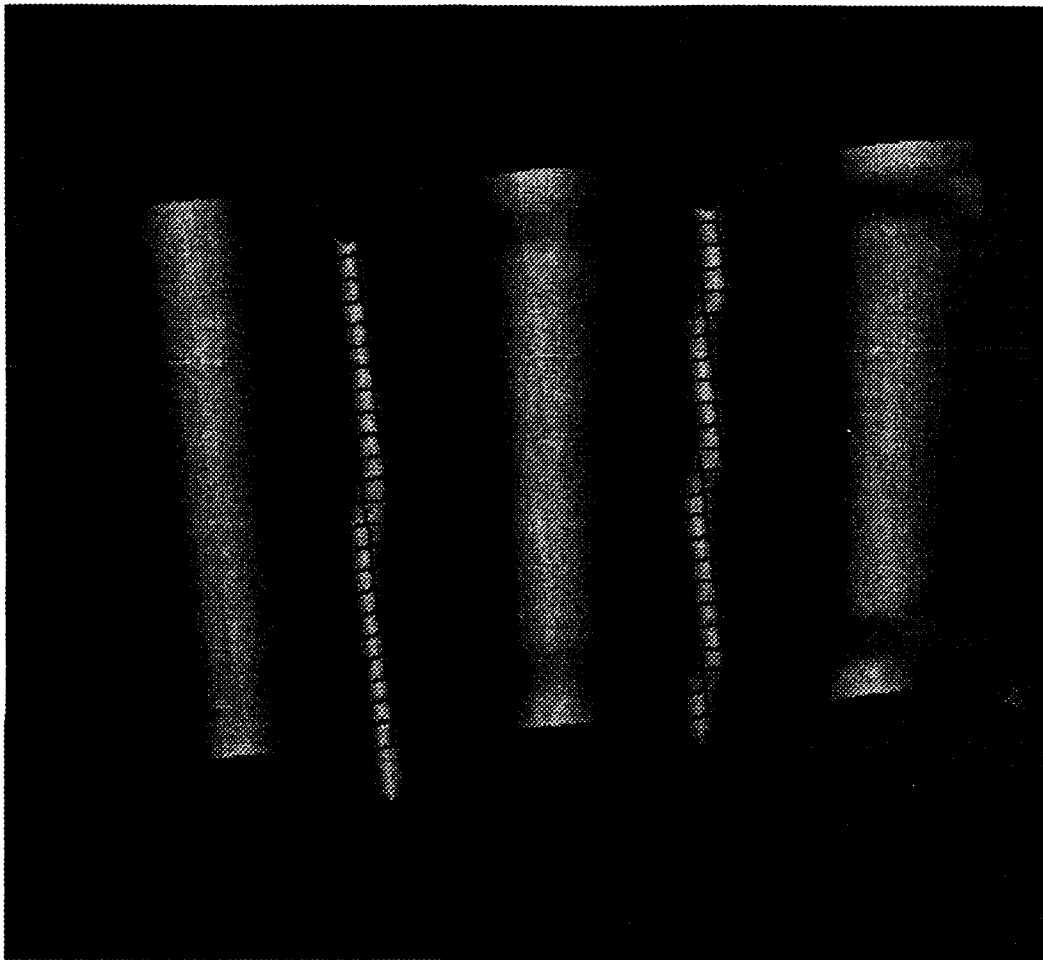
Figure 6.5: Refraction on the surface modes due to the bottom topography. Shown at $T = 0$.

by the amount of energy in the boundary conditions. Hence, it is necessary to include the reflected component when the sea-going wave backwash is not negligible.

If the spatial scales of variation in the bottom topography in the shoreward direction are of the same order as those of the surface waves, then scattering plays an important role in the energetics of these surface waves; hence the reflected component must be included even if the backwash is negligible. The model for the surface waves, in this case, is given by Equation (2.75).

6.3 Periodic Solutions to the Surface System

To give an idea of the rich structure of the surface system, Equation (4.14) is solved in the following examples using periodic boundary conditions in y. The parameter δ is considered independent of frequency. The following graphs were generated using the Fixed Point Method, in which the linear operator is discretized using the Douglas Scheme. The discretization yields a tri-diagonal matrix problem, with additional non-zero constant entries in the upper right-hand corner and the lower left-hand corner. This type of matrix is known as a "Jacobi matrix", and shows up, for example, in the solution to the Toda lattice problem with periodic boundary conditions. In the figures, two periods in y are plotted in tandem, the calculation being performed on only one of the two periods. The domain has $M = 240$ and $N = 150$, and the the fundamental frequency used was $\omega_1 = 1.2$. The parameters were $\alpha = 0.1$ and $\beta = 0.18$. The solution to the case with boundary conditions $\mathcal{A}_1 = 0.5 + 0.1\sin(\frac{3}{N}\pi y)$ and $\mathcal{A}_2 = 0$ is illustrated in Figure 6.14. For the same parameters, but with the boundary condition $\mathcal{A}_1 = 0.1\sin(\frac{3}{N}\pi y)$, the outcome is shown in Figure 6.15. Comparison of the last case to the case in which $\delta = 0$ is given by Figure 6.13.

An interesting pattern arises in the evolution of a case with quasi-periodic boundary conditions; $\mathcal{A}_1 = 0.1[\sin(\frac{3}{N}\pi y) + \sin(\frac{8}{N}\pi y)]$ and $\mathcal{A}_2 = 0$. The outcome is Figure 6.16, with the same parameter values as in the previous figure, except that $\delta \neq 0$. The outcome shown in Figure(6.16) is obtained for the boundary conditions $\mathcal{A}_1 = 0.1(\sin(\frac{3\pi y}{N}) + \sin(\frac{8\pi y}{N})$ and $\mathcal{A}_2 = 0$ (i.e., quasi-periodic), and $\delta \neq 0$. The numerical solution of this last example suggests that solutions to the surface system are stable and periodic.
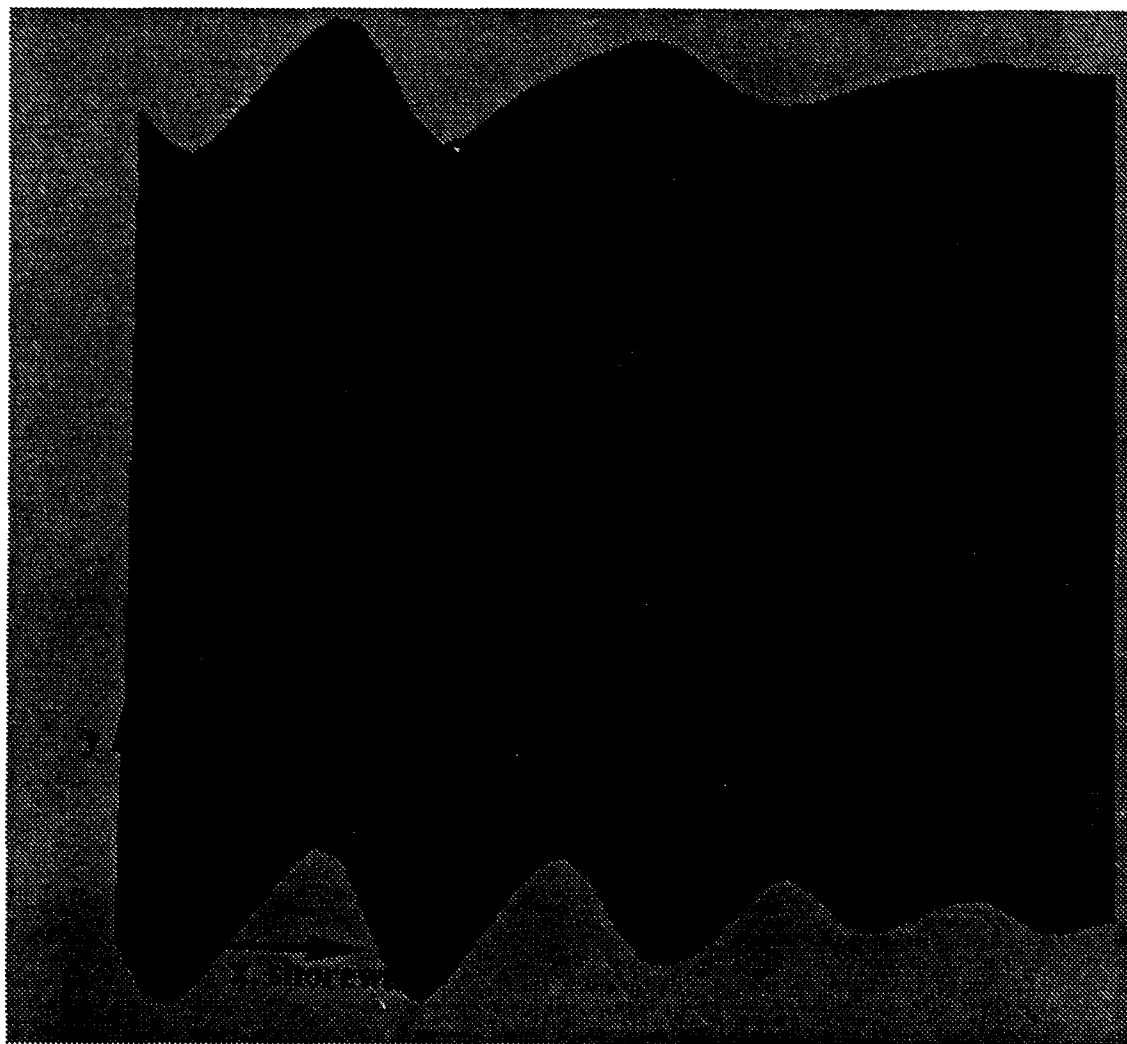
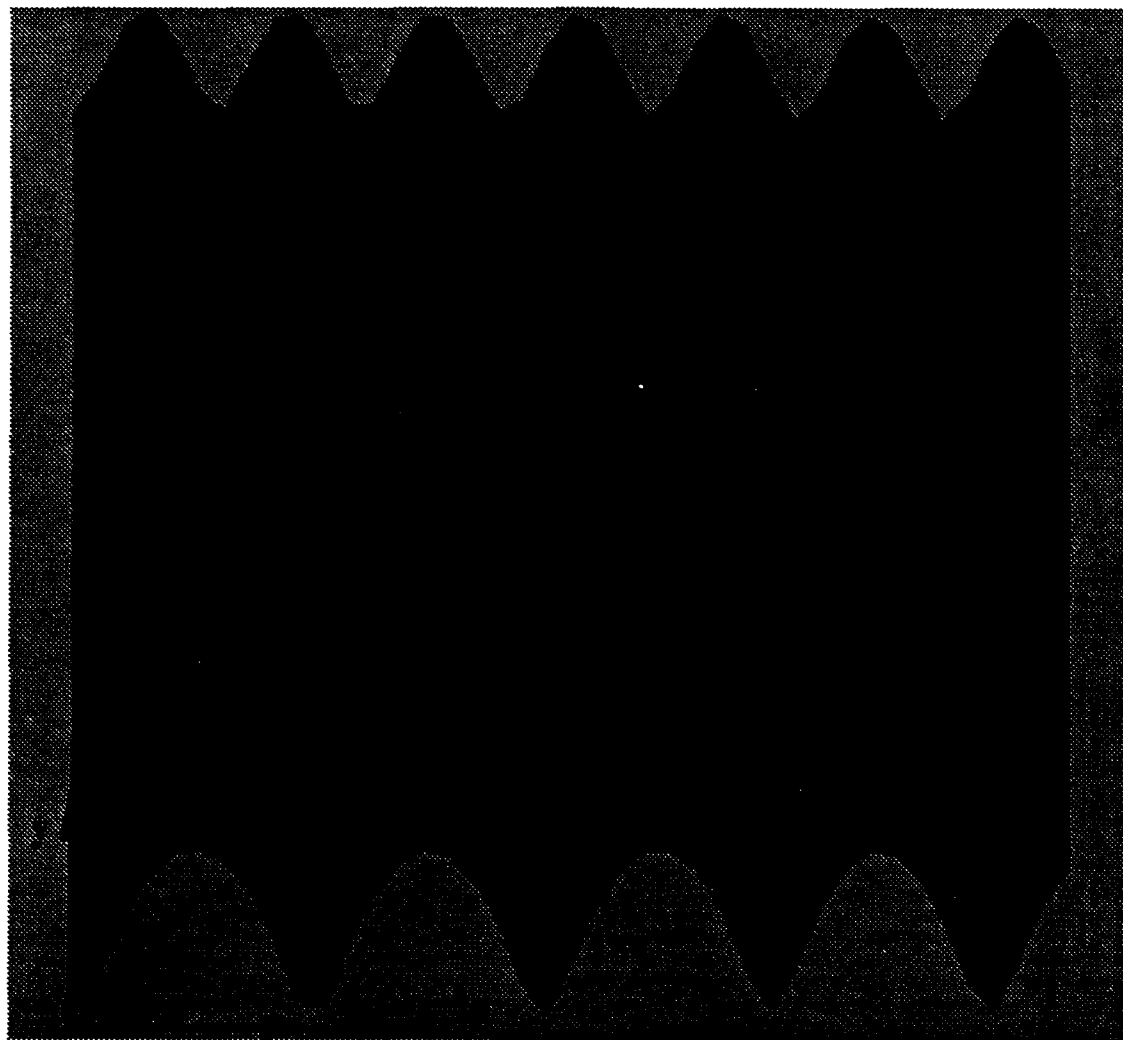Figure 6.6: Refraction due to initial bottom configuration. Bottom at $T = 400\Delta T$.

Figure 6.7: Refraction due to boundary conditions. a_2 at $T = 0$.
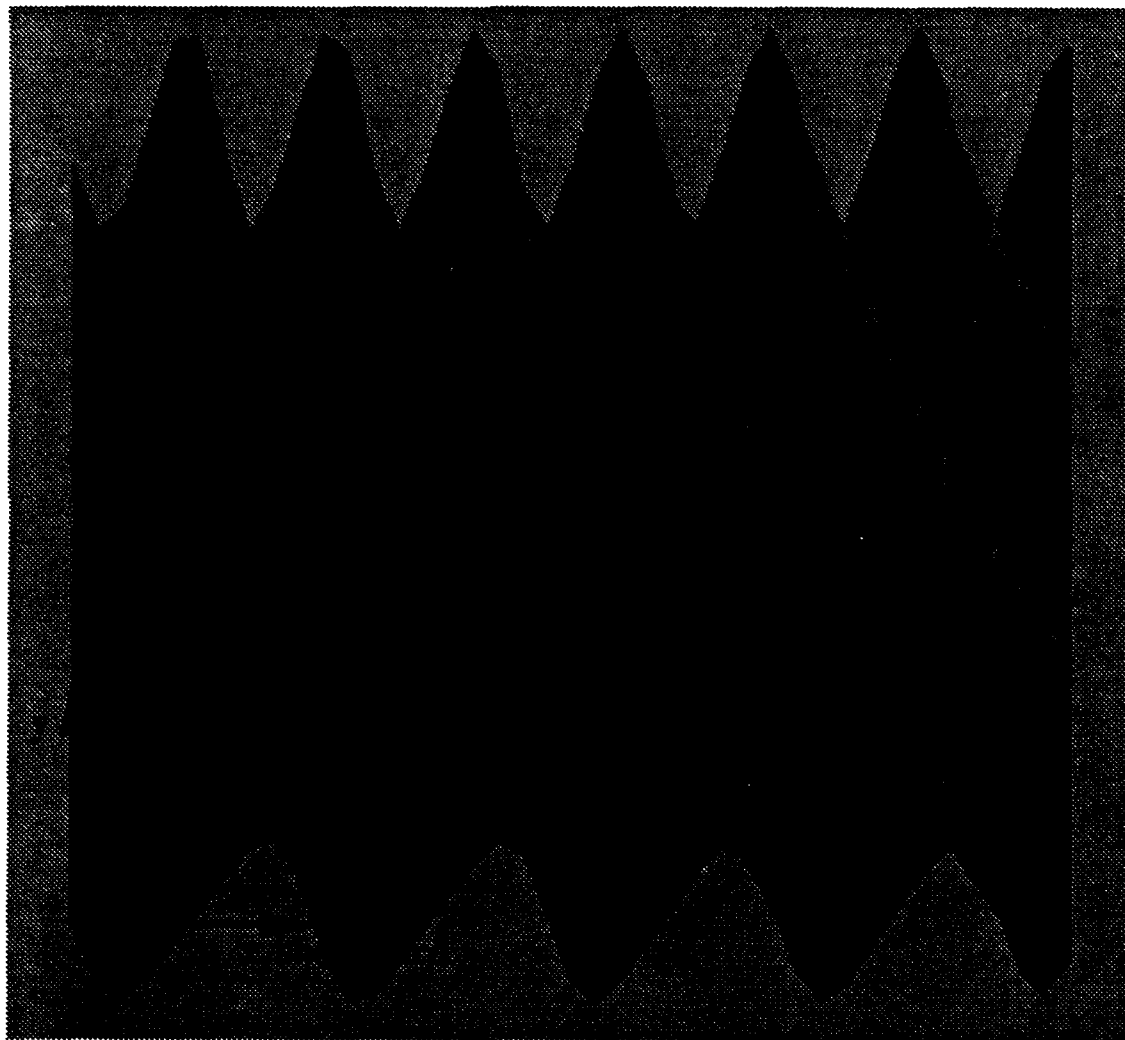
Figure 6.8: Refraction due to boundary conditions. Bottom at $T = 400\Delta T$.
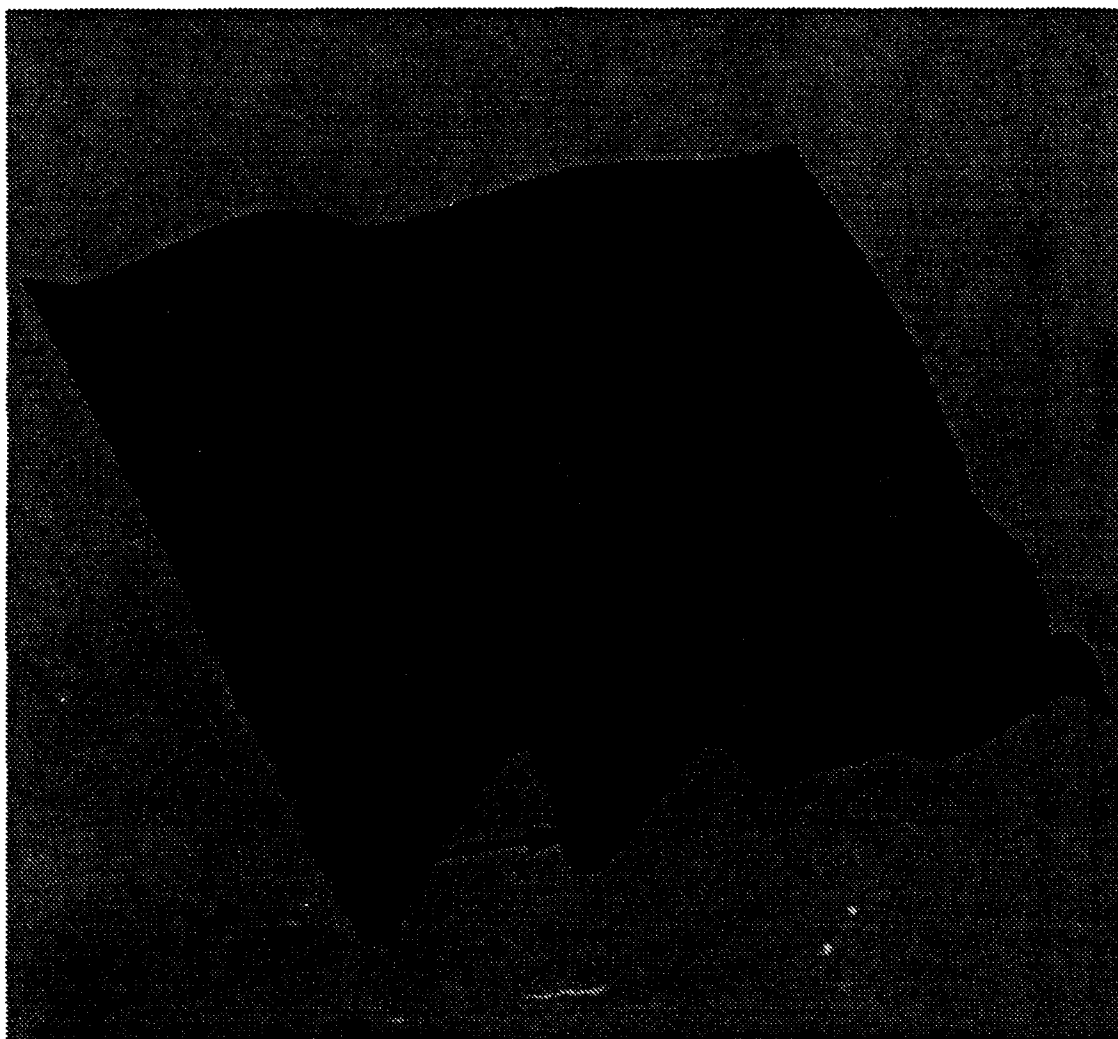
Figure 6.9: Refraction due to boundary conditions and initial bottom configuration. Bottom at $T = 400\Delta T$.
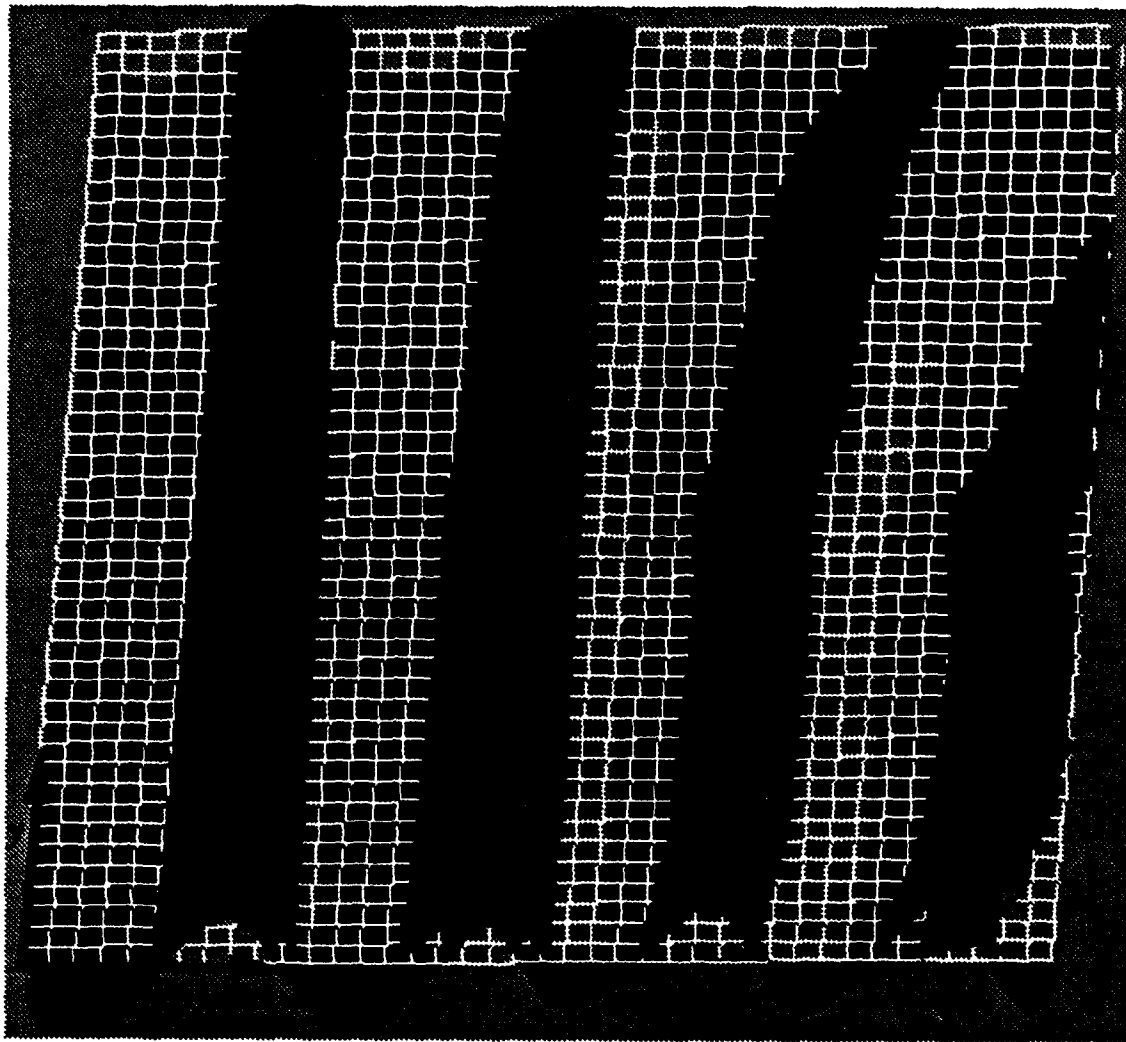
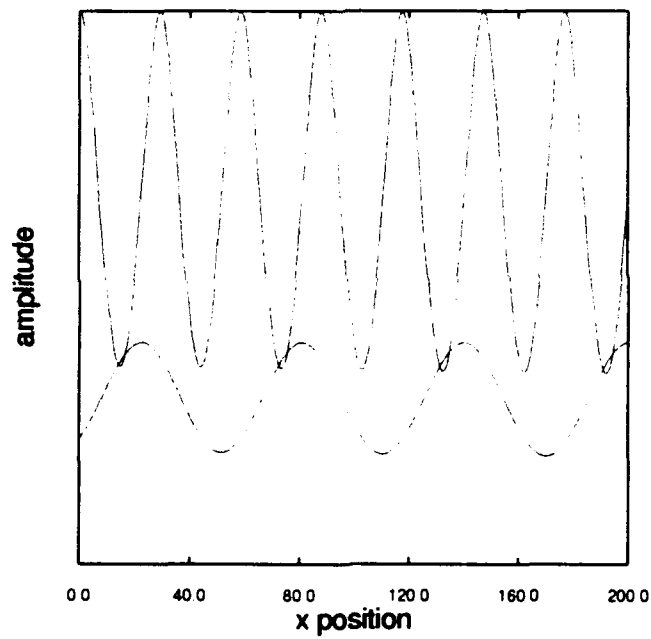Figure 6.10: Evolution of bottom topography. T=0: grid. T=200: grey. T=400: dark.

Figure 6.11: Profile of a_1 and b_1, for $f(x, y) = 0.006x$. $\mathcal{A}_1 = 0.5$, $\mathcal{B}_1 = 0.2$.
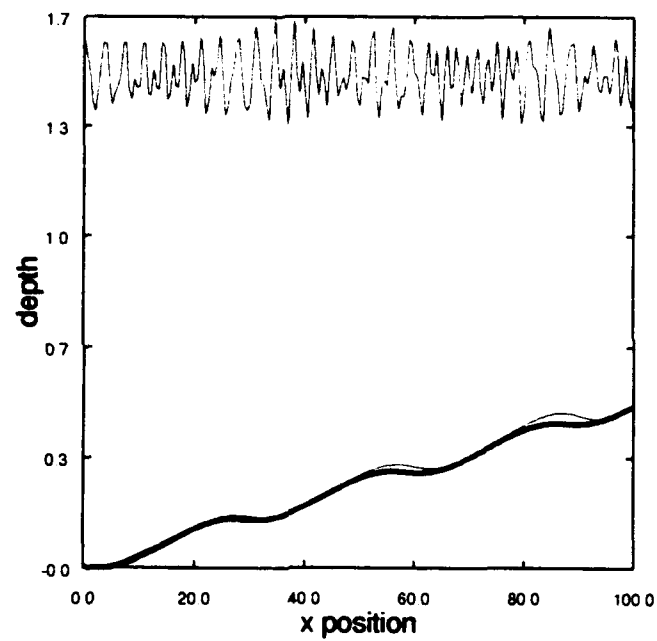
Figure 6.12: Effect of a bi-directional surface wave field on the eventual bottom configuration. Initially, $f(x, y, 0) = 0.006x$. The dark line is the bottom resulting from a strictly shoreward-directed wave.
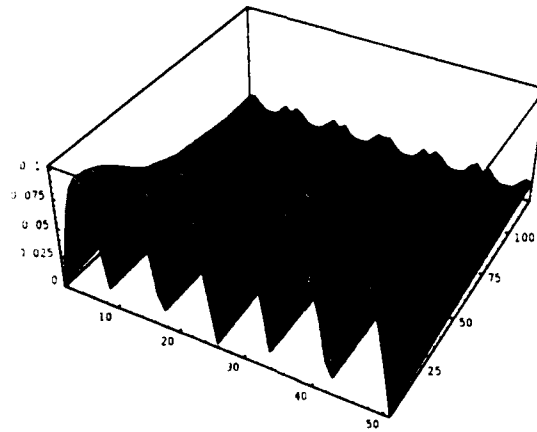
Figure 6.13: $u(x, y)$ for boundary conditions $\mathcal{A}_1 = 0.1 \sin(\frac{3}{N}\pi y)$, $\mathcal{A}_2 = 0$, and detuning parameter $\delta = 0$.

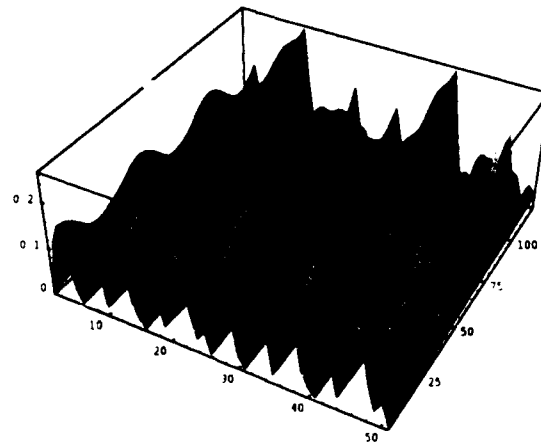Figure 6.14: $u(x, y)$ for $\mathcal{A}_1 = 0.5 + 0.1 \sin(\frac{3}{N}\pi y)$, $\mathcal{A}_2 = 0$, and $\delta \neq 0$.
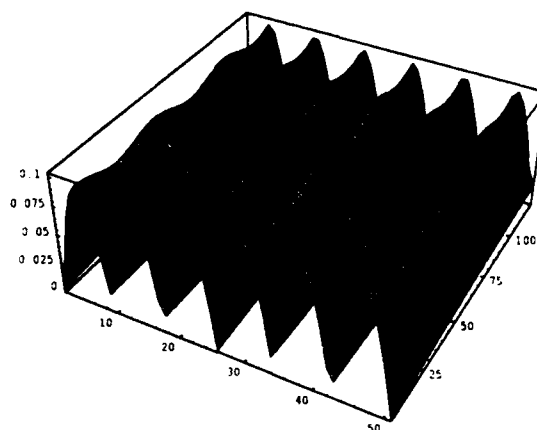
Figure 6.15: $u(x, y)$ for $\mathcal{A}_1 = 0.1 \sin(\frac{3}{N}\pi y)$, $\mathcal{A}_2 = 0$, and $\delta \neq 0$.
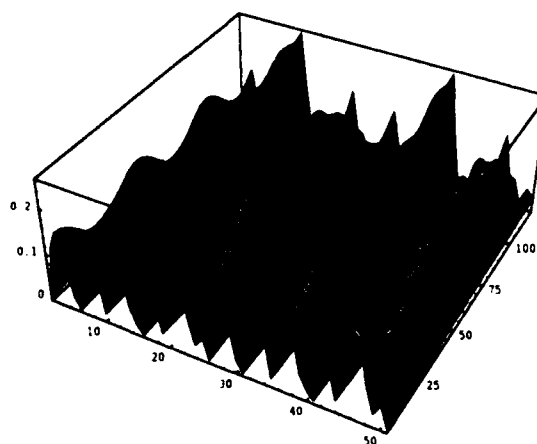

Figure 6.16: Solution for quasi-periodic boundary conditions: $\mathcal{A}_1 = 0.1[\sin(\frac{3}{N}\pi y) + \sin(\frac{8}{N}\pi y)]$, and $\mathcal{A}_2 = 0$. $\delta \neq 0$.

Chapter 7

Conclusions and Future Research Plans

This study detailed the construction and implementation of a model for the formation and evolution of three-dimensional sedimentary structures on the continental shelf, based on the energetic interactions of weakly nonlinear long waves with the shelf's sedimentary topography. This chapter turns its attention to the larger picture, discussing the main conjecture of the study, as well as the methodological aspects pertinent to future research.

The main conjecture of this study is that a significant, but by no means exclusive, agent for the formation and evolution of longshore sand ridges on regions of the continental shelf that are sufficiently removed from the shoaling area is the repeated action of the second-order oscillatory drift velocity that results from the passage of weakly nonlinear shallow-water internal or surficial waves. The basis for the conjecture rests on (1) the close correlation between the inter-bar spacing and the length in which energetic exchanges among the most powerful modes of the shallow water waves takes place; (2) the close correlation between the evolutionary time scales for the bars and the time required for highly coherent nonlinear dispersive wave trains to impart sufficient energy into a boundary layer to significantly transform a sediment-laden bottom topography; (3) the fact that longshore sand ridges are found in areas in which no wave breaking

occurs and/or in which the reflected field is absent or negligible; (4) the claim that sand ridges with highly organized characteristics may be found in regions in which coherent weakly nonlinear dispersive waves exist; and (5) that the energy of these waves is of the correct magnitude to significantly affect the topography of a sediment-laden bottom.

At present, neither the dynamics of sedimentation nor those of water waves are fully understood. The model presented here represents the conjecture based on current understanding of both processes. If the conjecture is correct, the model will improve in predictive power as understanding of sedimentation and wave dynamics improve. However, the more important functions played by the model are that its development yiels clues to ways in which the conjecture itself may be refined and tested, as well as providing conceptual spin-offs (such as the modal surface system that appears in this study) which are interesting independent of the sedimentation problem at hand.

The model in its inception was two-dimensional. Based on encouraging comparisons with actual field data, the three-dimensional version was developed and made the subject of this study. Briefly described, the present model couples a mass transport equation, which controls the history of the bottom topography, to a mathematical equation, which describes the evolution of the most energetic modes of surface or internal weakly nonlinear dispersive shallow water waves with weak span-wise spatial dependence. In order to solve the coupled system one must rely on the discrepant time scales of the bottom evolution and of the water waves to effectively decouple their interaction, making a solution by iteration possible.

In the near future the modal representation of the water waves will be replaced with a full Boussinesq system, and the effects of oceanic currents will be included in the model. Bona and Saut [69] are presently studying the different versions of the Boussinesq system in order to determine, among other things, which variant best models oceanic

waves, and which is well-posed as a boundary value problem. Additionally, a number of issues brought up in this study need to be pursued to completion. These include the search for stable bottom configurations as predicted by the model, completion of the well-posedness theory and the Hamiltonian structure for the surface system, and development of a stability result for the iterative procedure that was used to solve the coupled surface/mass transport equations.

The sensible way to test the conjecture and the model is, of course, to examine oceanic field data. Comparisons with oceanic field data can assess the predictive powers of the model; laboratory experiments cannot, however, as they do not scale well. The task of making field observations, particularly in the three-dimensional case, is a tedious, expensive, and sometimes difficult enterprise. While researchers at the INRS at the University of Quebec, headed by Prof. Boczar-Karakiewicz, were able to make some comparisons between the two-dimensional version of the model and sand ridge data [2], finding that the model's predictions agreed qualitatively with the height, spacing, and evolution trends of the actual bars, they have not yet taken on the task of making comparisons in the three-dimensional case. As of this writing, the Quebec team is reducing field data from the continental shelf, gathered from the ocean floor neighboring Newfoundland and Eastern Australia.

There are, however, several aspects of the conjecture which can be tested in the laboratory as well as in the field. The drift velocity created by shallow water waves of the type identified here as responsible for the formation of longshore sand ridges must be observed and studied in a laboratory setting. Comparisons between the laboratory experiments and the drift velocity measurements in sand ridge fields could prove fruitful. Additionally, it should be possible to correlate the drift velocity to the shallow water waves in question both in the laboratory and in the ocean.

Field observations are needed to (1) determine the importance of both the reflected wave field and oceanic currents in determining the nature of the drift velocity in sand ridge areas; (2) correlate in some way the beginning and end of ridge fields and the physical location at which water waves are created and eventually destroyed; (3) track the relevant wave spectra in order to see evidence of the predicted pattern in energetic interaction lengths and its correlation to features of the bottom topography; and (4) determine what sort of sand ridge configurations are stable and/or non-migratory.

Laboratory observations are required to determine how well the various Boussinesq systems model the weakly nonlinear shallow water waves and to confirm the existence of recurrence-like solutions over long propagation lengths. Additionally, more experiments aimed at furthering our understanding of the motion of sediment in the boundary layer are needed.

Computational experiments are currently being planned, aimed at exploring the nature of recurrence-like solutions in nonlinear dispersive equations, such as the Boussinesq equation; other experiments will explore the stability and interdependence of the truncated modal solutions to these equations.

In conclusion, this study has produced a wealth of interesting and fundamental questions. While comparisons between field data and the two-dimensional model are very encouraging and this three-dimensional extention should therefore find applicability in the real world environment, any topographical chart of the continental shelf provides a good reminder of the long path yet to travel toward a complete understanding and model of the full problem. If this study has piqued the curiosity and compelled the reader to take a closer look at sandbars, it will have succeeded.

Appendix A

Higher Order Theory

Considered here is the second order contributions to the proposed model. This section is included as an appendix because of it's exploratory nature. The value of these calculations resides in the possibility of discerning if any fundamentally new contributions may arise from a careful inclusion of these higher order terms. The very tedious process of generating the surface contributions at this order, and the daunting problem of formulating the drift velocity, is a veritable project, even for a symbolic solver. The higher order expressions were derived as carefully as possible, nevertheless, it is very possible that algebraic errors were made.

The irrotational condition to this order is

$$\alpha^2 : u_{2y} - v_{2x} - v_{1X} = 0. \tag{A.1}$$

and the continuity condition,

$$\alpha^2 : \eta_{2t} + u_{2x} - \frac{\beta^2 \eta_{2xxt}}{3} = F_2(\eta_0, u_0, v_0, \eta_1, u_1, v_1, G; x, X, y, t), \tag{A.2}$$

where $G(X, y, T) = \frac{\varepsilon f(X, y, T)}{\alpha}$, and

$$F_2 = -v_{1y} + \frac{\beta^2 \eta_{1yyt}}{3} - u_1 X - u_1 \eta_{0x} - G u_{1x} - \eta_1 u_{0x} + \frac{2\beta^2(\eta_{1x X_t} + G\eta_{1xxt})}{3}$$

$$-u_0 \eta_{1x} - \eta_0 u_{1x} - G_y v_0 - G_X u_0 - v_0 \eta_{0y} - G v_{0y} - \eta_0 v_{0y} + \frac{2\beta^2 (G\eta_{0t})_{yy}}{3} \quad (A.3)$$

$$-u_0 \eta_{0X} - G u_{0X} - \eta_0 u_{0X} + \frac{\beta^2 \eta_{0XXt}}{3} + \frac{4\beta^2 G_X \eta_{0xt}}{3} + \frac{4\beta^2 G\eta_{0xXt}}{3}.$$

Reiterating Equation (2.60).

$$\alpha^2: \quad \mathcal{L}\eta_2 = \mathcal{G}_2(\eta_0, u_0, v_0, \eta_1, u_1, v_1, G; x, X, y, t) \quad (A.4)$$

where the linear operator is

$$\mathcal{L} = \partial_{tt} - \partial_{xx} - \frac{\beta^2 \partial_{xxtt}}{3}, \quad (A.5)$$

and the inhomogeneous term is

$$\mathcal{G}_2 = (1 + \beta^2 \partial_{tt}/3)\eta_{1yy} + G(1 + 2\beta^2 \partial_{tt}/3)\eta_{1xx} + 2(1 + \beta^2 \partial_{tt}/3)\eta_{1xX}$$

$$(1 + \beta^2 \partial_{tt}/3)\eta_{0XX} + G(1 + 2\beta^2 \partial_{tt}/3)\eta_{0yy} + 2(1 + \beta^2 \partial_{tt}/3)\eta_{0xX}$$

$$+G_X(1 + 4\beta^2 \partial_{tt}/3) + \eta_{0x} + G_y \eta_{0y} + 2\beta^2 G_{yy}\eta_{0tt}/3 + 4\beta^2 G_y \eta_{0tyy}/3 \quad (A.6)$$

$$-(\eta_1 u_0 + \eta_0 u_1)_{xt} + (u_1 u_0)_{xx} + (u_0^2)_{xX} - (u_0 \eta_0)_{Xt} + G(u_0^2/2)_{xx}$$

$$+(u_0^2/2)_{yy} + (v_0^2/2)_{xx} + (\eta_0^2/2)_{yy} - (\eta_{0t} v_0)_y.$$

Applying the compatibility condition, we get, after a substantial amount of algebra,

$$A_{1x} + i\varepsilon f D_1 E_1 A_1 - i\alpha F_1 A_{1yy} - i\alpha D_1 S_1 e^{-i\delta x}(A_1^* a_2 + a_1^* A_2) = \Omega_1(x, y, a_1, a_2)$$

$$A_{2x} + i\varepsilon f D_2 E_2 A_2 - i\alpha F_2 A_{2yy} + i2\alpha D_2 S_2 e^{+i\delta x} a_1 A_1 = \Omega_2(x, y, a_1, a_2).$$
$$(A.7)$$

for the equations of the modes. The constants on the left hand side are given by Equation

(2.73), and the inhomogeneous terms are

$$
\begin{aligned}
\Omega_1 \;=\; & -p_1 a_{1xyy} - p_2 f(x,y)a_{1x} - p_3 a_{1xx} - p_4 f_x(x,y)a_1 + p_5 f_{yy}(x,y)a_1 \\
& + p_6 f_y(x,y)a_{1y} + p_7 f(x,y)a_{1yy} + \{ -p_8 a_2 a_{1x}^{*} + p_9 a_{2x}a_1^{*} + p_{10}f(x,y)a_1^{*}a_2 \\
& + p_{11}(a_1^{*}a_2)_x - p_{12}(a_1^{*}a_2)_{yy} - p_{13}(a_{1y}^{*}a_2)_y - p_{14}(a_1^{*}a_{2y})_y - p_{15}a_{2y}a_{1y}^{*} \}e^{-i\delta x} \\
& + p_{16}(a_1^{*}a_1^2 + 2a_1 a_2^{*}a_2)
\end{aligned}
$$

$$(A.8)$$

and

$$
\begin{aligned}
\Omega_2 \;=\; & -p_{17}a_{2xyy} - p_{18}f(x,y)a_{2x} - p_{19}a_{2xx} - p_{21}f_x(x,y)a_2 + p_{22}f_{yy}(x,y)a_2 \\
& + p_{23}f_y(x,y)a_{2y} + p_{24}f(x,y)a_{2yy} + \{ -p_{25}a_1 a_{1x}^{*} + p_{26}f(x,y)a_1^2 + p_{27}(a_1^2) \\
& - p_{28}(a_1^2)_{yy} + p_{29}(a_{1y})^2 + p_{30}(a_{1y}a_1)_y \}e^{+i\delta x} \\
& + p_{31}(a_2^2 a_2^{*} + 2a_1 a_1^{*}a_2).
\end{aligned}
$$

$$(A.9)$$

The coefficients appearing in the Ω terms above are explicitly given below:

$$
\begin{aligned}
p_1 \;&=\; 2F_1^2 \\[4pt]
p_2 \;&=\; 2\varepsilon D_1 F_1 E_1/\alpha \\[4pt]
p_3 \;&=\; iF_1/\alpha \\[4pt]
p_4 \;&=\; \varepsilon 2 D_1 F_1\left(1 - \frac{4\beta^2\omega_1^2}{3}\right) \\[4pt]
p_5 \;&=\; i\varepsilon\frac{2}{3}\beta^2\omega_1 D_1 \\[4pt]
p_6 \;&=\; 4i\varepsilon F_1^2 D_1 k_1 + \frac{4}{3}\varepsilon\beta^2\omega_1 D_1/k_1 \\[4pt]
p_7 \;&=\; 4i\varepsilon F_1^2 D_1 E_1 \\[4pt]
p_8 \;&=\; 4D_1 F_1^2(k_2 - k_1)(\omega_2 - \omega_1) \\[4pt]
p_9 \;&=\; 4D_1 F_1^2\omega_2(k_2 - k_1)(\omega_2 - \omega_1)/\omega_1 \\[4pt]
p_{10} \;&=\; \frac{2i\varepsilon F_1 D_1}{\omega_1}(k_2 - k_1)^2[2D_1 E_1(k_2 - k_1) - k_1]
\end{aligned}
$$

$$(A.10)$$

$$p_{11} = \frac{D_1}{\omega_1}\{4F_1(k_2 - k_1)[2E_1F_1(k_2 - k_1) - k_1] - (\omega_2 - \omega_1)(\omega_2/k_2 + \omega_1/k_1)\}$$

$$p_{12} = \frac{4i\alpha F_1 F_2 D_1}{\omega_1}[\frac{k_2(k_2 - k_1)}{2D_1} - k_1k_2 - \omega_1\omega_2]$$

$$p_{13} = 4i\alpha F_1 F_2 D_1 \omega_2^2/\omega_1$$

$$p_{14} = 4i\alpha F_1 F_2 D_1 \omega_1$$

$$p_{15} = 4i\alpha F_1 F_2 D_1 (k_2 - k_1)^2/\omega_1$$

$$p_{16} = \alpha D_1$$

$$p_{17} = 2F_2^2$$

$$p_{18} = 2\varepsilon D_2 F_2 E_2/\alpha$$

$$p_{19} = 3i F_2/\alpha\omega_2$$

$$p_{21} = \varepsilon 2 D_2 F_2(1 - \frac{4\beta^2\omega_2^2}{3})/\alpha$$

$$p_{22} = i\varepsilon\frac{2}{3}\beta^2\omega_2 D_2$$

$$p_{23} = 4i\varepsilon F_2^2 D_2 k_2 + \frac{4}{3}\varepsilon\beta^2\omega_2 D_2/k_2$$

$$p_{24} = 4i\varepsilon F_1^2 D_1 E_1$$

$$p_{25} = i8\omega_1 D_2 F_1 \omega_2$$

$$p_{26} = 2i\varepsilon D_2[\frac{2k_1 E_2}{k_2^2} - 1]k_1^2/\omega_2$$

$$p_{27} = 2D_2[\frac{2F_2 k_1^2}{D_1} - 2\omega_1^2 F_1 - k_1]$$

$$p_{28} = \frac{i\alpha D_2}{\omega_2}[\frac{F_2 k_1}{D_2} - \frac{1}{2}(1 + \frac{k_1^2}{\omega_1^2})]$$

$$p_{29} = 2i\alpha D_2/\omega_2$$

$$p_{30} = i\alpha\omega_1^2 D_2/\omega_2 k_1)^2$$

$$p_{31} = \alpha D_2. \tag{A.11}$$

The drift velocity to second order in α is

$$\langle \mathbf{U}_2 \rangle = \langle \mathbf{u}_2 \rangle + \langle \int^t \mathbf{u}_1 d\bar{t} \cdot \nabla \mathbf{u}_0 \rangle + \langle \int^t \int^{t'} \mathbf{u}_0 dt' \cdot \nabla \mathbf{u}_0 d\bar{t} \cdot \nabla \mathbf{u}_0 \rangle$$
$$+ \langle \int^t \mathbf{u}_0 d\bar{t} \cdot \nabla \mathbf{u}_1 \rangle + \frac{1}{2} \langle \{ \int^t \mathbf{u}_0 d\bar{t} \}^T \cdot H \mathbf{u}_0 \cdot \int_{t_0}^t \mathbf{u}_0 dt \rangle. \qquad (\text{A.12})$$

which, after weak y dependence scaling is adopted, can be expressed in component form as

$$\mathcal{U} = \langle u_2 \rangle + \langle \int^t v_0 d\bar{t} u_{0y} \rangle + \langle \int^t u_1 d\bar{t} u_{0x} \rangle + \langle \int^t w_1 d\bar{t} u_{0n} \rangle + \langle \int^t u_0 d\bar{t} u_{1x} \rangle + \langle \int^t w_0 d\bar{t} u_{1n} \rangle$$
$$\langle \{ \int^t \int^{\bar{t}} u_0 dt' u_{0x} d\bar{t} + \int^t \int^{\bar{t}} w_0 dt' u_{0n} d\bar{t} \} u_{0x} +$$
$$\{ \int^t \int^{\bar{t}} u_0 dt' w_{0x} d\bar{t} + \int^t \int^{\bar{t}} w_0 dt' w_{0n} d\bar{t} \} u_{0n} +$$
$$\frac{1}{2} (\int^t u_0 d\bar{t})^2 u_{0xx} + \frac{1}{2} (\int^t w_0 d\bar{t})^2 u_{0nn} \rangle$$

$$\mathcal{V} = \langle v_2 \rangle + \langle \int^t v_0 d\bar{t} v_{0y} \rangle + \langle \int^t u_1 d\bar{t} v_{0x} \rangle + \langle \int^t w_1 d\bar{t} v_{0n} \rangle + \langle \int^t u_0 d\bar{t} v_{1x} \rangle + \langle \int^t w_0 d\bar{t} v_{1n} \rangle$$
$$\langle \{ \int^t \int^{\bar{t}} u_0 dt' u_{0x} d\bar{t} + \int^t \int^{\bar{t}} w_0 dt' u_{0n} d\bar{t} \} v_{0x} +$$
$$\{ \int^t \int^{\bar{t}} u_0 dt' w_{0x} d\bar{t} + \int^t \int^{\bar{t}} w_0 dt' w_{0n} d\bar{t} \} v_{0n} +$$
$$\frac{1}{2} (\int^t u_0 d\bar{t})^2 v_{0xx} + \frac{1}{2} (\int^t w_0 d\bar{t})^2 v_{0nn} \rangle.$$

$$(\text{A.13})$$

The longshore drift velocity was calculated for which the second order velocity in the boundary layer, Equation (3.21), is needed. The calculation was carried out by isolating the contributions at the first and second harmonics to the velocity. Once the velocity was calculated, Equation (A.13) was computed explicitly. Finally, U gets integrated over the depth of the boundary layer since the density distribution for the sediment is assumed constant. The resulting expression for the longshore mass transport velocity is

$$\mu_2 = \sum_{j=1}^{2} \frac{C_j}{\sigma_j} [\frac{1}{k_j \omega_j} N_j |a_{jy}|^2 - \frac{3 k_j}{\sigma_j} C_j \{ M_j + 3 P_j \} a_j^* A_j$$
$$+ 3 \{ h^2 \frac{k_j}{\sigma_j} M_j - \frac{2}{\omega_j k_j} C_j P_j \} a_j^* a_{jyy}] + c.c.$$

$$+ \quad \beta \frac{k_1}{\omega_1^2} C_1^2 C_2 L e^{\imath \delta x} a_1^2 a_2^* + c.c. \tag{A.14}$$

where M, N, P, L are complicated coefficients that depend on the frequency and wavenumber of the waves, the boundary layer thickness, and the parameter β. Finally, we add the above contribution to the mass transport equation, which now looks like

$$\frac{\partial h(x, y, T)}{\partial T} = \frac{K}{\rho_0} [\mu_{1x} + \alpha(\mu_{2x} + \nu_{1y})]. \tag{A.15}$$

An illustration of the contribution of the second order theory is shown below. Figure A.1 shows the cross section of the higher order contributions to the surface wave field, and Figure A.2 gives a comparison of the eventual bottom topography which is formed by the action of the higher order drift velocity to the case in which no higher order contributions are used. The bottom initially had a profile $f(x) = 0.006$, the frequency was $\omega_1 = 1.8$. The parameters were set at $\alpha = 0.1$, $\beta = 0.08$, $\varepsilon = 0.2$.

Figure A.1 and Figure A.2 display the higher order effects for the same problem and parameters used to generate Figure 6.1 and Figure 6.2. Although the plots for the higher order contributions have been produced with an exagerated vertical scale, it is not clear whether in reality , these quantities do indeed eventually diverge.
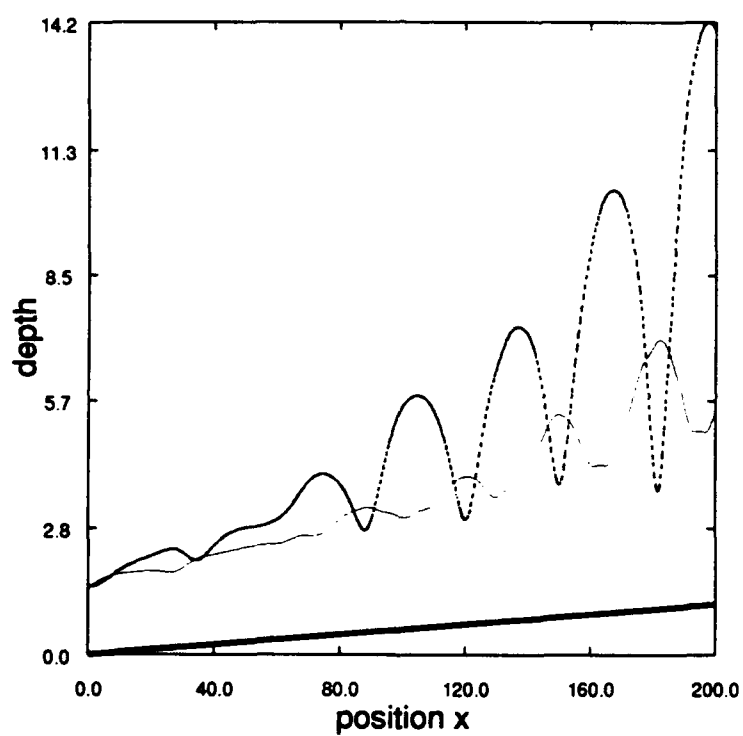
Figure A.1: Higher order contributions to the surface wave field at $T = 0$. The vertical scale has been exagerated.The lower curve represents the bottom. A_1: ————————.A_2:- - - - - - - -.
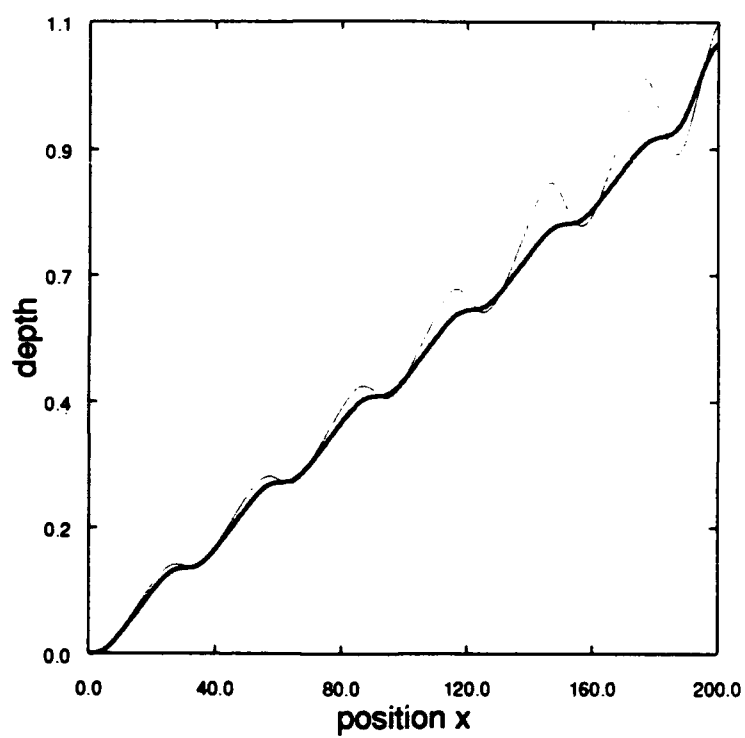
Figure A.2: Higher contributions to the bottom topography. The bottom was initially $f(x) = 0.006$. Eventual bottom with —————, and with no ········ higher order contributions.

Appendix B

Slightly Interacting Resonant Quartets

This appendix contains the expressions for the lowest order surface wave modal amplitudes for the case of quartet interactions.

The presentation is limited to the incident wave field. The relation among the frequency and wavenumbers, that $\omega_j = j\omega_1$, $k_2 = 2k_1 - \delta$, and $k_3 = 3k_1 - \Delta$ is given by the dispersion relation. The procedure is the same as the two mode case. Substituting Equations(2.65) and (2.67), with $j = 1,2,3$, into the compatibility condition, Equation (2.71) yields the following system:

$$a_{1x} + i\varepsilon f D_1 E_1 a_1 - i\alpha F_1 a_{1yy} + i\alpha D_1 S_{211}\epsilon^{-i\delta x}a_1^* a_2 + i\alpha D_1 S_{321}e^{i\Delta x}a_2^* a_3 = 0$$

$$a_{2x} + i\varepsilon f D_2 E_2 a_2 - i\alpha F_2 a_{2yy} + i\alpha D_2 S_2\epsilon^{+i\delta x}a_1^2 + i\alpha D_2 S_{312}e^{i\Delta x}a_1^* a_3 = 0$$

$$a_{3x} + i\varepsilon f D_3 E_3 a_3 - i\alpha F_3 a_{3yy} + i\alpha D_3 S_3 e^{-i\Delta x}a_1 a_2 = 0,$$

$$(B.1)$$

to $O(\delta/X)$. The constants are

$$
\begin{aligned}
D_j &= 1/2(1 - \frac{\beta^2 \omega_j^2}{3}) \\
E_j &= k_j(1 - \frac{2\beta^2 \omega_j^2}{3}) \\
F_j &= 1/2k_j \\
S_3 &= \frac{k_2+k_1}{\omega_3}\{k_2 + k_1 + 3\omega_1(\frac{\omega_1}{k_1} + \frac{\omega_2}{k_2})\} \\
S_2 &= \frac{2}{\omega_2}k_1^2 + 2\omega_1^2 \\
S_{ijl} &= \frac{k_i-k_j}{l\omega_1}\{k_i - k_j + l\omega_1(\frac{\omega_i}{k_i} + \frac{\omega_j}{k_j})\}
\end{aligned}
\tag{B.2}
$$

The boundary conditions are similar to Equation (4.2), except that there are three modes rather than two that need to be pinned down at the boundary. Thus

$$
a_j(0, y) = \mathcal{A}_j,
\tag{B.3}
$$

with $j = 1, 2, 3$, plus appropriate boundary conditions on the lateral sides of the domain.

References

[1] Boczar-Karakiewicz, B., Bona, J. L. & Cohen, G., *Interaction of Shallow-water waves and bottom topography*, PSU Applied Mathematics Series #AM3, Penn State University, 1986.

[2] Boczar-Karakiewicz, B., Bona, J. L. & Pelchat, A., "Interaction of Shallow Water Internal Waves with the Bottom Topography," *Continental Shelf Research* 11 (1991), 234-345.

[3] Sleath, J. F. A., *Sea Bed Mechanics*, John Wiley and Sons, New York, 1984.

[4] Davis, R. A., Fox, W. T., Hayes, M. C. & Boothroyd, J. C., "Comparison of Ridge and Runnel Systems in Tidal and Non-Tidal Environments," in *Proceedings, 8th. Conference of Great Lakes Research*, Int. Ass. Great Lakes Research, 1965, 223-231.

[5] Off, T., "Rhythmic Sand Bodies Caused by Tidal Currents," *Bulletin of the American Association of Petroleum Geologists* 47 (1960), 324-341.

[6] Allen, J. R. L., in *Current Ripples*, North Holland, 1968, 434.

[7] Swift, D. J. P., "Quaternary Shelves and the Return to Grade," *Marine Geology* 1 (1968), 5-30.

[8] Lau, J. & Travis, B., "Slowly Varying Stokes Waves and Submarine Longshore Bars," *Journal of Geophysics Research* 78 (1973), 4489-4497.

[9] Boczar-Karakiewicz, B., Amos, C. L. & Drapeau, G., "The Origin and Stability of Sand Ridges on Sable Island Bank, Scotian Shelf," *Continental Shelf Research* 10 (1990), 683-701.

[10] Short, A., "Multiple Off-shore Bars and Standing Waves," *Journal of Geophysical Research* 80 (1975), 3838-3840.

[11] Dean, C., "'Nearshore' is Plumbed for Clues to Explain How Beach Waves Act." The New York Times, June 12, 1990.

[12] Boczar-Karakiewicz, B., Benjamin, T. B. & Pritchard, W. P., "Reflection of Water Waves in a Channel with Corrugated Bed," *Journal of Fluid Mechanics V185P 229-247* (1987).

[13] Pritchard, W. G., Personal Communication.

[14] Bijker, E. W., Hijun, E. & Vallinga, P., "Sand Transport by Waves." *Proceedings, 15th International Conference on Coastal Engineering* (1976).

[15] Hallermeier, R., "Oscillatory Bed-Load Transport." *Continental Shelf Research* 1 (1982), 159-190.

[16] Elgar, S., Guza, R. T. & Freilich, M., "Eulerian Measurements of Horizontal Accelerations in Shoaling Gravity Waves," *Journal of Geophysical Research* 93 (1988), 9261-9269.

[17] Bagnold, R. A., "Motion of Waves in Shallow Water. Interaction of Waves and Sand Bottoms." *Proc. Roy. Soc. London Ser. A* 187 (1963), 1-15.

[18] Bailard, J. A. & Inman, D. L., "An Energetics Model for a Plane Sloping Beach. Local Transport." *Journal of Geophysical Research* 75 (1970), 5800-5812.

[19] Smith, J. D., "The Stability of a Sand Bed Subjected to Shear Flow at Low Froude Number ," *J. Geophys. Res.* 75 (1970), 5928-5940.

[20] Fredœ, J., "On the Development of Dunes in Erodible Channels," *Journal of Fluid Mechanics* 64 (1974), 1-16.

[21] Richards, K. J., "Formation of Ripples and Dunes on an Erodible Bed." *Journal of Fluid Mechanics* 99, 597-618.

[22] Dean, R., "Future Directions in Cross-shore Transport Modelling," Coastal Sediment Workshop '91. 1991.

[23] Raudkivi, A. J., "Study of Sediment Ripple Formation," *Proc. American Society of Civil Engineering, Hydraulics Division* 89 (1963), 15–36.

[24] Williams, P. B. & Kemp. P. H., *Proceedings American Society of Civil Engineering* 97 (1971), 505.

[25] Longuett-Higgins, M. S., "Mass Transport in Water Waves," *Phylosophical Transactions of the Royal Society of London* 245 (1953), 535–581.

[26] Stokes, G. G., *Phylosophical Transactions of the Royal Society of London* 8 (1847), 441.

[27] Johns, B., "On the Mass Transport Induced by an Oscillatory Flow in a Turbulent Boundary Layer," *Journal of Fluid Mechanics* (70), 177–185.

[28] Blondeaux, P., "Sand Ripples under Sea Waves. Part 1. Ripple Formation," *Journal of Fluid Mechanics* 218 (1990), 1–17.

[29] Vittori, G. & Blondeaux, P., "Sand Ripples under Sea Waves. Part 2. Finite-amplitude Development," *Journal of Fluid Mechanics* 218 (1990), 19–39.

[30] Holman, A. & Bowen. A. J., "Bars, Bumps and Holes: Model for the generation of Complex Beach Topography," *Journal of Geophysical Research* 87 (1982), 457–468.

[31] Bowen, A. J., "On-Offshore sand transport on a beach, (Abstract)," *EOS, Transportation Sci. of the American Geophysical Union* 56 (1975), 83.

[32] Mei, C. C. & Ümlüata, "Harmonic Generation in Shallow Water Waves," in *Waves on Beaches*. R. E. Meyer. ed., Academic Press. San Diego, 1972.

[33] Hara, T. & Mei, C. C., "Bragg Scattering of Surface Waves by Periodic Bars. Theory and Experiment," *Journal of Fluid Mechanics* 152 (1987), 221–241.

[34] Mei, C. C., Hara, T. & Naciri, M., "Note on Bragg Scattering of Water Waves by Parallel Bars on the Sea Bed.," *Journal of Fluid Mechanics* 187 (1990), 147–162.

[35] deVriend, H. J., "2DH Computation of Transient Sea Bed Evolution," in *20th International Conference on Coastal Engineering*, Taipei, 1986.

[36] Russell, R. C. H. & Osorio, J. D. C., "An Experimental Investigation of Drift Profiles in a Closed Channel," *Proc. 6th. Conference on Coastal Engineering* (1975).

[37] Bijker, E. W., Kalkwijk, J. P. T. & Pieters, T., "Mass Transport in Gravity Waves on a Sloping Bottom," *Proceedings, 14th Conference on Coastal Engineering* (1974).

[38] J. M. Huthnance, "Internal tides and waves near the continental shelf," *Geophys. Astrophys. Fluid Dynamics* 48 (1989), 81–106.

[39] Suhaida, J. M., "Standing Waves on Beaches," *Journal of Geophysical Research* 79 (1974), 3065–3071.

[40] Lau, J. & Barcilon, A., "Harmonic Generation of Shallow Water Waves over Topography," *Journal of Physical Oceanography* (1972).

[41] Elgar, S., Freilich, M. & Guza, R. T., "Recurrence in Truncated Boussinesq Models of Nonlinear Waves in Shallow Water," *Journal of Geophysical Research* 95 (1991), 11547–11556.

[42] Caponi, E. A., Saffman, P. G. & Yuen, H. C., "Instability and Confined Chaos in a Nonlinear Dispersive Wave System," *Physics of Fluids* 25 (1982), 2159–2166.

[43] Herbst, B. M., Weideman, J. A. C. & Ablowitz, M. J., "Dynamics of Semi-discretizations of the Focusing Nonlinear Schrödinger Equation," Preprint, 1990.

[44] J. Boussinesq, "Theorie des ondes et des remous qui se ...," *J. Math. Pures Appl.* 2 (1872), 55–108.

[45] Batchelor, G. K., *Introduction to Fluid Dynamics*, Cambridge University Press, 1988.

[46] Phillips, O. M., "On the Generation of Waves by Turbulent Wind," *Journal of Fluid Mechanics* 2 (1957), 417–445.

[47] Miles, J., "Shearing Flow over a Wavy Wall," *Journal of Fluid Mechanics* 3 (1957), 185–204.

[48] Zakharov, V. E. & Shabhat, A. B., "Exact Theory of Two-dimensional Self-focusing and One-dimensional Self-modulation of Waves in Nonlinear Media," *Soviet Physics. JETP* 34, 62–69.

[49] Miles, J., "On Hamilton's Principle for Surface Waves," *Journal of Fluid Dynamics* 83 (1977), 153–158.

[50] S. Bowman, "Hamiltonian formulations and long-wave models for two-fluid systems," unpublished, 1986.

[51] T. B. Benjamin, "Lectures on Nonlinear Wave Motion," in *Nonlinear Wave Motions*, Alan Newell, ed., Lectures in Applied Mathematics #15, 1974, 3–47.

[52] T. B. Benjamin & P. J. Olver, "Hamiltonian structure, symmetries and conservation laws for water waves," *J. Fluid Mech.* 125 (1982), 137–185.

[53] Lord Rayleigh, "On Waves," *Philosophical Magazine* 5 (1876), 257–279.

[54] Peregrine, D. H., "Long Waves on a Beach," *Journal of Fluid Mechanics* 27 (1967), 815–827.

[55] Benjamin, T. B., Bona, J. L. & Mahony, J. J., "Model Equations for Long Waves in Nonlinear Dispersive Systems," *Philosophical Transactions of the Royal Society* A 227, 47–78.

[56] Druet, Cz., Massel, S. R. & Zeidel, R., "The Structure of Wind Waves in the Southern Baltic Sea," *Ruzprawy Hydrotechniczne* 30 (1972), 312–318.

[57] Apel, J. R.. "Observations of Internal Wave Signatures in ASTP Photographs," in *Apollo-Soyuz Test Project. Summary Science Report* #SP-H12. NASA, 1979, 505–509.

[58] Baines, P. G., "Satellite Observations of Internal Waves on the Australian North-West Shelf," *Australian Journal of Marine and Freshwater Research* 32, 457–463.

[59] Chapalain, E., "Etude hydrodynamique et sédimentaire des Environments littoraux dominés par la Houle," in *Ph.D. Thesis*, Institut de Méchanique de Grenoble. Université de Grenoble, 1988, 319.

[60] Boczar-Karakiewicz, B., Forbes, D. L. & Drapeau, G., "Formation and Stability of Nearshore bars in the Southern Gulf of St. Lawrence," *Geological Survey of Canada, Contribution 33187* (1990).

[61] Svendsen, I. A., "A Model for Sedimentary Motion under Waves," *Internal Research Note* (1977).

[62] Lax, P. D., *Hyperbolic Systems of Conservation Laws and the Mathematical Theory of Shock Waves*, Regional Conference Series on Applied Mathematics #11, Society for Industrial and Applied Mathematics, Philadelphia, PA, 1973.

[63] Armstrong, J. A., Ducuing, J. & Persham, P. S.. "Interaction between Light Waves in a Nonlinear Dielectric," *Physical Review* 127 (1962), 1918–1939.

[64] Hasselmann, K., "On the Nonlinear Energy Transfer in a Gravity-Wave Spectrum," *Journal of Fluid Mechanics* 12 (1962), 481–500.

[65] Brekhovskikh, L. M. & Goncharov, V., *Mechanics of Continua and Wave Dynamics*. Springer Series on Wave Phenomena #1. Springer-Verlag, New York, 1985.

[66] Smith, J. D., *Numerical Solution of Partial Differential Equations, Finite Difference Methods* #3rd. Edition, Clarendon Press, Oxford, 1985.

[67] Press, W. H., Flannery, B. P., Teukolsky, S. A. & Vetterling, W. T., *The Art of Scientific Computing, Numerical Recipes*, Cambridge University Press, Cambridge, 1989.

[68] Golub, G. H. & Van Loan, C. F., *Matrix Computations*, The Johns Hopkins University Press, Baltimore, 1989.

[69] Bona, J. L., Personal Communication.